AEROSPACE RESEARCH IN BULGARIA

Volume 23, Sofia, 2009
Space Research Institute
Bulgarian Academy of Sciences

Address
AEROSPACE RESEARCH IN BULGARIA
Space Research Institute
6, Moskovska St., Sofia 1000, Bulgaria

e-mail: office@space.bas.bg

ISSN 1313 – 0927

Bulgarian Academy of Sciences **ISSN 1313 – 0927**

Aerospace Research in Bulgaria

23
Sofia, 2009

C o n t e n t s

С Ъ Д Ъ Р Ж А Н И Е

Bulgarian Academy of Sciences. Space Research Institute.
Aerospace Research in Bulgaria. 23, 2009, Sofia

BRIEF OVERVIEW OF SOME RECENT DEVELOPMENTS IN THE THEORY OF NON–AXISYMMETRIC ACCRETION DISCS

Dimitar Dimitrov

Space Research Institute - Bulgarian Academy of Sciences
e-mail: dim@mail.space.bas.bg

Abstract

This overview considers the recent status of accretion disc theory in the cases of non-axisymmetric flows around compact objects with stellar masses. Examples of the absence of circular symmetry may be not only the discs' elliptical shape, but also the spiral density waves, the non-circular gaps in the discs and the density clumps (protoplanets). The overview is based on papers in the field published during the last four years. The implications concerning the observational appearances are also discussed. The considered problem of non-axisymmetry is examined both from theoretical and observational point of view. The former approach also includes numerical simulations of accretion flows. This review touches upon problems related with such astrophysical objects which need to be resolved.

Introduction

The present investigation of non-circular accretion discs is bounded preferably to the cases of stationary Keplerian discs, orbiting around stellar mass compact objects in close binary systems. The normal components in these systems supply the matter which is needed for discs to exist in a (quasi)stationary state. They also tidally affect accretion flows, causing in such a way their elliptical shape. It would be stressed that the elliptical orbits of the disc particles may arise not only due to the external factors, but also as a consequence of internal instabilities inherent to the accretion discs alone. To some extent, the structure of the outermost parts of accretion discs may be affected by the infalling flows of matter coming from the star

orbiting around the compact object (the so called “bright spot”). Observational data, when there is a possibility for high spatial/angular and spectral resolutions of circumstellar discs, are consistent (as a rule) with the existence of Keplerian rotating gaseous discs. For example, the massive star R Mon has a clearly established Keplerian disc [1]. But there are also some exceptions, as we shall see later [3]. Such high-quality observations of the stellar accretion discs, however, are not numerous. In the lack of great amount of direct (spatially resolved) observations of discs, theoretical physics has tried to provide reasonable analytical and numerical models with varying degrees of success. This is due to the uncertainties which still exist in accretion disc theory (even with respect to some basic equations). In this situation, progress may be made, if the investigations are restricted to particular object cases hoping that the results are likely to have in some sense direct impact on the understanding of other objects.

With respect to numerical experiments, it may be definitely said that the use of modern powerful computers allows performing of 3D smoothed particle hydrodynamics calculations with high spatial and temporal resolution and more realistic viscosity and sound-speed prescriptions. Such approach may be successfully applied to the modelling of eccentric instability, which underlies the superhump phenomena in nova-like binaries such as SU Ursae Majoris variables [2]. Comparison of 2D and 3D results leads to the conclusion that 3D simulations are an indispensable requirement to obtain reasonable description of the disc’s dynamics. Numerical simulations reveal that it is necessary to run computations of very long durations to achieve eccentric equilibrium, and that saturation depends on the mass ratio of the stars in the binary system.

Another problem arises when the description of the disc’s dynamics is limited only to the Newtonian case. As a rule, the inner part of the accretion disc is affected by the very strong gravitation of the compact object. Consequently, the general relativistic effects must be taken into account. In some particular cases, when the modelling is limited to a stellar mass black hole accreting at a low rate, the disc close to the central object cannot survive and is evaporated. This is in agreement with earlier theoretical and observational results for low accretion rates [3]. In the other cases of high accretion rates onto the compact object, the advection processes most probably determine the inner disc structure, and therefore, a Keplerian motion of the accreted material is not a good approximation.

There is also an important factor, which in many situations cannot be neglected when the disc dynamics is a subject of computations. In stellar accretion discs, especially in their high temperature inner regions, the gas is highly ionized plasma. Consequently, there are strong magnetic fields with complex spatial and temporal structure of their magnetic lines. Simulations and analytical arguments indicate that the turbulence driven by magnetorotational instability in accretion discs can amplify the azimuthal component of the magnetic field to a point at which the magnetic pressure exceeds the combined "gas + radiation" pressure in the disc. Examination of the properties of these magnetically dominated discs shows that, in such manner, a number of outstanding problems in accretion disc theory are resolved [4]. These investigations show that the discs would be thicker than the standard Shakura-Sunyaev discs [22] at the same radius r and accretion rate. They would also tend to have higher colour temperature. If such accretion flows, transport angular momentum according to an α-prescription, they would be stable against the thermal and viscous instabilities that were found in the standard disc models. Other studies concerning the viscous evolution of protoplanetary discs include the combined action of magnetohydrodynamic turbulence (generated by magnetorotational instability), self-gravity torques (parametrized in terms of an effective viscosity) and also an additional viscous agent (of unspecified origin) [5]. It was generally found that accretion discs rapidly evolve towards a configuration where the intermediate regions of the radii r between a fraction of an astronomical unit and a few astronomical units are stable against magnetorotational instability due to their low ionization degree. When an additional source of viscosity was assumed to operate in these regions, it was obtained that the subsequent evolution of the disc was eruptive, i.e., highly nonstationary. Namely, brief episodes of high mass accretion rate ensure satisfaction (though for a short time) of the criterion for development of magnetorotational instability in the regions of low ionization. These theoretical investigations reveal that the radial distribution of mass and temperature in the accretion disc may be considerably different from the disc models with constant α-parameter or layered accretion models. Although magnetic fields are widely believed to play a crucial role in the transport of angular momentum, in the models of ionized atmospheres of accretion discs their contribution to the vertical hydrodynamic support has been generally neglected. Simulations of magnetorotational turbulence in a vertically stratified geometry show that the magnetic pressure support can

be dominant in the upper layers of the discs. It generically produces a vertically more extended disc atmosphere with a larger density scale height. This feature acts to harden the emitted spectrum of accretion flows compared to the models where the vertical magnetic pressure support has been neglected [6].

Obviously, the great variety of accretion disc geometries, initial conditions, different simplifications introduced into the models, etc., do not permit analytical treatment of all these combinations, and in some cases, even the self-consistency of the parameters of the concrete models may not be ensured. In such complicated situations it is useful to apply numerical methods to solve the problems. Of course, this approach does not mean that the universal prescription has been found. The two commonly used techniques of grid and smoothed particle hydrodynamics show striking differences in their ability to model processes that are important across many areas of astrophysics. For example, Eulerian grid-based methods are able to resolve and treat Kelvin-Helmholtz and Rayleigh-Taylor dynamical instabilities, but these processes are poorly or even not at all resolved by the existing techniques based on the smoothed particle hydrodynamics methods [7]. The reason for this is that in the latter case the standard implementation of the smoothed particle hydrodynamics introduces spurious pressure forces on particles in regions where there are steep density gradients. Another serious problem encounters in numerical simulations is taking into account the vertical structure of the accretion flow, i.e. its 3D nature. Even at a resolution of one million particles, the vertical structure in the disc simulations may not be accurately reproduced inside 10 astronomical units, where the midplane densities drop well below their analytical values. The erroneously low densities may lead to enhanced fragmentation in those regions, even if the structure is accurately modelled further out [8]. It should be mentioned that the resolved and unresolved parts of the disc are not isolated from each other. When waves or other perturbing structures propagate through the disc their subsequent evolution will be apparently influenced by the change in resolution. Hence, the evolution of the perturbations throughout the entire simulation becomes suspect.

In numerical simulations of accretion flows it is important to quantify what changes in the behaviour of the models occur as a function of gravitational softening; for example, in order to be able to sort out real and artificial effects. That is, it must be possible to decide which effects are to be considered to be numerically induced rather than due to physical processes.

Often, such a situation arises when the reality of fragmentation events must be checked. The authors of paper [9] conclude that the ability of the accretion disc to remain in a self-regulated and self-gravitating state (without fragmentation) is partly dependent on the thermal history of the disc, as well as on its current state of cooling. An important implication of their work is that self-gravitating discs can enter into the fragmentation regime via secular evolution and it is not necessary to invoke rapid/impulse events to trigger fragmentation. Another investigation [8] shows that fragmentation will be enhanced in under-resolved simulations or (more importantly) in real physical systems. Simulations which are performed with different systems of initial conditions, different resolutions in time and space, different approximations etc., may lead to similar results about the fragmentation, which occurs in each numerical accomplishment. In other words, the simulations may be in fact converged to the same results. This conclusion may be actually true, but nevertheless there is no guarantee that it may be also seriously misleading. Due to uncertainties in their design, numerical simulations are also able to tend to converge to incorrect results. The interpretation of these results, in terms of the physical behaviour of accretion flows and the importance of the other correctly implemented physical processes, becomes difficult or even impossible [8]. Sometimes, the results and their invalidity can be clearly and/or easily established, but the same statement may not be true in other simulations, where the results could be more difficult to verify. Another investigation [10] examined whether accretion discs around the massive stars are likely to fragment due to self-gravity. It was established that the rapid accretion and the high angular momentum push these discs towards fragmentation. Oppositely, viscous heating and high protostellar luminosity tend to stabilize them. Generally speaking, for a broad range of protostellar masses and for reasonable accretion times, the massive discs larger than 150 astronomical units are prone to fragmentation. The discs are marginally prone to fragmentation around stars of about 4÷15 solar masses, even for conservative estimates of the disc's radii and tendency to fragment. The discs around more massive stars are progressively more likely to fragment and there is a sharp drop in the stability of disc accretion at very high accretion rates, which are expected for accretion flows around very high stellar masses: 110 solar masses and more. The conclusion made in paper [10] is that fragmentation may starve accretion in massive stars, especially

above the latter's mass limit and is likely to create swarms of small coplanar dense condensations.

As follows from the extensive researches devoted to the evolution of the fragments in accretion discs, the appearance of planet systems is a common phenomenon. The latter circumstance may affect appreciably the structure of accretion discs. The most striking appearance of such kind is the formation of gaps in the discs cleared by the planets. One such observational evidence of the existence of gaps is the spectral energy distribution of some T Tauri stars which display a deficit of near-infrared flux. A possible explanation of this event is that it could be a consequence of an embedded Jupiter-mass planet, partially clearing an inner hole in the circumstellar disc [11]. In this paper, it was shown that the pressure gradient at the outer edge of the gap (cleared by the planet) acts as a filter. Namely, particles, smaller than a critical size, pass through the gap to the inner disc, and the larger ones are held back in the outer disc. This process leads to discontinuous grain population across the planet's orbital radius, with small grains in the inner disc and larger grains in the outer disc. This type of dust population was found qualitatively consistent with the spectral energy distribution in the models of stars that have optically thin inner holes in their circumstellar discs. Edgar et al. [12] consider the minimum mass of the planet as a function of its orbital radius that is capable to open a gap in an α-accretion disc. They estimate that a planet with a ½ Jupiter mass can open a gap in a disc with accretion rate corresponding to viscosity parameter $\alpha = 0.01$ and central star with solar mass and solar luminosity. It was established that, if a gap-opening planet cuts off disc accretion, allowing formation of a central hole or clearing a ring in the disc, then the clearing radius would be approximately proportional to the stellar mass.

Theoretical and observational evidence of globally non-axisymmetric accretion discs

Let us denote by M_1 the mass of the compact stellar object around which the accretion flow rotates, and by M_2 – the mass of the companion star. Respectively, $q = M_2/M_1$ is the mass ratio of the components of the binary stellar system. By means of numerical simulations, analysis of the dynamics and geometry of accretion discs in binary systems with $q < 0.1$ was performed. This investigation refers to ultracompact X-ray binaries, AM CVn stars and cataclysmic variables with very short periods. It was found that the steady state geometry of the disc in the binary reference

frame may be quite different from the geometry expected for higher mass ratio q >0.1. For q = 0.1, the disc takes on the usual elliptical shape, with the major axis aligned perpendicular to the line of centres of the two stars. However, at smaller mass ratios (q < 0.1), the elliptical gaseous orbits in the outer regions of the disc are rotated in the binary plane. For much smaller values of q (q = 0.01; i.e. an order of magnitude smaller), the major axes of these orbits are aligned almost parallel to the line of centres of the two stars [13]. The steady-state geometry at low mass ratio q has not been found to be predicted by an inviscid, restricted three-body model of gaseous orbits. Instead, it is related to the effects of tidal-viscous truncation of the accretion disc near the Roche lobe boundary. Numerical investigations of Amand Smith et al. [2] also confirm the conclusion that the global structure of accretion discs may essentially depend on the mass ratio q. The latter authors have found that for q > 0.24, the high-resolution 3D models of the discs do not show development of superhumps/superoutbursts. It turns out that this property agrees with the analytical expectations.

The non-axisymmetric structure of accretion discs in Be/X-ray binaries was studied in [14] by performing three-dimensional smoothed particle hydrodynamics simulations for a system with a short orbital period and a moderate orbital eccentricity. It was found that the pressure due to the phase-dependent mass transfer from the disc of the Be star excites a one-armed, trailing spiral structure in the accretion disc around the neutron star. The numerical simulations established that the spiral wave was a transient event. It was excited around the periastron passage, when the material was transferred from the Be-disc and it was gradually damped afterwards. These investigations demonstrated that the accretion disc changes its morphology from circular to eccentric with the development of the spiral wave, and then from eccentric to circular with the decay of the wave during the orbital period. Another numerical study also gives similar conclusions about the evolution of the accretion disc's structure. Vorobyov and Theis [15] have studied the time-dependent evolution of stellar discs in the linear regime and partially in the non-linear one. They have established that in the earlier linear phase, the very centre and the large scales are characterized by growing one-armed and bisymmetric positive density perturbations, respectively. But in the late linear phase, the overall appearance is dominated by a two-armed spiral structure localized within the outer Lindblad resonance. During the non-linear evolutionary phase, radial mass redistribution due to the gravitational torques of spiral arms produces an

outflow of mass, which forms a ring at the outer Lindblad resonance, and also an inflow of mass, which forms a transient central bar. As a final result, a compact central disc and a diffuse ring at the outer Lindblad resonance are formed. In [2] it was concluded that the disc models reveal a complex standing wave dynamics, which repeats (in the inertial frame) the disc precession period. This picture of the disc motions can be described as a superposition of different spiral modes. The authors of paper [2] characterize the eccentricity distribution in their accretion disc models and show that the entire body of the disc has its contribution which must be taken into account when evaluations of disc eccentricity have to be made.

The instabilities of non-axisymmetric gaseous discs are also subject of investigation in [16], where a perturbation theory for studying of these phenomena is presented. For such discs, the amplitude and the phase angle of the travelling waves are functions of both the radius r and the azimuthal angle φ, because of the interaction of different wave components in the response spectrum. It was demonstrated that wave interaction in unstable discs (with small initial asymmetries) can develop dense clumps during the phase of exponential growth of instabilities. Such events are relevant to the formation of planet systems around the accreting stars. Namely, local clumps, which occur on the major spiral arms, may play the role of seeds of gas giant planets in accretion discs.

Special cases of accretion flows are the circumbinary accretion discs orbiting around binary stars (i.e., the latter being in the centres of the discs). There are studies of two-dimensional thin, viscous, locally isothermal corotating discs, which investigate the structure of the discs after multiple viscous times. One of them is presented in paper [17], where a numerical modelling of a flow, moving in the orbital plane of two equal mass point masses (rotating along a fixed circular orbit) is performed. The binary system maintains a central hole in the viscosity relaxed disc with hole radius equal to about twice the binary semimajor axis. The model shows that the disc surface density Σ within the hole is reduced by orders of magnitude relative to the density in the disc bulk. The initially circular disc becomes elliptical and after that, eccentric. Disturbances in the disc contain a component that is stationary in the rotating frame in which the binary star is at rest and this component is a two-armed spiral density wave.

Returning to the effects of planets on accretion discs, the paper of Hosseinbor et al. [18] should be mentioned, where such an investigation is performed for a planet moving along an eccentric orbit. The planet acts on a

two-dimensional low-mass gaseous disc. The authors find that the disc morphology differs from that exhibited by a disc containing a planet in a circular orbit. An eccentric gap is created with eccentricity that can exceed the planet eccentricity and precesses with respect to the planet orbit. It is established that a more massive planet is required to open a gap, when the planet is on an eccentric orbit. In [18], this behaviour is attributed to spiral density waves excited at corotation resonances by the eccentric planet orbit. These act to increase the disc's eccentricity and exert a torque opposite in sign to the one exerted by the Lindblad resonances. Another group of collaborators also investigates the interaction between a giant planet and a viscous circumstellar disc by means of high-resolution, 2D hydrodynamic simulations [19]. They also find that a planet can cause eccentricity growth in a disc region adjacent to the planet orbit, even if the latter is circular. Moreover, disc-planet interactions lead to increase of planet orbital eccentricity. The accretion rate towards a planet depends on both the disc and the planetary orbital eccentricity and is pulsed over the orbital period of the planet. Similar accretion modulation occurs in the flow at the inner disc boundary, which represents the accretion towards the star [19]. A concrete example of the planet-disc interactions is discussed in paper [20], where it is suggested that a planet just interior to the ring edge causes the eccentricity and sharpness of the edge of Fomalhaut's disc. The collision time-scale is evaluated as being long enough that spiral density waves could not be able to be driven near the planet. It is also found that the ring edge has eccentricity, caused by secular perturbations from the planet and its eccentricity, equal to 0.1 (the same as of the planet orbit).

The role of magnetic fields on accretion disc structure

Here we shall consider in some details the influence of large scale organized magnetic fields. Such fields may play a major role in understanding the dynamical and spectral properties of X-ray binary stars. Although most of the models are computed for discs with circular orbits of their gaseous flows, the results have also implications on elliptical accretion discs. It is important to note that numerical simulations of turbulent, magnetized, differentially rotating flows, driven by the magnetorotational instability, are often used to calculate the effective values of α-viscosity that is invoked in the analytical models. The authors of paper [21] show that the angular momentum transport in magnetorotational instability-driven accretion discs cannot be described by the standard model of Shakura and

Sunyaev [22] for shear viscosity. The former demonstrate that turbulent magnetorotational stresses are not linearly proportional to the local shear and vanish identically for angular velocity profiles that increase outwards [21]. The properties of a geometrically thin, steady magnetically torqued accretion disc model is computed in [23] for a flow around a central rotating magnetized star. The magnetosphere in these calculations is assumed to entrain the disc over a wide range of radii. The solution for angular velocity profile tends to corotation close to the central star and smoothly matches a Keplerian curve at a radius where the viscous stress vanishes. It was also found that for rapid rotators the accretion disc might be powered mostly by the spin-down of the central star. These results are independent on the viscosity prescription in the disc. Another investigation [24] deals with the role of disc magnetization on the hysteresis behaviour of X-ray binaries. The precisely worked out model contains a transition radius below which a jet-emitting disc is settled. The latter drives self-collimated non-relativistic jets. But beyond the transition radius, no jets are produced and a standard accretion disc is established, despite the presence of magnetic fields. The radial distribution of disc magnetization adjusts itself to any change in the disc accretion rate, thus modifying the established transition radius. This property opens the possibility for the transitions between standard accretion disc and jet-emitting disc and their reverse transitions to occur locally at different magnetization. This bimodal behaviour of the accretion disc may explain the hysteresis cycles observed in X-ray binary stars during outbursts. It is well known that such events are closely related to the elliptical shape of the accretion disc.

Concluding remarks

The evolution of astrophysical discs is dominated by instabilities of gravity perturbations, including those produced by spontaneous disturbances. A hydrodynamic theory of non-resonant Jeans instability in the gaseous component of a disc has been developed [25], in which it is shown analytically that gravitationally unstable systems (such as, in particular, protoplanetary discs) are efficient at transporting mass and angular momentum. Already on a timescale of the order of 2 or 3 rotational periods, the unstable accretion flow has a large portion of its angular momentum transferred outward and mass transferred both inward and outward.

As already mentioned, the true estimations of the values of the viscosity parameter α are of essential importance when the dynamics of accretion flows must be determined. This is valid both for discs with circular and elliptical orbits of their particles. For accretion discs, the height scale is a constant whenever hydrostatic equilibrium and the subsonic turbulence regime hold. In order to have a variable height scale, an extra term must be added to the continuity equation, due to processes of specific physical nature. Such a contribution makes the viscosity parameter α much greater in the outer region and much smaller in the inner region of the disc [26]. Under these circumstances, the hydrodynamical turbulence is the presumable source of viscosity in the disc. There is no need to include magnetic fields in the considerations. The way disc structure is affected by the values of α is demonstrated by Liu et al. [27], where the condensation of matter from a corona to a cool, optically thick inner disc is investigated. They give a description of a simple model for the exchange of energy and mass between corona and disc taking into account the effect of Compton cooling of the corona by photons from underlying disc. It is established that the inner disc can be present in the low/hard state for a range of luminosities that depends on the magnitude of the viscosity parameter. For $\alpha \approx 0.1 \div 0.4$, such an inner disc can exist for solar luminosities within the range $0.001 \div 0.02$. This example illustrates how essential the precise evaluation of the viscosity parameter α may be, when the global structure of accretion flows must be derived.

Astronomical observations of binary stars with accretion discs (both photometric and spectroscopic) enable us to check the validity of the theoretical models based on numerical or analytical approaches. Another method is the investigation of the evolution of protostellar discs around T Tauri stars that have formed self-consistently from the collapse of molecular cloud cores. Numerical studies of such objects demonstrate that the discs settle into a self-regulated state with low-amplitude non-axisymmetric perturbations persisting for at least several million years [28]. The global effect of gravitational torques due to such perturbations is to produce disc accretion rates that are of the correct magnitude to explain observed accretion onto T Tauri stars. An important development of accretion disc theory makes references to the formation of planet systems. Closely related to this problem is the process of disc fragmentation. In paper [29], the effects of eccentricity on the fragmentation of gravitationally unstable accretion discs are considered using numerical hydrodynamics. It is found

that the eccentricity does not affect the overall stability of the disc against fragmentation, but significantly alters the manner in which such fragments accrete gas. Variable tidal forces around an eccentric orbit slow down the accretion process and suppress the formation of weakly bound clumps. The "stellar" mass function resulting from the fragmentation of an eccentric disc is found to have a significantly higher characteristic mass than that from a corresponding circular disc. The application of the worked out model to massive stars at 0.1 parsecs from the Galactic center shows that the fragmentation of an eccentric accretion disc (due to gravitational instability) is a viable mechanism for the formation of these systems [29].

It is often a matter of discussion what is the range of applicability of the standard accretion disc model. As it would be expected, the limitations of its use would be the same for discs with elliptical orbits of their particles. Shaffe et al. [30] consider a simple Newtonian model of a steady accretion disc around a black hole. They use height-integrated hydrodynamic equations, α-viscosity prescription and a pseudo-Newtonian potential. The results reveal that as the disc's thickness or the value of α increases, the hydrodynamic model exhibits increasing deviations from the standard thin disc model [22]. However, these results must be taken with a caution, because they have been obtained with a viscous hydrodynamic model. More accurate quantitative estimates need to be received by magnetohydrodynamic simulations of radiatively cooled thin discs.

References

1. Fuente A., T. Alonso – Albi, R. Bachiller, A. Natta, L. Testi, R. Neri, P. Planesas. A Keplerian gaseous disk around the B0 star R Monocerotis., Astrophys. J. Letters, 649, 2006, № 2, part 2, p. L119.
2. Smith A. J., C. A. Haswell, J. R. Murray, M. R. Truss, S. B. Foulkes. Comprehensive simulations of superhumps. Monthly Not. Royal Astron. Soc., 378, 2007, № 3, p. 785.
3. Mayer M., J. E. Pringle. Time-dependent models of two-phase accretion discs around black holes., Monthly Not. Royal Astron. Soc., 376, 2007, № 1, p. 435.
4. Begelman M. C., J. E. Prigle. Accretion discs with strong toroidal magnetic fields., Monthly Not. Royal Astron. Soc., 375, 2007, № 3, p. 1070.
5. Reyes – Ruiz M. Evolution of protoplanetary discs driven by MRI, self-gravity and hydrodynamical turbulence., Monthly Not. Royal Astron. Soc., 380, 2007, № 1, p. 311.
6. Blaes O. M., S. W. Davis. Magnetic pressure support and accretion disk spectra., Astrophys. J., 645, 2006, № 2, part 1, p. 1402.

7. A g e r t z O., B. M o o r e, J. S t a d e t, e t a l. Fundamental differences between SPH and grid methods., Monthly Not. Royal Astron. Soc., 380, 2007, № 3, p. 963.
8. N e l s o n A. F. Numerical requirements for simulations of self gravitating and non-self gravitating discs., Monthly Not. Royal Astron. Soc., 373, 2006, № 3, p. 1039.
9. C l a r k e C. J., E. H a r p e r – C l a r k, G. L o d a t o. The response of self-gravitating protostellar discs to slow reduction in cooling time-scale: The fragmentation boundary revisited., Monthly Not. Royal Astron. Soc., 381, 2007, № 4, p. 1543.
10. K r a t t e r K. M., C. D. M a t z n e r. Fragmentation of massive protostellar discs., Monthly Not. Royal Astron. Soc., 373, 2006, № 4, p. 1563.
11. R i c e W. K. M., P. J. A r m i t a g e, K. W o o d, G. L o d a t o. Dust filtration at gap edges: Implications for the spectral energy distributions of discs with embedded planets., Monthly Not. Royal Astron. Soc., 373, 2006, № 4, p. 1619.
12. E d g a r R. G., A. C. Q u i l l e n, J. P a r k. The minimum gap-opening planet mass in an irradiated circumstellar accretion disc., Monthly Not. Royal Astron. Soc., 381, 2007, № 3, p. 1280.
13. T r u s s M. R. Accretion disc dynamics in extreme mass ratio compact binaries., Monthly Not. Royal Astron. Soc., 376, 2007, № 1, p. 89.
14. H a y a s a k I K., A. T. O k a z a k i. One-armed spiral structure of accretion discs induced by a phase-dependent mass transfer in Be/X- ray binaries., Monthly Not. Royal Astron. Soc. Letters, 360, 2005, № 1, p. L15.
15. V o r o b y o v E. I., Ch. T h e i s. Boltzmann moment equation approach for the numerical study of anisotropic stellar discs., Monthly Not. Royal Astron. Soc., 373, 2006, № 1, p. 197.
16. A s g h a r I N. M., M. A. J a l a l i. Unstable modes of non-axisymmetric gaseous discs., Monthly Not. Royal Astron. Soc., 373, 2006, № 1, p. 337.
17. M a c F a d y e n A. I., M. M i l o s a v l j e v i ć. An eccentric circumbinary accretion disk and the detection of binary massive black holes., Astrophys. J., 672, 2008, № 1, part 1, p. 83.
18. H o s s e i n b o r A. P., G. E. R i c h a r d, A. C. Q u i l l e n, A. L a P a g e. The formation of an eccentric gap in a gas disc by a planet in an eccentric orbit., Monthly Not. Royal Astron. Soc., 378, 2007, № 3, p. 966.
19. D'A n g e l o C., S. H. L u b o w, M. R. B a t e. Evolution of giant planets in eccentric disks., Astrophys J., 652, 2006, № 2, part 1, p. 1698.
20. Q u i l l e n A. C. Predictions for a planet just inside Fomalhaut's eccentric ring., Monthly Not. Royal Astron. Soc. Letters, 372, 2006, № 1, p. L14.
21. P e s s a h M. E., C. – K. C h a n, D. P s a l t i s. The fundamental difference between shear alpha viscosity and turbulent magnetorotational stresses., Monthly Not. Royal Astron. Soc., 383, 2008, № 2, p. 683.
22. S h a k u r a N. I., R. A. S u n y a e v. Black holes in binary systems. Observational appearance., Asron. & Astrophys., 24, 1973, № 3, p. 337.
23. K l u ź n i a k W., S. R a p p a p o r t. Magnetically torqued thin accretion disks., Astrophys. J., 671, 2007, № 2, part 1, p. 1990.
24. P e t r u c c I P. – O., J. F e r r e i r a, G. H e n r i, G. P e l l e t i e r. The role of the disc magnetization on the hysteresis behaviour of X-ray binaries., Monthly Not. Royal Astron. Soc.: Letters, 385, 2008, № 1, p. L88.

25. G r i v E., E. L i v e r t s, M. M o n d. Angular momentum transport in astrophysical disks., Astrophys. J. Letters, 672, 2008, № 2, part 2, p. L127.
26. F i l h o C. M., N. L e i s t e r. The viscosity parameter's dependence on the profile of the disk scale height., Astrophys. J. Letters, 672, 2008, № 1, part 2, p. L45.
27. L i u B. F., R. E. T a a m, E. M e y e r – H o f m e i s t e r, F. M e y e r. The existence of inner coo disks in the low/hard state of accreting black holes., Astrophys. J., 671, 2007, № 1, part1, p. 695.
28. V o r o b y o v E. I., S. B a s u. Mass accretion rates in self-regulated disks of T Tauri stars., Astrophys. J. Letters, 676, 2008, № 2, part 2, p. L139.
29. A l e x a n d e r R. D., P. J. A r m i t a g e, J. C u a d r a, M. C. B e g e l m a n. Self-gravitating fragmentation of eccentric accretion disks., Astrophys. J., 674, 2008, № 2, part 1, p. 927.
30. S h a f e e R., R. N a r a y a n, J. E. M c C l i n t o c k. Viscous torque and dissipation in the inner regions of a thin accretion disks: Implications for measuring black hole spin., Astrophys. J., 676, 2008, № 1, part 1, p. 549.

КРАТЪК ПРЕГЛЕД НА НЯКОИ ОТ СЪВРЕМЕННИТЕ РАЗРАБОТКИ В ТЕОРИЯТА НА НЕОСЕСИМЕТРИЧНИТЕ АКРЕЦИОННИ ДИСКОВЕ

Д. Димитров

Резюме

Този обзор разглежда съвременното състояние на теорията на акреционните дискове в случаите на неосесиметрични потоци около компактни обекти със звездни маси. Примери за отсъствието на кръгова симетрия могат да бъдат не само елиптичната форма на дисковете, но също спиралните вълни на плътността, имащите некръгова форма празнини в дисковете и плътните сгъстявания от вещество (протопланети). Обзорът включва статии по тази тематика от последните четири години. Дискутирани са също следствията, отнасящи се до наблюдателните прояви. Разглежданият проблем на отсъствие на осева симетрия е проучван както от теоретична, така и от наблюдателна гледна точка. Първият подход също включва числени моделирания на акреционните потоци. Този обзор засяга и проблемите, които трябва да бъдат решени за такива астрофизични обекти.

Bulgarian Academy of Sciences. Space Research Institute.
Aerospace Research in Bulgaria. 23, 2009, Sofia

THIN VISCOUS ELLIPTICAL ACCRETION DISCS WITH ORBITS SHARING A COMMON LONGITUDE OF PERIASTRON. IV. PROOF OF THE HOMOGENEITY OF THE DYNAMICAL EQUATION, GOVERNING DISC STRUCTURE FOR ARBITRARY POWERS *n* IN THE VISCOSITY LAW $\eta = \beta \Sigma^n$

Dimitar Dimitrov

Space Research Institute - Bulgarian Academy of Sciences
e-mail: dim@mail.space.bas.bg

Abstract

We consider the models of elliptical accretion discs developed by Lyubarskij et al. [1] and discuss their specific properties. In particular, we emphasize on possible deviations from the Keplerian rotation, magnetorotational instability, external illumination of the disc, etc., which may take place with real accretion flows (as indicated by a lot of observations), but are not taken into account in the above theoretical constructions. According to the models, the viscosity coefficient η is adopted to have a power law form: $\eta = \beta \Sigma^n$ (β is a constant, Σ is the disc surface density). We investigate the dynamical equation, which is derived by Lyubarskij et al. [1], for a continuous set of values of the power n. Physically reasonable n occupy the zone between ≈ -1 and $\approx +3$. The basic result of our investigation is that the dynamical equation, governing the structure of elliptical discs, is a homogeneous second order ordinary differential equation for any values of n in the designated interval. This is a generalization of our previously established result for the case of integer values of n only.

Introduction

In this paper we continue the investigation of elliptical accretion discs described by Lyubarskij et al. [1] about 15 years ago. The essential feature of their model is that not only the disc particles have *elliptical* orbits,

but also the apse lines of all orbits are in line with each other. It would be stressed that it provides for changes in the eccentricity between adjacent streamlines. In other words, the eccentricities of the particle orbits may (in principle) vary for different parts of the accretion disc – its inner, middle and outer regions. The motion of the particles along the ellipses is supposed to be Keplerian and the dynamics of the disc is treated in the framework of viscous hydrodynamics. In fact, the above cited work [1] generalizes to some extent the well known α-disc model of Shakura and Sunyaev [2], where all particle orbits are *a priori* assumed to be circular. We shall consider in our investigation only the case of *stationary* accretion discs. The simplifications applied in the paper [1] lead to a second-order ordinary differential equation, which governs the structure of the accretion disc, namely, the dependence of eccentricity on the focal parameter p of the corresponding ellipse. The situation is not so favourable, in view of simplicity, in the more general models of elliptical discs considered by Ogilvie [3]. The base line followed by us is to study *analytically* these objects as much as possible in order to minimize the application of numerical methods and eventually, reveal more clearly some properties of the solutions. Despite of the property that the Ogilvie's model [3] is much more realistic and more appropriate to be checked by means of astronomical observations than earlier model of Lyubarskij et al. [1], we shall concentrate on the latter for the above mentioned reasons. Some results concerning the problem of solving of the dynamical equation for the accretion disc model of Lyubarskij et al. [1] were already published earlier in papers [4–9]. The present research may be considered as a supplement to the case of *integer* powers n [7] in the sense that now we shall consider arbitrary (but physically reasonable!) values of n, which *may not be integers*. More specifically, it will be allowed that $n \neq -1, 0, +1, +2, +3$. Of course, between integer values, n may vary continuously. We remind that, according to the adopted viscosity law $\eta = \beta \Sigma^n$ in the accretion disc model of Lyubarskij et al. [1], n is the power of the disc surface density Σ and it is allowed to take continuous (but later on fixed!) values in some appropriate interval. The more general situation, when the power n eventually depends on some physical and geometrical factors like pressure, temperature, volume density, distance to the compact object, shape of the accretion disc and so on, is out of the scope of our investigation. Henceforth, the quantity n (and also the factor β) are considered to be constants and the variation of the viscosity

coefficient η throughout the disc is determined by the variation of its surface density Σ.

With the accumulation of observational data about accretion discs in binary stellar systems, it becomes more and more evident that the ellipticity of these objects is not only a possible theoretical construction, but it is often a phenomenon occurring in reality. The overview paper [10] gives some examples on this subject. We shall now add to this list of papers several more recent results concerning the theme of elliptical discs. Especially, we shall mention the photometric observations of Howell et al. [11] in the infrared region of the electromagnetic spectrum of the eclipsing interacting binary WZ Sge. There is evidence that the accretion flow in this stellar system is much more complex than previously suggested. The astronomical observations support the conclusion that that the so-far-known *gaseous* accretion disc is surrounded by an *asymmetric* disc of *dusty* material with a radius about 15 times larger than the outer radius of the gaseous disc. The dust disc contains only a small amount of mass and is completely invisible at optical and near-infrared wavelengths. Such discovery in respect to the structure of the *global* (gas + dust) disc has significant influence on accretion disc theory. It suggests the need of certain generalization of the model, advocated by Lyubarskij et al. [1], to “two-component disc” case, but we shall not deal with this problem here. Indications of the presence of an elliptical accretion disc are found in the X-ray binary star UW Coronae Borealis [12]. The interpretation of the light curve for this system is based on the assumption of eclipse of an accretion disc around a neutron star by the secondary star. The surface brightness of the accretion disc is strongly *asymmetric* and highly variable. Observations show that the variations of eclipse morphology are repeated at a period of 5.5 days and the shape of the superhump-like modulation also varies at this period. The model developed by Mason et al. [12] assumes elliptical distribution of surface brightness and, respectively, the disc precesses at the 5.5-day period in order to reproduce the eclipse depths and the times of mideclipse. The superhump-like variability phenomenon for the UW Coronae Borealis star may be explained reasonably well by an elliptical precessing disc. The paper of Ferreira and Ogilvie [13] considers warping and eccentric disturbances propagating inwards in discs around black holes under a wide variety of conditions. It is assumed that the deformations are stationary and propagate in a disc model similarly to the regions (a) (dominant radiation pressure; electron scattering on free electrons plays the main role) and (b) (dominant

gas pressure; electron scattering accounts for the main contribution to opacity) of Shakura and Sunyaev discs [2]. This investigation shows that the propagation of warping and eccentric deformations to the innermost regions of the disc is favoured by the low viscous damping and the high accretion rate.

Deviations from the Keplerian Rotation of Accretion Flows

The elliptical accretion disc model of Lyubarskij et al. [1] assumes the idea (and this concept is supported by the observations) that the discs are Keplerian, i.e., rotationally supported gaseous/dust discs. The common scenario, which naturally leads to the formation of Keplerian discs, is the viscous decretion model. According to it, discs are hydrodynamically supported in the vertical direction, while the radial structure is governed by viscous transport. This circumstance determines that the temperature is a primary factor that governs disc density structure. Of course, many physical and geometrical properties of accretion flows depend on the central stars around which discs rotate. For example, Carciofi et al. [14] discuss the basic hydrodynamics that determines the density structure of the discs around hot stars and solve the full problem of the *steady* state nonisothermal viscous diffusion and vertical hydrostatic equilibrium. They find that for Keplerian viscous discs, the self-consistent solutions depart significantly from the analytic isothermal density, which may have potentially large effects on the emergent spectrum. The implication is that for detailed modelling of Be star discs, nonisothermal disc models must be used. But in the opposite case, Shu et al. [15] find that strong magnetization makes the discs surrounding young stellar objects to rotate at rates that are too sub-Keplerian to enable the thermal launching of disc winds from their surfaces. An exception is observed when the rate of gas diffusion across field lines is dynamically fast. Another study [16] also supports the possibility of non-Keplerian motion in the inner regions of accretion discs around compact objects (i.e., the orbital frequency of the gas deviates from the *local* Keplerian value). It is shown that for long-wavelength modes in this region, the *radial* epicyclic frequency k is higher than the *azimuthal* frequency Ω. This circumstance may have significant implications for models of the twin kilohertz quasi-periodic oscillations observed in many neutron star sources. Hence, it can be subject to observational verifications. Deviations from the Keplerian velocity law are able to cause various kinds of instabilities, which are not taken into account in the model of Lyubarskij et al. [1] considered by us.

For example, in the paper of Barranko [17] it is shown that, as the dust in a protoplanetary disc settles, a vertical shear develops. The reason for this phenomenon is that the dust-rich gas in the midplane of the accretion disc orbits at a rate closer to the Keplerian velocity than the slower moving dust-depleted gas above and below the midplane. The classical analysis (i.e., neglecting the Coriolis force and differential rotation) performed by Barranko [17] predicts that Kelvin-Helmholtz instability occurs when the Richardson number of the stratified shear flow is $\leq 1/4$. Planets embedded in optically thick passive accretion discs are also expected to produce perturbations in the density and temperature structure of the disc. The calculated magnitudes of these perturbations for a range of planet masses and different radial distances from the center of the disc are given in [18]. It is demonstrated that a self-consistent calculation of the density and temperature structure of the accretion flow has great effect on the disc model. In addition, the temperature structure in the disc is highly sensitive to the angle of incidence of stellar irradiation at the surface. Therefore, the accurate calculation of the *shape* of the disc surface is crucial for modelling the disc's thermal structure. In this connection it is worthy to note that the model of Lyubarskij et al. [1] does not take into account the external illumination of elliptical accretion discs.

The investigation of the magnetorotational instability and its evolution in protoplanetary discs that have radial non-uniform magnetic field which allow stable and unstable regions to coexist *initially* is considered in paper [19]. It is found that a zone in which the disc gas rotates with a super-Keplerian velocity emerges as a result of the non-uniformly growing magnetorotational turbulence. It is also established that the original Keplerian shear flow is transformed to a quasi-steady flow such that more flattened (even with *rigid* rotation in the *extreme* cases) velocity profile emerges *locally* and the *outer* part of the velocity profile tends to be super-Keplerian. According to Kato et al. [19], angular momentum and mass transfer due to temporally generated magnetorotational instability turbulence in the initially unstable region are responsible for this transformation. Since the paper of Lyubarskij et al. [1] (and, consequently, our investigations, which are based on it) does not include the latter factor, we shall very briefly discuss in the next section how this simplification affects the accretion disc structure and how it restricts the applicability of this model. Of course, we must have in mind that the other approximations are also essential.

Significance of Magnetic Instabilities for the Realistic Description of Accretion Disc Models around Stellar Mass Objects

Let us take into consideration the work of Nekrasov [20] where electromagnetic streaming instabilities of multicomponent collisional *magnetized* accretion discs are studied. In this paper, sufficiently ionized regions of the disc are explored because there is strong collisional coupling of neutral atoms with both ions and dust grains simultaneously. The *steady state* is investigated in details and the azimuthal and radial background velocities of the species are calculated. The azimuthal velocities of ions, dust grains and neutral particles are found to be less than the Keplerian velocity. Concerning the radial velocities of the latter and the dust grains, it is shown that they are directed inward of the disc. Also, the dispersion relation for the vertical perturbations is derived and its unstable solutions, due to different background velocities of ions and electrons, are established [20]. It is found that the growth rates of the considered streaming instabilities can be much larger than the Keplerian frequency.

The accretion disc model of Lyubarskij et al. [1] is developed on the basis of classical Newtonian mechanics, i.e. general relativistic effects are not taken into account. But these may be essential in the near vicinities of compact objects. Consequently, by the notation "inner boundary"/ "innermost radius" of the accretion disc (respectively, "the smallest parameter" p_{min} (or p_{in}) of the elliptical disc) we shall mean such a value of the parameter p which marks the boundary closest to the central star, inside which the considered disc models are not already so good approximations as for the outer parts of the disc. Unfortunately, the general relativistic constraints are not the only factors that are able to impose restrictions on the reasonable validity of the model in the innermost regions of accretion flow. It is not excluded at all that other physical conditions and geometrical arguments may "augment" the value of the "inner disc radius" beyond the limit placed by the general relativistic considerations. In this sense, it is worthy to note the recent investigation of Beckwith et al. [21], which examines general relativistic magnetohydrodynamic simulations of black hole accretion. They find significant magnetic stresses near and inside the innermost stable circular orbit, which implies that such flows could radiate in a manner noticeably different from the prediction of the standard α-model of Shakura and Sunyaev [2]. The latter model assumes that in these regions

there are not stresses. Beckwith et al. [21] obtain estimates of how phenomenologically important parameters like the “radiation edge” (i.e., the innermost ring of the disc from which substantial thermal radiation escapes to infinity) may be altered near the innermost stable circular orbit. Their estimates are based on a large number of 3D general relativistic magnetohydrodynamic simulations combined with general relativity ray tracing. For slowly spinning black holes, the radiation edge lies well inside where the standard α-disc model [2] predicts, particularly when the stellar system is viewed at high inclination. For more rapidly spinning black holes, the contrast is established to be smaller. It is estimated in [21] that for a fixed total luminosity, the characteristic temperature of accretion flow increases by a factor between 1.2 and 2.4 over that predicted by the standard model [2]. If the mass accretion rate is fixed, there is a corresponding enhancement of accretion luminosity, which may be anywhere from tens of percent to the order of unity [21].

In our investigation, we are dealing with *stationary* (i.e., *steady state*) models of accretion discs. But we must keep in mind that the more realistic descriptions take into account different kinds of instabilities. For this reason, we shall add some remarks concerning this item in order to emphasize to some extent the limitations inherent to our model. For example, when the accretion rate is more than a small fraction of the Eddington rate dM_{Edd}/dt, the inner regions of the accretion discs around black holes are expected to be radiation-dominated. However, in the α-models [1,2] these regions are, in addition, thermally unstable. In the 3D radiation magnetohydrodynamic simulations of a vertically stratified shearing box (ratio of radiation to gas pressure $p_{rad}/p_g \sim 10$) performed by Hirose et al. [22], no thermal runaway occurs over a timespan of 40 cooling times t_{cool}. They observe that stress and total pressure are well correlated as predicted by the α-model [2], but stress *fluctuations* precede pressure *fluctuations*, contrary to the common suggestion that pressure controls the saturation level of magnetic energy. According to [22], this circumstance determines the thermal stability of the accretion flow. When the *thin* accretion discs around black holes are perturbed, the main restoring force is gravity. The authors of paper [23] state that, if gas pressure, magnetic stresses and radiation pressure are neglected, the disc remains *thin* as long as the particle orbits do not intersect (this condition *is fulfilled by hypothesis* in the model of Lyubarskij et al. [1] !). They also find that a discrete set of perturbations is possible for which orbits remain non-intersecting for

arbitrarily long times. Correspondingly, these models define a discrete set of perturbations.

According to [24], accretion discs in which angular momentum transport is dominated by magnetorotational instability may also possess additional (*purely hydrodynamic*) turbulence drivers. Even when the hydrodynamic processes themselves generate negligible levels of transport, they may still affect the disc's evolution through their influence on magnetorotational instability. The conclusion is that the impact of hydrodynamic turbulence is generically subject to ignorance only in some cases. Such a phenomenon is convection, where additional turbulence arises due to the accretion energy released by magnetorotational instability alone. Hydrodynamic turbulence may affect (either enhance or suppress) magnetorotational instability, if it is both strong and driven by independent mechanisms, such as self-gravity, supernovae explosions or solid(dust) particles-gas interactions in multiphase protoplanetary discs [24].

With the above notes about the adopted simplifications, which are intrinsic to standard α-disc models [1,2], we now begin to consider a very concrete problem, namely, the transformation of the dynamical equation for elliptical accretion discs (derived by Lyubarskij et al. [1]) to a more simple form. The main purpose of our approach is to do this in *purely analytical way*. It may come out that the final results of our attempts do not provide successfully to express this equation in a form, which allows solving it by means of the known standard methods from the theory of ordinary differential equations. But even in this pessimistic scenario, we hope that this will reveal some properties of the physical and mathematical structure of the disc model [1].

The Dynamical Equation and the Specific Characteristics of Its Terms

For clarity of subsequent computations, we rewrite here the dynamical equation governing the structure of elliptical accretion discs (with orbits of their species sharing a common longitude of periastron; [1]) in the form which was already derived in the previous paper [6]:

$$(1)\qquad \sum_{i,k} \mathbf{A}_{ik}(e,\dot{e},n)\, \mathbf{I}_i(e,\dot{e},n)\, \mathbf{I}_k(e,\dot{e},n)\, \ddot{e} + \sum_{l,m} \mathbf{B}_{lm}(e,\dot{e},n)\, \mathbf{I}_l(e,\dot{e},n)\, \mathbf{I}_m(e,\dot{e},n)\, \dot{e} = 0,$$

where the indices i, k, l and m independently take the values of 0─, 0+, 0, 1, 2, 3 and 4. The eccentricity e of the ellipse of each particle trajectory and its derivative $\dot{e} = de/du \equiv de/d(lnp)$ with respect to the logarithmic scale $u \equiv lnp$ of the focal parameter p of the ellipse, are (strictly speaking) functions of u and the power n in the viscosity law $\eta = \beta \Sigma^n$. According to the agreement made in the beginning of the present paper, we shall assume in what follows, that n is an arbitrarily chosen *fixed* non-integer number. That is to say, the quantity n does not vary along the values of the focal parameter p (the "radius" of the disc). Naturally, the convention that n is the same for all parts of the accretion disc, simplifies greatly the mathematical treatment of the problem. Consequently, for every previously selected (and after that fixed !) value of n between $\approx$ -1 and $\approx$ +3, we shall consider e and $\dot{e}$ as functions depending only on $u \equiv lnp$. We rewrite the definitions of the integrals $\mathbf{I}_{0-}$, $\mathbf{I}_{0+}$, $\mathbf{I}_0$, $\mathbf{I}_1$, $\mathbf{I}_2$, $\mathbf{I}_3$ and $\mathbf{I}_4$ [6]:

$$(2) \qquad \mathbf{I}_{0-}(e,\dot{e},n) \equiv \int_0^{2\pi} (1 + e\cos\varphi)^{n-3} [1 + (e - \dot{e})\cos\varphi]^{-(n+1)} \, d\varphi \, ,$$

$$(3) \qquad \mathbf{I}_{0+}(e,\dot{e},n) \equiv \int_0^{2\pi} (1 + e\cos\varphi)^{n-2} [1 + (e - \dot{e})\cos\varphi]^{-(n+2)} \, d\varphi \, ,$$

$$(4) \qquad \mathbf{I}_j(e,\dot{e},n) \equiv \int_0^{2\pi} (\cos\varphi)^j \, (1 + e\cos\varphi)^{n-2} [1 + (e - \dot{e})\cos\varphi]^{-(n+1)} \, d\varphi \, ;$$

$$j = 0, 1, 2, 3, 4.$$

The appearance of the above seven integrals in dynamical equation (1) is related to the averaging over the azimuthal angle φ, as proceeded in the model of elliptical accretion discs [1]. The other quantities to appear in equation (1) are the coefficients $\mathbf{A}_{ik}(e,\dot{e},n)$ and $\mathbf{B}_{lm}(e,\dot{e},n)$, which are known functions of e, $\dot{e}$ and n. Their writing in explicit form is too long to be given here and we shall miss this procedure in order to save unnecessary tedious formulae. We stress that the main purpose of the present paper is not to investigate the known functions $\mathbf{A}_{ik}$ and $\mathbf{B}_{lm}$, but to overcome the difficulties generated by the presence of these seven integrals, $\mathbf{I}_{0-}$, $\mathbf{I}_{0+}$, $\mathbf{I}_0$,…, $\mathbf{I}_4$, in dynamical equation (1). It must be pointed out that both the coefficients $\mathbf{A}_{ik}$ and $\mathbf{B}_{lm}$ and the integrals $\mathbf{I}_{0-}$, $\mathbf{I}_{0+}$, $\mathbf{I}_0$,…, $\mathbf{I}_4$ are, as a final result, functions of the parameter $u \equiv lnp$. But actually, at this stage of the task's solving, we do not know the solution(s) of equation (1). ***This is just our final goal*** **!** For

this reason, we shall assume in what follows {e, $\dot{e}$ and n = preliminary fixed constant} to be independent variables, having however in mind that differentiation of e with respect to u (we note this by a dot ($\dot{}$)) gives $\dot{e}$. Because $\dot{e}$ may also depend on u, it is again true that $d\dot{e}/du = \ddot{e}(u)$. These properties must be taken into account when the above-considered coefficients and integrals, participating in the subject-to-simplifications equation (1) undergo differentiation with respect to $e(u)$ or $\dot{e}(u)$.

Proof that the Dynamical Equation Is a Second-Order *Homogeneous* Ordinary Differential Equation

In the original deriving of the dynamical equation, which determines the structure of elliptical discs with orbits sharing a common longitude of periastron, Lyubarskij et al. include a free term ([1], equation (45)):

$$(5) \quad \mathbf{F}(e,\dot{e},n) \equiv \mathbf{Y}[(3/2)\mathbf{W} - \mathbf{Z} - (1/2)(1 - e^2)\mathbf{Y}] ,$$

The bars above **Y**, **Z** and **W** (which are present in paper [1], but are *omitted* in our notations for typographical technical reasons) denote averaging over the azimuthal angle φ. At first sight, it seems that this expression (5) stipulates the dynamical equation ([1], equation (45)) to be an inhomogeneous differential equation. For accretion discs with constant eccentricity of particle orbits ($\dot{e}(u) \equiv 0$; correspondingly $\ddot{e}(u) \equiv 0$ throughout the disc) it is obvious from ([1],equation (45)) that the free term $\mathbf{F}(e,\dot{e},n)$ (5) vanishes in a similar way for the entire disc. In the earlier paper [7], the explicit expressions for the auxiliary functions $\mathbf{Y}(e,\dot{e},n)$, $\mathbf{Z}(e,\dot{e},n)$ and $\mathbf{W}(e,\dot{e},n)$ were given for *integer* values of n (n = -1, 0, +1, +2, +3) ([7], equations (7a) – (11c)). Proving the homogeneity of the dynamical equation in the latter case was based on a little different approach. There is no necessity for the free term $\mathbf{F}(e,\dot{e},n)$ to be identically equal to zero. It is enough to show that $\mathbf{F}(e,\dot{e},n)$ factorizes and one of the factors is just the derivative of the eccentricity $\dot{e}(u) \equiv de/du$. Further on, $\mathbf{F}(e,\dot{e},n)$ can be "absorbed" into the term $\{\mathbf{Y}(e,\dot{e},n)[\partial\mathbf{Z}(e,\dot{e},n)/\partial e] - \mathbf{Z}(e,\dot{e},n)[\partial\mathbf{Y}(e,\dot{e},n)/\partial e] - \mathbf{Y}^2(e,\dot{e},n)e\}\dot{e}$ ([1], equation (45)), which also contains as a common factor the first derivative $\dot{e}(u)$. This implies that equation (45), established by Lyubarskij et al. [1], is in fact, a second-order *homogeneous* ordinary differential equation. In paper [7], factorization of the free term $\mathbf{F}(e,\dot{e},n)$ is evident from its explicit computation thanks to the already analytically evaluated expressions for integrals $\mathbf{I}_{0-}$, $\mathbf{I}_{0+}$, $\mathbf{I}_0$, $\mathbf{I}_1$, $\mathbf{I}_2$, $\mathbf{I}_3$ and $\mathbf{I}_4$ (see equations

(2a)–(6h) from [7]). There, it was only noticed that the proof of the homogeneity of the dynamical equation may be also generalized to the case of non-integer values of the power n. We shall now give a proof of this statement. We shall take into account the circumstance that we do not know (at least at the present time!) any analytical evaluations for non-integer n of the integrals $\mathbf{I}_{0-}$, $\mathbf{I}_{0+}$, $\mathbf{I}_0$, $\mathbf{I}_1$, $\mathbf{I}_2$, $\mathbf{I}_3$ and $\mathbf{I}_4$, defined by relations (2), (3) and (4).

Let us start with detailed derivation of the expressions for $\mathbf{Y}(e,\dot{e},n)$, $\mathbf{Z}(e,\dot{e},n)$ and $\mathbf{W}(e,\dot{e},n)$. *Here we make an important note***.** For technical/ typographical reasons, we denote by $\mathbf{Y}(e,\dot{e},n)$, $\mathbf{Z}(e,\dot{e},n)$ and $\mathbf{W}(e,\dot{e},n)$ the corresponding angle-averaged functions defined by equation (42) in the paper of Lyubarskij et al. [1], and denoted by barred gothic capital letters. This is, of course, evident when we write the free term $\mathbf{F}(e,\dot{e},n)$ (5) in our paper and compare it with the notations in the dynamical equation (45) in [1]. Consequently, our notations $\mathbf{Y}(e,\dot{e},n)$, $\mathbf{Z}(e,\dot{e},n)$ and $\mathbf{W}(e,\dot{e},n)$ *must not be erroneously identified* with the same designated quantities in [1] (equations (35), (36) and (38)). The latest we shall rewrite as:

$$(6)\qquad \mathbf{Y}_1(e,\dot{e},\varphi) \equiv -(2/3)(GMp)^{-1/2}\, g\, r^p \sigma^{p\varphi},$$

$$(7)\qquad \mathbf{Z}_1(e,\dot{e},\varphi) \equiv -(2/3)(GM/p)^{-1} \mathrm{V}_i \sigma^{pi}\, g^{1/2},$$

$$(8)\qquad \mathbf{W}_1(e,\dot{e},\varphi) \equiv (2/9)(GM/p^2)^{-1} \sigma_{i\,k}\, \sigma^{i\,k}\, g^{1/2}.$$

Note that these functions $\mathbf{Y}_1$, $\mathbf{Z}_1$ and $\mathbf{W}_1$ *do not depend* on the power n (see expressions (A5), (A7), (A12), (A14) and (A16) from Appendix A of [1]; see also formulae (9), (10) and (11) bellow in this paper). In the above formulae (6)–(8), G is the Newton's gravitational constant, M is the mass of the central star around which the accretion disc rotates, p is the focal parameter of the considered elliptical particle orbit. To describe the problem, non-orthogonal curvilinear coordinates (p, φ) are used instead of Cartesian ones (x, y). Correspondingly, V_i ($i = p, \varphi$) are the covariant components of the Keplerian velocity, $\sigma_{i\,k}$ and $\sigma^{i\,k}$ ($i, k = p, \varphi$) are the covariant and contravariant components of the shear tensor $\boldsymbol{\sigma}$, g is the determinant of the metric tensor and r^p is the contravariant p-component of the radius vector $\boldsymbol{r}$. We perform in advance: (i) correction of some typographical errors and (ii) simplification of some expressions in Appendix A to Lyubarskij et al. [1]. For example, the right-hand side of the formula for the trace of the shear tensor $\sigma \equiv \sigma_{i\,k}\, \sigma^{i\,k}$ ([1], equation (A16)) may be

factorized. The substitution of the final results in (6)–(8) gives the following representations about the auxiliary functions:

(9) $3\mathbf{Y}_1(e, \dot{e}, \varphi) = (1 + e\cos\varphi)^{-2}[1 + (e - \dot{e})\cos\varphi]^{-1}(3 + 7e\cos\varphi + e^2 + 4e^2\cos^2\varphi + e^3\cos\varphi - 4\dot{e}\cos\varphi + 2e\dot{e} - 8e\dot{e}\cos^2\varphi - 2e^2\dot{e}\cos\varphi)$,

(10) $3\,\mathbf{Z}_1(e, \dot{e}, \varphi) = (1 + e\cos\varphi)^{-2}[1 + (e - \dot{e})\cos\varphi]^{-1}(3 + 13e\cos\varphi + 22e^2\cos^2\varphi + 2e^3\cos\varphi + 16e^3\cos^3\varphi + e^4 + 2e^4\cos^2\varphi + 4e^4\cos^4\varphi + e^5\cos\varphi - 4\dot{e}\cos\varphi - 2e\dot{e} - 12e\dot{e}\cos^2\varphi - 6e^2\dot{e}\cos\varphi - 12e^2\dot{e}\cos^3\varphi - 2e^3\dot{e} - 4e^3\dot{e}\cos^2\varphi - 2e^4\dot{e}\cos\varphi - 4e^3\dot{e}\cos^4\varphi)$,

(11) $9\,\mathbf{W}_1(e, \dot{e}, \varphi) = (1 + e\cos\varphi)^{-2}[1 + (e - \dot{e})\cos\varphi]^{-1}(9 + 33e\cos\varphi - 2e^2\cos^2\varphi - 2\,e^3\cos\varphi + 32e^3\cos^3\varphi + e^4 + 8e^4\cos^4\varphi + e^5\cos\varphi - 24\dot{e}\cos\varphi + 4e\dot{e} - 72e\dot{e}\cos^2\varphi + 4e^2\dot{e}\cos\varphi - 72e^2\dot{e}\cos^3\varphi - 4e^3\dot{e} - 24e^3\dot{e}\cos^4\varphi - 4e^4\dot{e}\cos\varphi + 8\dot{e}^2 + 8\dot{e}^2\cos^2\varphi + 8e\dot{e}^2\cos\varphi + 24e\dot{e}^2\cos^3\varphi + 4e^2\dot{e}^2 + 16e^2\dot{e}^2\cos^4\varphi + 4e^3\dot{e}^2\cos\varphi)$.

From Appendix A ([1], equations (A5) and (A12)), we also compute:

(12) $(g^{1/2}\,\mathrm{V}^{\varphi})^n = (GM/p)^{n/2}\,(1 + e\cos\varphi)^{-n}[1 + (e - \dot{e})\cos\varphi]^n$.

Then, following definitions (40) and (42) from the paper of Lyubarskij et al. [1], we can write the new auxiliary functions (depending already on n):

(13) $\mathbf{Y}_2(e, \dot{e}, n, \varphi) \equiv \mathbf{Y}_1(e, \dot{e}, \varphi)(g^{1/2}\,\mathrm{V}^{\varphi})^{-n}$,

(14) $\mathbf{Z}_2(e, \dot{e}, n, \varphi) \equiv \mathbf{Z}_1(e, \dot{e}, \varphi)(g^{1/2}\,\mathrm{V}^{\varphi})^{-n}$,

(15) $\mathbf{W}_2(e, \dot{e}, n, \varphi) \equiv \mathbf{W}_1(e, \dot{e}, \varphi)(g^{1/2}\,\mathrm{V}^{\varphi})^{-n}$,

We stress again that in our notations the symbol "dot" ($\dot{}$) means differentiation with respect to the variable $u \equiv \ln p$, ***not*** with respect to the time t. Finally, the averaging over the azimuthal angle φ yields the expressions for $\mathbf{Y}(e,\dot{e},n)$, $\mathbf{Z}(e,\dot{e},n)$ and $\mathbf{W}(e,\dot{e},n)$ we are seeking for:

(16) $3\mathbf{Y}(e,\dot{e},n) \equiv (3/(2\pi))\int_0^{2\pi}\mathbf{Y}_2(e, \dot{e}, n, \varphi)d\varphi = (2\pi)^{-1}(p/GM)^{n/2}[(3 + e^2 + 2e\dot{e})\mathbf{I}_0 + (7e + e^3 - 4\dot{e} - 2e^2\dot{e})\mathbf{I}_1 + (4e^2 - 8e\dot{e})\mathbf{I}_2]$,

(17) $3\mathbf{Z}(e,\dot{e},n) \equiv (3/(2\pi))\int_0^{2\pi}\mathbf{Z}_2(e, \dot{e}, n, \varphi)d\varphi = (2\pi)^{-1}(p/GM)^{n/2}[(3 + e^4 - 2e\dot{e}$

$-2e^3\dot{e})\mathbf{I}_0 + (13e + 2e^3 + e^5 - 4\dot{e} - 6e^2\dot{e} - 2e^4\dot{e})\mathbf{I}_1 + (22e^2 + 2e^4 - 12e\dot{e} - 4e^3\dot{e})\mathbf{I}_2 + (16e^3 - 12e^2\dot{e})\mathbf{I}_3 + (4e^4 - 4e^3\dot{e})\mathbf{I}_4]$,

(18) $9\mathbf{W}(e,\dot{e},n) \equiv (9/(2\pi))\int_0^{2\pi}\mathbf{W}_2(e, \dot{e}, n, \varphi)d\varphi = (2\pi)^{-1}(p/GM)^{n/2}[(9 - 2e^2 + e^4 + 4e\dot{e} - 4e^3\dot{e} + 8\dot{e}^2 + 4e^2\dot{e}^2)\mathbf{I}_0 + (33e - 2e^3 + e^5 - 24\dot{e} + 4e^2\dot{e} - 4e^4\dot{e} + 8e\dot{e}^2 + 4e^3\dot{e}^2)\mathbf{I}_1 + (48e^2 - 72e\dot{e} + 8\dot{e}^2)\mathbf{I}_2 + (32e^3 - 72e^2\dot{e} + 24e\dot{e}^2)\mathbf{I}_3 + (8e^4 - 24e^3\dot{e} + 16e^2\dot{e}^2)\mathbf{I}_4]$.

In deriving the last three expressions, we took into account definitions (4) of the integrals $\mathbf{I}_j(e, \dot{e}, n)$, (j = 0, 1, 2, 3, 4). Having already the results (16)–(18), it is simple to calculate the free term $\mathbf{F}(e,\dot{e},n)$:

(19) $18\mathbf{F}(e,\dot{e},n) \equiv (3\mathbf{Y})[9\mathbf{W} - 2(3\mathbf{Z}) + (e^2 - 1)(3\mathbf{Y})] = (2\pi^2)^{-1}(p/GM)^n \boldsymbol{\dot{e}}$ $[(9e + 6e^3 + e^5 + 12\dot{e} + 16e^2\dot{e} + 4e^4\dot{e} + 8e\dot{e}^2 + 4e^3\dot{e}^2)\mathbf{I}_0^2 + (-18 + 36e^2 + 14e^4 + 16e\dot{e} + 32e^3\dot{e} - 16\dot{e}^2 - 8e^2\dot{e}^2)\mathbf{I}_1\mathbf{I}_0 + (-42e + 43e^3 - e^7 + 24\dot{e} + 12e^2\dot{e} + 8e^4\dot{e} + 4e^6\dot{e} - 16e\dot{e}^2 - 16e^3\dot{e}^2 - 4e^5\dot{e}^2)\mathbf{I}_1^2 + (-60e - 8e^3 + 4e^5 + 12\dot{e} - 44e^2\dot{e} - 24e\dot{e}^2 - 16e^3\dot{e}^2)\mathbf{I}_2\mathbf{I}_0 + (-164e^2 + 8e^4 - 4e^6 + 156e\dot{e} + 4e^3\dot{e} + 16e^5\dot{e} - 16\dot{e}^2 - 40e^2\dot{e}^2 - 16e^4\dot{e}^2)\mathbf{I}_2\mathbf{I}_1 + (-80e^3 + 176e^2\dot{e} - 32e\dot{e}^2)\mathbf{I}_2^2 + (-72e^2 - 24e^4 + 36e\dot{e} - 36e^3\dot{e} + 24e^2\dot{e}^2)\mathbf{I}_3\mathbf{I}_0 + (-168e^3 - 24e^5 + 180e^2\dot{e} + 60e^4\dot{e} - 48e\dot{e}^2 - 24e^3\dot{e}^2)\mathbf{I}_3\mathbf{I}_1 + (-96e^4 + 240e^3\dot{e} - 96e^2\dot{e}^2)\mathbf{I}_3\mathbf{I}_2 + (-24e^3 - 8e^5 + 24e^2\dot{e} - 8e^4\dot{e} + 16e^3\dot{e}^2)\mathbf{I}_4\mathbf{I}_0 + (-56e^4 - 8e^6 + 88e^3\dot{e} + 24e^5\dot{e} - 32e^2\dot{e}^2 - 16e^4\dot{e}^2)\mathbf{I}_4\mathbf{I}_1 + (-32e^5 + 96e^4\dot{e} - 64e^3\dot{e}^2)\mathbf{I}_4\mathbf{I}_2]$.

The above complex and lengthy expression shows clearly that a common factor $\boldsymbol{\dot{e}}$ appears when factorization has been performed. It is worthy to note that we have not imposed any restrictions on the power n in the viscosity law $\eta = \beta\,\Sigma^n$. That is to say, the purely analytically derived result (19) is valid both for integer and non-integer values of n. As a final result, the "free" term $\mathbf{F}(e,\dot{e},n)$, given by definition (5), can be absorbed into the term $(\mathbf{Y}\partial\mathbf{Z}/\partial e - \mathbf{Z}\partial\mathbf{Y}/\partial e - \mathbf{Y}^2 e)\boldsymbol{\dot{e}}$ of the dynamical equation ([1], equation (45); call to mind that we are using other notations in the present paper, as mentioned earlier). This completes the proof that the dynamical equation, which determines the structural properties of stationary elliptical accretion discs *with apse lines of all orbits assumed to be in line with each other*, is a second-order *homogeneous* ordinary differential equation. This argument was taken into account when we wrote the dynamical equation in form (1).

Conclusions

As illustrated by relation (19), the coefficients $\mathbf{A}_{ik}(e, \dot{e}, n)$ and $\mathbf{B}_{lm}(e, \dot{e}, n)$, (i, k, l, m = 0─, 0+, 0, 1, 2, 3, 4) are expected to be very complex functions of their arguments e, $\dot{e}$ and n. Consequently, the homogeneity of dynamical equation (1) is far from the condition to be a sufficiently simplifying property, allowing for its easy (or without great difficulties) solving by means of purely analytical methods. For this reason, the necessity arises to find additional simplifications of equation (1), though there are no optimistic indications for such useful possibilities. Even in the case of integer values of the power n in the viscosity law $\eta = \beta \Sigma^n$, when each of the seven integrals $\mathbf{I}_{0-}$, $\mathbf{I}_{0+}$, $\mathbf{I}_0$, **…,** $\mathbf{I}_4$ may be found in an explicit analytical form, the dynamical equation can hardly be approximated by a differential equation with constant coefficients [7]. One possible approach to simplify further this equation is to try to find relations between these seven integrals, allowing us to exclude some of them in equation (1). In the simplest case we are to seek for linear ones. The attractivity of this idea increases when non-integer powers n are considered, because (at least at the present time) we do not even know any explicit analytical solutions of the integrals $\mathbf{I}_{0-}$, $\mathbf{I}_{0+}$, $\mathbf{I}_0$, **…,** $\mathbf{I}_4$. Dynamical equation (1) determines the structure of elliptical discs with particles sharing a common longitude of periastron. If the attempts to solve it to the very end by purely analytical methods appear to be unsuccessful, we nevertheless hope that the attained simplifications will allow us to accomplish some more problems. For example, the number of branch points of the solutions, the limitations imposed on the domains of the solutions, certain qualitative characteristics of theirs, etc. Of course, analytically simplified forms of (1) are probably preferred when numerical methods for solving are used.

In conclusion, we would line to make the following remark. Above we have written definitions (2) and (3) of the integrals $\mathbf{I}_{0-}(e, \dot{e}, n)$ and $\mathbf{I}_{0+}(e, \dot{e}, n)$, accordingly. At first sight, it may seem that this is an unnecessary supplement to definitions (4) of the integrals $\mathbf{I}_j(e, \dot{e}, n)$, (j = 0,1,…, 4). In fact, this information was not used when deriving the final expression (19). This is so because the latter result serves only to reveal the property that a factor $\dot{\boldsymbol{e}}$ appears, when the free term $\mathbf{F}(e, \dot{e}, n)$ is factorized. For this purpose, we do not perform any differentiations of integrals $\mathbf{I}_j(e, \dot{e}, n)$, (j = 0,1,…, 4). Such operations will lead to the appearance of $\mathbf{I}_{0-}(e, \dot{e}, n)$ and $\mathbf{I}_{0+}(e, \dot{e}, n)$, and, consequently, of their presence in dynamical equation (1). It can also be seen in explicit form, if we try to eliminate some of the integrals $\mathbf{I}_0$, $\mathbf{I}_1$,

…, $\mathbf{I}_4$ by deriving linear relations between them, including differentiation operations. This will be subject of a forthcoming paper and we provide definitions (2) and (3) mostly for completeness of the discussion.

References

1. L y u b a r s k i j Y u. E., K. A. P o s t n o v, M. E. P r o k h o r o v. Eccentric accretion discs., Monthly Not. Royal Astron. Soc., 266, 1994, № 2, p. 583–596.
2. S h a k u r a N. I., R. A. S u n y a e v. Black holes in binary systems. Observational appearance., Astron. & Astrophys., 24, 1973, № 3, p. 337–355.
3. O g i l v i e G. I. Non–linear Dynamics of eccentric discs., Monthly Not. Royal Astron. Soc., 325, 2001, № 1, p. 231–248.
4. D i m i t r o v D. V. Elliptical accretion discs with constant eccentricity. I. Case $\eta = \beta \Sigma^n$., Aerospace Research in Bulgaria, 14, 1998, p. 3–10.
5. D i m i t r o v D. V. Elliptical accretion discs with constant eccentricity. II. Standard α-disc model., Aerospace Research in Bulgaria, 15, 1999, p. 11–21.
6. D i m i t r o v D. V. One possible simplification of the dynamical equation governing the evolution of elliptical accretion discs., Aerospace Research in Bulgaria, 17, 2003, p. 17–22.
7. D i m i t r o v D. V. Thin viscous elliptical accretion discs with orbits sharing a common longitude of periastron. I. Dynamical equation for integer values of the powers in the viscosity law., Aerospace Research in Bulgaria, 19, 2006, p.16–28.
8. D i m i t r o v D. V. Thin viscous elliptical accretion discs with orbits sharing a common longitude of periastron. II. Polynomial solutions to the dynamical equation for integer values of the powers in the viscosity law., Aerospace research in Bulgaria, 21, 2007, p. 7–23.
9. D i m i t r o v D. V. Thin viscous elliptical accretion discs with orbits sharing a common longitude of periastron. III. Numerical evaluations of the validity domain of the solutions., Aerospace research in Bulgaria, 22, 2008, p. 5–23.
10. D i m i t r o v D. V. A short overview of some recent developments in the theory of non-axisymmetric accretion discs., Aerospace research in Bulgaria, 23, 2009, (in print).
11. H o w e l l S. B., D. W. H o a r d, C. B r i n k w o r t h, S. K a f k a, M. J. W a l e n t o s k y, F. M. W a l t e r, T. A. R e c t o r. “dark matter” in accretion disks., Astrophys. Journal, 685, 2008, № 1, part 1, p. 418–427.
12. M a s o n P. A., E. L. R o b I n s o n, C. L. G r a y, R. I. H y n e s. The orbital period and time-variable asymmetric accretion disk in the X–ray binary MS 1603.6 + 2600 (= UW Coronae Borealis)., Astrophys Journal, 685, 2008, № 1, part 1, p. 428–435.
13. F e r r e i r a B. T., G. I. O g i l v i e. Warp and eccentricity propagation in discs around black holes., Monthly Not. Royal Astron Soc., 392, 2009, № 1, p. 428–438.
14. C a r c i o f i A. C., J. E. B j o r k m a n. Non–LTE Monte Carlo radiative transfer. I I. Nonisothermal solutions for viscous Keplerian disks., Astrophys. Journal, 684, 2008, № 2, part 1, p. 1374–1383.

15. S h u, F, H., S. L i z a n o, D. G a l l i, M. J. C a i, S. M o h a n t y. the challenge of sub-Keplerian rotation for disk winds., Astrophys. J. Letters, 682, 2008, № 2, part 2, p. L121–L124.
16. A l p a r M. A., D. P s a l t i s. The highest dynamical frequency in the inner region of an accretion disc., Monthly Not. Royal Astron. Soc., 391, 2008, № 3, p. 1472–1476.
17. B a r r a n k o, J. A. Three–dimensional simulations of Kelvin–Helmholtz instability in settled dust layers in protoplanetary disks., Astrophys. Journal, 691, 2009, № 2, part 1, p. 907–921.
18. J a n g – C o n d e l H. Planet shadows in protoplanetary disks. I. Temperature perturbations., Astrophys. Journal, 679, 2008, № 1, part 1, p. 797–812.
19. K a t o M. T., K. N a k a m u r a, R. T a n d o k o r o, M., F u j i m o t o, S. I d a. Modifications of angular velocity by inhomogeneous magnetorotational growth in protoplanetary disks., Astrophys. Journal, 691, 2009, № 2, part 1, p. 1697–1706.
20. N e k r a s o v A. K. Electromagnetic streaming instabilities of magnetized accretion disks with strong collisional coupling of species., Astrophys. Journal, 695, 2009, № 1, part 1, p. 46–58.
21. B e c k w i t h, K., J. F. H a w l e y, J. H. K r o l i k. Where is the radiation edge in magnetized black hole accretion discs?, Monthly Not. Royal Astron. Soc., 390, 2008, № 1, p. 21–38.
22. H i r o s e S., J. H. K r o l i k, O. B l a e s. Radiation–dominated disks are thermally stable., Astrophys. Journal, 691, 2009, № 1, part 1, p. 16–31.
23. T a s s e v S. V., E. B e r s t s c h i n g e r. Kinematic density waves in accretion disks., Astrophys. Journal, 686, 2008, № 1, part 1, p. 423–431.
24. W o r k m a n J. C., P. J. A r m i t a g e. Interaction of the magnetorotational instability with hydrodynamic turbulence in accretion disks., Astrophys. Journal, 685, 2008, № 1, part 1, p. 406–414.

ТЪНКИ ВИСКОЗНИ ЕЛИПТИЧНИ АКРЕЦИОННИ ДИСКОВЕ С ОРБИТИ, ИМАЩИ ОБЩА ДЪЛЖИНА НА ПЕРИАСТРОНА. IV. ДОКАЗАТЕЛСТВО НА ХОМОГЕННОСТТА НА ДИНАМИЧНОТО УРАВНЕНИЕ, ОПРЕДЕЛЯЩО СТРУКТУРАТА НА ДИСКА, ЗА ПРОИЗВОЛНИ СТЕПЕННИ ПОКАЗАТЕЛИ n В ЗАКОНА ЗА ВИСКОЗИТЕТА $\eta = \beta \Sigma^n$

Димитър Димитров

Резюме

Ние разглеждаме моделите на елиптични акреционни дискове, разработени от Любаркий и др. [1], и дискутираме техните специфични свойства. В частност, ние наблягаме на възможните отклонения от

Кеплеровото въртене, магниторотационната нестабилност, външното осветяване на диска и т. н., които могат да имат място при реалните акреционни потоци (както е указано при много от наблюденията), но които не са взети под внимание в горните теоретични конструкции. Съгласно моделите, коефициентът на вискозитета η е прието да има формата на степенен закон: $\eta = \beta \Sigma^n$ (β е константа, Σ е повърхностната плътност на диска). Ние изследваме динамичното уравнение, което е получено от Любаркий и др. [1], за едно непрекъснато множество от стойности на степенния показател n. Физически приемливите значения на n обхващат областта между $\approx$ - 1 и $\approx$ + 3. Основният резултат на нашето изследване е, че динамичното уравнение, определящо структурата на елиптичните дискове, е едно ***хомогенно*** обикновено диференциално уравнение от втори ред за ***всички*** стойности на n в посочения интервал. Това е обобщение на нашия по-рано установен резултат за случая ***само на целочислени*** стойности на n.

Bulgarian Academy of Sciences. Space Research Institute.
Aerospace Research in Bulgaria. 23, 2009, Sofia

ATMOSPHERIC GRAVITY WAVES ASSOCIATED WITH THE SOLAR TERMINATOR'S MOVING THROUGH THE EARTH'S UPPER ATMOSPHERE

Georgii Lizunov[1], Alla Fedorenko[1], Ludmil Bankov[2], Any Vassileva[2]

[1] Space Research Institute - NSAU, Ukraine
e-mail: liz@ikd.kiev.ua
[2] Space Research Institute –Bulgarian Academy of Sciences
e-mail: ludmil.bankov@gmail.com

Abstract

Upper atmosphere dynamical response to moving solar terminator is investigated based on direct satellite measurements. The observations on Atmosphere Explorer-E are analyzed over the period when the satellite was positioned on circular near-equatorial orbit with inclination of $i = 19.7°$ and height of 250-300 km. It is shown that the terminator generates large-scale atmosphere gravity waves (AGW) and travelling ionosphere disturbances (TID) with the following parameters: 1) the horizontal wavelength is close to 1200-1600 km; 2) the calculated period is about 50 minutes; 3) the duration of AGW/TID train is four-six wave periods; 4) the relative amplitude of the AGW is several percents; 5) the relative amplitude of TID at sunrise terminator is about several percents, at sunset terminator – up to ten percents; 6) plasma density oscillations $[O^+]$ are generated in opposite phase with the oscillations of the main neutral components $[N_2]$, $[O]$; molecular ion densities $[NO^+]$ and $[O_2^+]$ oscillate in phase with the neutrals. The obtained experimental results are interpreted based on the theory of AGW propagation in multi-component gas medium. It is shown that the amplitude and phase distinctions of the oscillations of the atmospheric components (including the main ionic component O^+) are caused by differences in the vertical distributions of atmosphere gases above the turbo-pause.

Introduction

The first theoretical suggestion on the possible generation of Atmospheric Gravity Waves (AGWs) by the solar terminator is made in [1]. The ionospheric response to the moving terminator as a Travelling

Ionospheric Disturbance (TID) has been the subject of a great number of ground-based observations [2, 3 and references therein]. In the present work, we study the process of wave generation at the solar terminator based on *in situ* measurements carried out on the *Atmosphere Explorer-E* (AE-E) satellite at the low latitude bottom side of F-region ionosphere. A diagram of the relative geometry of the AE-E orbit and the solar terminator position is shown in Fig.1.

In the Sun-Earth reference frame, neutral atmosphere co-rotating with the Earth crosses a steady terminator, which leads to the generation of a wave in associated day/night transition zone. As can be seen from Fig.1, in a given season, subsequent AE-E orbits cross the terminator zone and the wavelike structures attached to it in quite a similar manner. This in fact allows us to observe this wave with the periodicity of the satellite motion. In the late 70's and early 80's, complex satellite experiments were carried out to study ionosphere-thermosphere-magnetosphere interactions, such as *Atmosphere Explorer-C, D, E*, *Dynamics Explorer-B* etc. [4]. In the present work, we use AE-E data within the period of circular orbit at an altitude of 250-350 km and orbital inclination of 19.7^{o}. Such an orbital configuration of AE-E corresponds quite well to the studied terminator processes. First, satellite AE-E is at low Earth orbit (LEO) and second, because of the low orbital inclination, it crosses the wavelike train generated by the terminator (Fig.1). Most of the later "ionospheric" satellites, including nowadays DEMETER satellite, are launched at higher orbits (more than 700 km), well above the heights of AGW/TID propagation.

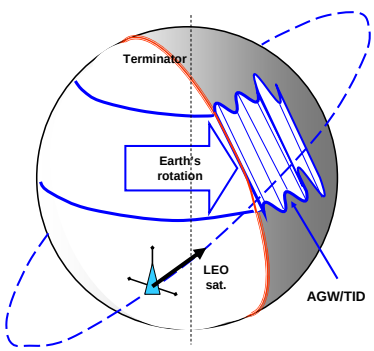

Fig.1. A diagram of Low Earth's Satellite observational opportunities at the terminator is shown. The relative position of the satellite's orbit, the terminator and the generated wavelike structures changes with time only due to the orbital precession.

Optically, solar terminator is a surface, which divides daylight from night-time part of the atmosphere. At altitude of 300 km, the angle between the horizon and the optical terminator's surface is about 10°, the thickness of the twilight zone is 55 km and the equatorial velocity of the terminator relatively to the Earth's surface is $V_{ST} = 450$ m/s. We will call AGW/TID generation zone the physical terminator, which is spread eastward of the optical terminator with characteristic width $L \sim 1500$ km (nearly one-hour band in local time). The relative configuration of the optical and physical terminators is shown in Fig.2.

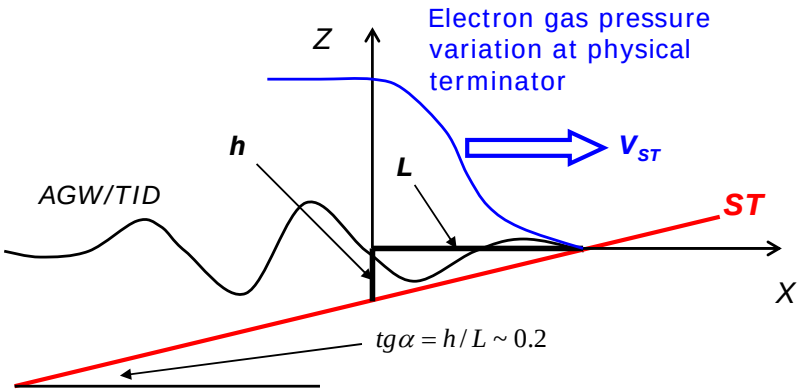

Fig. 2. Structure of the sunrise terminator. ST – optical terminator, between sunlight and dark night-side atmosphere. Wave generation appears in the region of solar energy accumulation with horizontal length scale L (at physical terminator).

The physical mechanisms of solar energy absorption which lead to the generation of atmospheric fluctuations are discussed in [5, 6]. At large solar zenith angles (at the terminator more than 90°), the main part of the energy in the UV band dissipates higher than 200 km. Because of the AGW's small group velocity, wave propagation upward and downward from the region of maximum absorption cannot explain the existence of neutral atmospheric disturbances at adjacent altitude layers, which are obviously generated independently by the terminator.

The structure of the work is as follows: Chapter 1 provides a simple explanation of the data processing procedure applied to the AE-E data; Chapter 3 contains a case study of several selected events; and Chapter 4 gives a theoretical interpretation of the observations.

1. Data processing technique

Here we use AE-E data taken from the database of the *National Space Science Data Center*, web-site: <http://nssdc.gsfc.nasa.gov/atmoweb>. As relevant parameters of the atmosphere around the F2 layer height have been chosen:

- neutral O and N_2 density;
- neutral temperature T_n;
- O^+ ion density;
- NO^+ и O_2^+ molecular ion density.

To study the wavelike disturbances generated by the moving terminator, we use a special data processing algorithm. While phase velocity of the AGW (hundreds of m/s) is small compared to the satellite orbital velocity of $V_{sat} \approx 8$ km/s, the frequency of the observed atmospheric disturbances is given by the wavelength spectrum: $\omega' = \omega - k_x V_{sat} \approx -k_x V_{sat}$, where ω – frequency of the AGW/TID in the stationary reference frame, $k_x = 2\pi / \lambda_x$ – wave vector component along the satellite's track, λ_x – horizontal wavelength. The smallest observable wavelength $\lambda_{\min}$ is determined by the Naiquist scale $\lambda_{\min} = 2 \cdot V_{sat} t_{sampl}$, where t_{sampl} is the data sampling time interval. In the case of AE-E, $t_{sampl} = 15$ s, $\lambda_{\min} = 240$ km. The maximal wavelength depends on the data processing method. We reduce our analysis to $\lambda_{\max} \sim 2000$ km in order to locate large scale AGW/ TID [7, 8].

The major problem of the undertaken data processing is related with wave selection against abrupt changes of the atmospheric parameters. Let us examine an example, which appears in sunrise ionosphere. Close after the terminator, within few hours, in the F-region, plasma density grows by more than an order of magnitude. In the same time, the terminator generates plasma fluctuations, a TID with relative amplitude of several percents, which forms a "small ripple" on the base gradient plasma density. In this case, to recognize the AGW, it is correct to extract trends from the data before calculating the spectral characteristics.

2. Data analysis

Data analysis of AE-E shows that in the morning hours after sunrise (for example 6-11 a.m. local time) and in the evening, after sunset (7-12 p.m. local time), a relative increase in wave activity is observed, which is

manifested as variations in the density and temperature of the different atmospheric species.

In Fig.3, a typical example of the wavelike disturbance on sunrise terminator is shown. Upon elimination of the large scale trends, we select the variations of the neutrals (AGW) and plasma (TID) with relative amplitudes $\delta[O]/[O] \sim 5\%$, $\delta[O^+]/[O^+] \sim 10\%$. It has to be pointed out that the main neutral components [O] и [N_2] vary in synchrony but with different relative amplitudes (amplitude ratio ~ 2). The wavelet transformation shows the presence of horizontal wavelength (about $\lambda_x = 1250$ km) and localizes the time interval within the observed wavelike activity (6-10 a.m. LT).

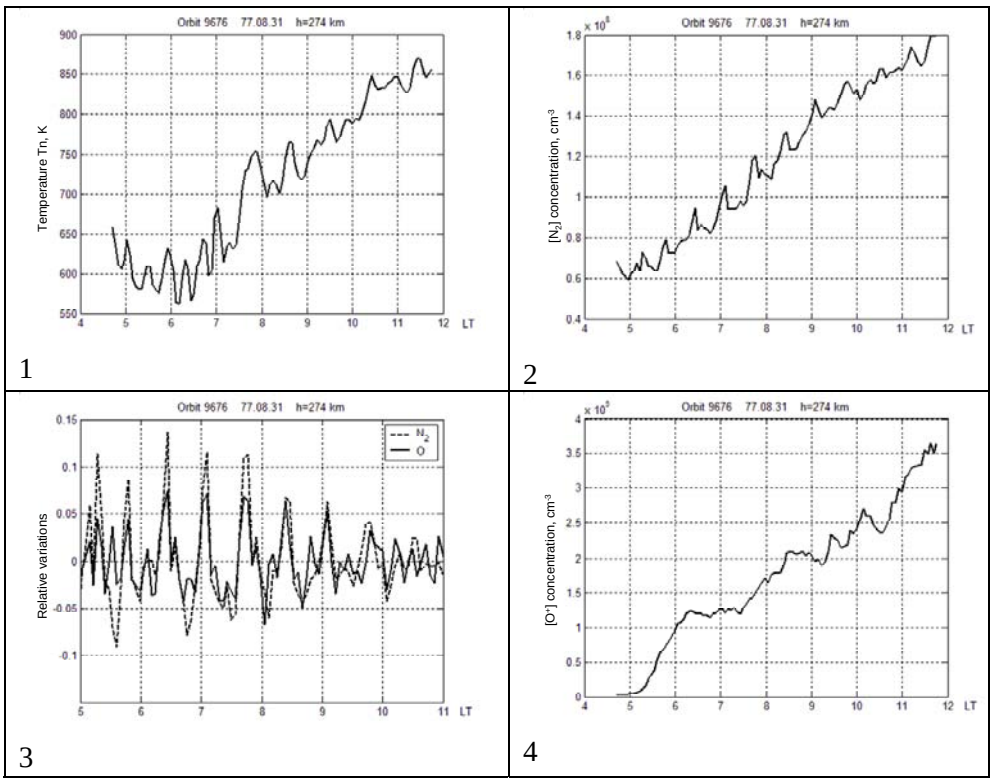

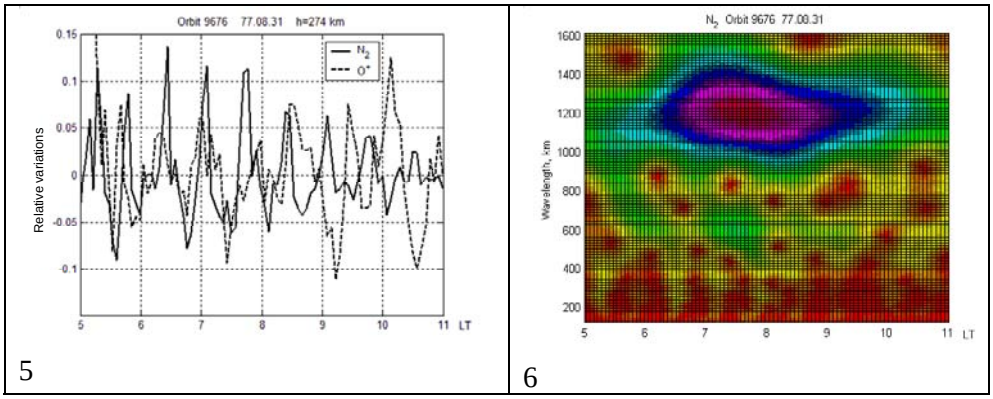

Fig.3. Atmospheric parameters behaviour at sunrise terminator, as observed at orbit 9796. Panels 1,2,4 – represent neutral temperature T_n, neutral density of $[N_2]$ and ion density of $[O^+]$; Panel 3 – smoothed relative variations of the neutral components; Panel 5 – neutral and plasma components; Panel 6 – wavelet spectrum of $[N_2]$ density variations

An example of the evening terminator fluctuations is shown in Fig.4. Upon elimination of the trends, relative variations in the neutrals and plasma are selected with characteristic size $\lambda_x \approx 1400$ km. The density of the major ion $[O^+]$ varies in anaphase with molecular ion density $[O^+_2]$ and $[NO^+]$. Latest in amplitude and phase follow the main neutral components.

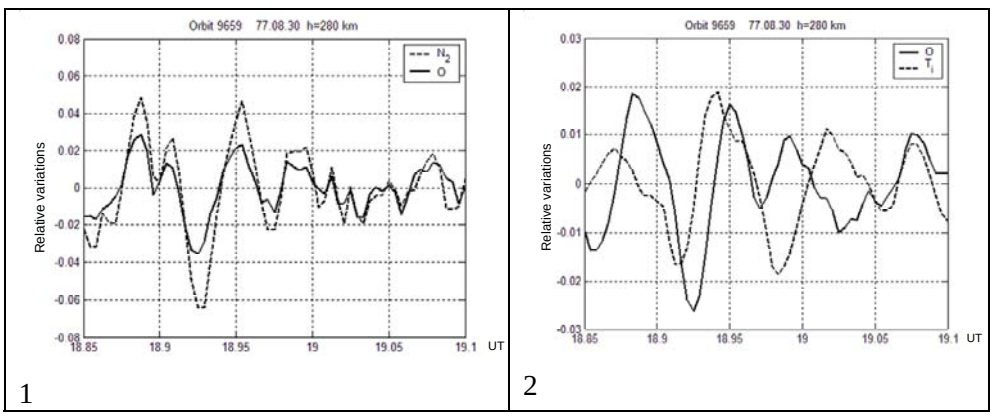

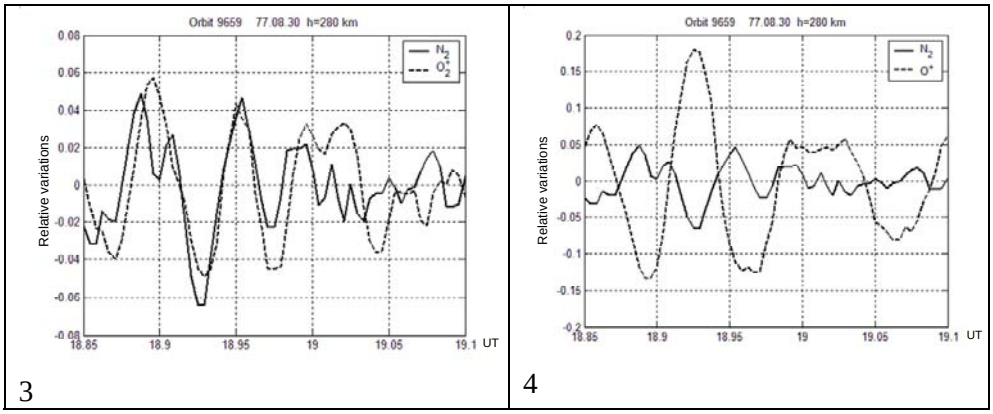

Fig.4. AGW/TID at evening terminator (7-9 p.m. LT). Panel 1,2 – relative density variations of the main neutral components and ion temperature Ti; Panel 3,4 – relative variations of different ion species vs. main neutral component [N_2] fluctuations

Following this procedure, we examined 8 cases at the terminator, which are summarized on Table 1. For sunrise and sunset conditions, the wavelengths almost coincide, the length of the wavelike zones of AGW/TID and the relative amplitudes of the AGW. The main peculiarity of the evening events is their larger plasma response amplitudes.

Table 1

Data	Orbit	h, km	Local time	Relative fluctuations, %						V_z, m/s	λ_x, km
				[N_2]	[O]	T_n	[O^+]	[NO^+]	[O_2^+]		
Dusk terminator											
77.04.23	7581	255	20-1^h	4	2	2	20	-	-	5	1400 + 2800
77.04.23	7583	255	20-3^h	6	3	3	15	-	-	7	1440
77.08.30	9659	280	19-24^h	5	3	-	20	5	5	10	1600
Dawn terminator											
77.04.19	7514	257	4-11^h	3	1,5	1	1	-	-	5	1600
77.07.28	9135	266	4-11^h	-	-	3	10	-	-	-	1500
77.08.31	9676	274	5-11^h	10	5	5	10	-	-	-	1250
77.10.08	10290	281	4.5-9.5^h	3	2	2	3	-	-	-	1400
78.03.19	12874	317	6-11^h	2	1	1	3	2	2	-	1300

To illustrate the repeatability of the behaviour of wavelike structures at the selected terminator described above, an additional example is shown in Fig. 5. One can see wave trains associated with evening terminator

observed from three different passes of AE-E at altitude of ~320 km in the longitudinal zone with geographic longitudes from -65° to -25°, during three subsequent days from March 10 to March 12, 1978. Data are matched along the local terminator position ST. Total ion density variations taken from IDM/RPA instrument have quite similar shape in the post sunset parts of the orbits on panel (a) on the left side of Fig.5. The dotted lines mark the smoothed density profile to extract the trends from data. In Fig.5 (b), the spectral power density of the smoothed profiles is shown for these three cases. Relative wavelength is about $\lambda_x = 1250$ -1400 km.

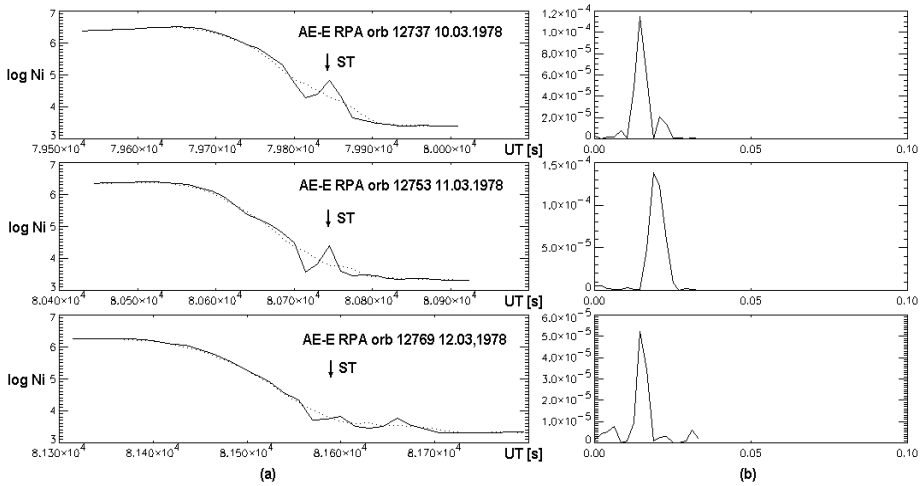

Fig.5. RPA Ni density profiles as taken from three equatorial passes through the terminator zone of AE-E during three subsequent days at height of ~320 km

3. Discussion

The theory of AGW in multi-component medium is the subject of [9, 10], where it is shown that the amplitude and phase of fluctuations for different sorts of gases are different. This effect has been observed experimentally on Atmosphere Explorer-C data and discussed in [11, 12]. Let us examine in details the generation mechanism of fluctuations in the air density of propagating AGW. AGW compression phase appears because of upwelling of the dense bottom layer of the atmosphere. In the same way, rarefied phase of AGW appears when low density air from upper levels moves downward in the atmosphere.

Let us consider that the motion of elementary air volume is slow enough, so the air pressure in the volume equalizes with the surrounding atmosphere. In this case, density changes could be written as follows:

$$(1) \qquad \delta\rho_s(t) = c_s^{-2}\delta p_s(t) = c_s^{-2}\delta\left(p_0 e^{-z(t)/H}\right) \approx -\frac{\delta z(t)}{\gamma \cdot H}\rho(z),$$

where c_s – sound velocity, $p(z) = p_0 e^{-z/H}$, $\rho(z) = \rho_0 e^{-z/H}$ – barometric distribution of atmospheric pressure and γ – adiabatic factor, $\delta z = \delta z(t)$ – vertical displacement of the air volume. Density variation at a given height is equal to the difference of upwelling volume $\rho_s(z) = \rho(z - \delta z) + \delta\rho_s$, and undisturbed air density $\rho(z)$:

$$(2) \qquad \delta\rho(t) = \rho_s(z) - \rho(z) = \delta\rho_s - \delta\left(\rho_0 e^{-z/H}\right) \approx \frac{\gamma - 1}{\gamma}\frac{\delta z(t)}{H}\rho,$$

which leads to

$$(3) \qquad \frac{\delta\rho(t)}{\rho} = \frac{\gamma - 1}{\gamma}\frac{\delta z(t)}{H}.$$

The latest expressions relate the relative AGW amplitude $A = \delta\rho/\rho$ with the amplitude of vertical displacement of the particles δz.

Repeating the procedure for the "α" sort of gases and taking in account that, after rarefaction or compression of the mixed gases, the density of the individual components changes in a proportional way $\delta\rho_{s\alpha}/\rho_{s\alpha} = \delta\rho_s/\rho_s$ and that, above turbo pause, different components follow individual vertical distribution corresponding to scale H_α, one can write:

$$(4) \qquad \frac{\delta\rho_\alpha}{\rho_\alpha} = \left(\frac{H}{H_\alpha} - \gamma^{-1}\right)\frac{\delta z}{H} = \frac{\gamma H/H_\alpha - 1}{\gamma - 1}\frac{\delta\rho}{\rho}.$$

Expressions (3), (4) are obtained under the following simplifying assumptions: (i) AGW propagation does not disturb hydrostatic distribution of atmospheric pressure $p(z) = p_0 e^{-z/H}$, $p(x, y) = const$, (ii) different atmospheric gases move in AGW in the same way. More strict estimations made in [9, 13] lead to negligible quantitative corrections in relations (7), (8) which could be neglected in our further treatment.

In AE-E observations at 250…300 km, the predominant atmospheric component is atomic oxygen (almost 90% of total density), where scale height of the multi component atmosphere $H \approx H_O \approx 50$ km, adiabatic

factor $\gamma = 5/3$ (single component gas). For the characteristic AGW amplitude of $A = \delta[O]/[O] \sim 0.02$, the amplitude of the vertical displacement of layers following (3) becomes $\delta z \sim 2$ km. The next atmospheric components, molecular nitrogen and helium, have density ratio $[O]:[N_2]:[He] = 100:10:1$ and scale height ratio $H_O : H_{N2} : H_{He} = 1:1.75:0.25$. From equation (4), the amplitudes of individual gas disturbances become

$$\frac{\delta[N_2]}{[N_2]} \approx 3\frac{\delta[O]}{[O]}, \quad \frac{\delta[He]}{[He]} \approx -\frac{\delta[O]}{[O]}, \tag{5}$$

which is in good agreement with AE-E observations. Note that helium density variations are opposite to the variations of background component.

On some orbits, AE-E provided measurements of neutral wind vertical component of the velocity V_z (see. Table 1). This allows us to calculate the period of observed AGW from experimental data. While $V_z = \delta\dot{z} = i\omega\delta z$, relation (3) represents frequency, relative AGW amplitude and vertical wind velocity:

$$\omega = \frac{\gamma - 1}{\gamma}\frac{V_{zm}}{H}A^{-1}, \tag{6}$$

where V_{zm} – is amplitude of velocity fluctuations. The calculated periods of AGW are about 50…55 min, which is well supported by theoretical estimations.

These estimations, concerning the various effects on neutral atmosphere from propagating AGW, also give us a key to understand plasma response to AGW. It has to be pointed out here that ion density disturbances in relative units usually prevail over neutral atmosphere response to AGW. This is demonstrated pretty well by the enhanced AGW amplitude in plasma density in the night time hemisphere where the amplitudes of TID reach up to ten percent.

As it is well known, at night time conditions, F-region plasma support originates from downward diffusion of O^+ ions from topside ionosphere [14]. Recombination processes of molecular nitrogen at altitudes of about 200…300 km lead to the formation of steep gradient in the vertical ion density profile $n_p(z)$. The dynamics of the F-region predominant O^+ ions is described by the continuity equation:

(7) $$\frac{\partial[O^+]}{\partial t}+\frac{\partial}{\partial z}\left(V_D\cdot[O^+]\right)=-a[N_2][O^+],$$

where V_D is vertical plasma drift velocity, a – ion-neutral recombination coefficient, term $\tau=(a[N_2])^{-1}$ – lifetime of O^+ ions. Assuming $\partial/\partial t=0$, one can evaluate the quasi-stationary vertical distribution of night time O^+ ion density:

(8) $$[O^+]=n_p(z)=n_{p0}\exp\{\frac{H_{N2}}{H_p}\left(1-e^{(z_0-z)/H_{N2}}\right)\},$$

where $H_p=(a[N_2])^{-1}|_{z=z0}\cdot V_D$ – drift length of O^+ ions for lifetime τ. Near F maximum vertical profile could be approximated by exponential function (9):

(9) $$n_p(z)\approx n_{p0}\exp\{\frac{z-z_0}{H_p}\},\ \text{while}\ |z-z_0|<H_{N2}.$$

Thus, drift length H_p plays the role of plasma distribution vertical scale (ionospheric scale height). If $z_0=300$ km, $V_D=10$ m/s, $\tau=(aN_2)^{-1}|_{z=z0}=10^3$ s, scale height becomes $H_p=10$ km.

The influence of AGW on plasma dynamics in the F-region is described by equation (7) where the following replacements can be made: $aN_2\to aN_2+\delta(aN_2)$ (changing recombination background under the influence of AGW) and $V_D\to V_D+\delta V_i$ (neutral particles effectively drug ions). Estimations show that, beneath h_mF2 altitude, especially in the steep ion density gradient zone [11], the latest term prevails. Because of the high ion-neutral collision frequency at these heights, ions move along the magnetic field lines with the speed of neutrals, and in parallel, ions drift perpendicularly, driven by perpendicular electric field [14, 15]. Thus, $\delta V_i\sim\delta V_n$, which coincides with *in situ* velocity measurements on AE-E. In this case, the estimation of plasma density variations leads to expression (4) with negative plasma scale height $H_\alpha=-H_p$ (while $z<h_mF2$ plasma density increases with altitude):

(10) $$\frac{\delta[O^+]}{[O^+]}\sim-\frac{\gamma H/H_p+1}{\gamma-1}\frac{\delta[O]}{[O]}.$$

In accordance with (10), ion density fluctuations occur in anti-phase with AGW with larger relative amplitudes. If we assume $H = 50$ km, $H_p = 10$ km, relative O^+ variations become

$$\left|\frac{\delta[O^+]}{[O^+]}\right| = 15 \cdot \left|\frac{\delta[O]}{[O]}\right|. \quad (11)$$

In contrast to the major O^+ ions, molecular NO^+ and O_2^+ ion motion caused by neutrals in the space/time scale of AGW is negligible. AGW propagation affects molecular ions only by reducing background recombination levels, because their photochemical lifetime at these altitudes is less than one minute. Relative variations of molecular ions do follow neutral density fluctuations (see Fig. 5.3) where:

$$\frac{\delta[NO^+]}{[NO^+]} \sim \frac{\delta[N_2]}{[N_2]}, \quad \frac{\delta[O_2^+]}{[O_2^+]} \sim \frac{\delta[O_2]}{[O_2]}. \quad (12)$$

Conclusions

In the present paper, wavelike processes at the terminator are studied for the first time by means of *in situ* satellite observations. Atmosphere Explorer-E satellite provided both neutral and charged particle measurements in the Earth's atmosphere, which permits *in situ* study of AGW and TID, their interactions with background atmospheric species. For the period of the data used here, AE-E measurements cover equatorial ionosphere at altitude 250…300 km, beneath F-region maximum.

As shown by experimental data, in the morning hours after sunrise (6…11^h local time) and evening hours after sunset (19…24^h), intensification of the wavelike activity in the various atmosphere components is observed, evidencing of large scale generation of AGW/TID by moving terminator. The main persistent characteristics of these fluctuations could be summarized as follows:

- Horizontal wavelength 1400…1600 km;
- Estimated period 50…55 min;
- AGW/TID train of 4…6 wave periods;
- Relative AGW amplitudes of few percents;
- Relative morning TID amplitudes of few percents, and evening TID amplitudes greater than ten percents;
- Relative ion density variations prevail over the corresponding neutral density fluctuations. At night $[O^+]$ density behaviour is in

anti-correlation with the variations in the main neutral components such as $[N_2]$, [O].

– Variations in $[NO^+]$ and $[O_2^+]$ molecular ions do follow neutral atmosphere fluctuations.

The amplitude and phase relationships between the different atmospheric components presented in this paper do correspond to the main behaviour of AGW above turbopause. Note that the changes in volume density in the presence of AGW correspond to the upward motion of dense air layers and downward motion of rarefied layers from the top. The dimensionless parameter referred to density variation of gas component $\delta\rho_\alpha$ corresponds to the ratio of vertical displacement of layer to the scale height of the given component $\delta z / H_\alpha$. The heavier is the gas component (i.e. as small is H_α), the higher is the relative density variation. Below ionospheric maximum $z < h_m F2$ plasma density increases with height which leads to negative scale heights at these altitudes. As a result, plasma and neutral density have opposite variations and plasma variations are larger than relative amplitudes in AGW.

Ionospheric plasma response to AGW propagation discussed here is of great importance, because ground-based and space-borne AGW measurements concern mostly the registration of plasma effects of AGW instead of neutral ones.

References

1. Beer T. Supersonic generation of atmospheric waves //Nature. – 1973. – V.242, N5392. – P.34.
2. Galushko V. G., V. V. Paznukhov, Y. M. Yampolski and J. C. Foster. Incoherent Scatter Radar Observations of the AGW/TID Events Generated by the Moving Solar Terminator // Ann. Geophys. –1998. – Vol.16. – p. 821-827.
3. Бурмака В. П., В. И. Таран, Л. Ф. Черногор. Результаты исследования волновых возмущений в ионосфере методом некогерентного рассеяния //Успехи современной радиоэлектроники. – 2005. – №3. – С.4-35.
4. Dalgarno A., W. B. Hanson, N. W. Spencer and E. R. Schmerling. The Atmosphere Explorer mission // Radio. Sci. – 1973. –V. 8. –P. 263-273.
5. Сомсиков В. М. Солнечный терминатор и динамика атмосферы. – Алма-Ата: Наука, 1983. – 192 с.
6. Сомсиков В. М. Волны в атмосфере, вызванные движением солнечного терминатора (обзор) //Геомагнетизм и аэрономия.– 1991. – Т.31, № 1, с.1-12.

7. G e o r g e s T. M. HF Doppler studies of travelling ionospheric disturbances // Journal of Atmospheric and Terrestrial Physics. – V. 30. – P. 735-746.
8. F r a n c i s S. H. Global propagation of atmospheric gravity waves: a review// Journal of Atmospheric and Terrestrial Physics. –1975. – V. 37. – P. 1011-1054.
9. D e l G e n i o A. D., G. S c h u b e r t, J. M. S t r a u s. Gravity wave propagation in a diffusively separated atmosphere with height-dependent collision frequencies// J. Geophys. Res. –1979 – V.84,NA8 – P.4371-4378.
10. I n n i s J. L and M. C o n d e. Characterization of acoustic-gravity waves in the upper thermosphere using Dynamics Explorer 2 Wind and Temperature Spectrometer (WATS) and Neutral Atmosphere Composition Spectrometer (NACS) date // J. Geophys. Res. –2002. – Vol.107, № A12. – SIA 1-21.
11. R e b e r C. A., A. E. H e d i n, D. T. P e l z, W. E. P o t t e r and L. H. B r a c e. Phase and amplitude relationships of wave structure observed in the lower thermosphere // J. Geophys. Res. –1975. –V.80. –P. 4576-1975.
12. P o t t e r W. E., D. C. K a y s e r and K. M a u e r s b e r g e r. Direct measurements of neutral wave characteristics in the thermosphere //J. Geophys. Res. – 1976. – V.81. – P.5002.
13. M a k h l o u f U., E. D e w a n, J. R. I s l e r and T. F. T u a n. On the importance of the purely gravitationally induced density, pressure and temperature variations in gravity waves: Their application to airglow observations //J. Geophys. Res. – 1990. – V.95. – P. 4103-4111.
14. Б р ю н е л л и Б. Е., А. А. Н а м г а л а д з е. Физика ионосферы. – М.: Наука, 1988. – 527 с.
15. K e l l e y M. C. The Earth's Ionosphere Plasma Physics and Electrodynamics // Academic Press. Inc. International Geophysics Series –1989. –V.43. – 487 p.

ГРАВИТАЦИОННИ ВЪЛНИ В АТМОСФЕРАТА, СВЪРЗАНИ С ДВИЖЕНИЕТО НА СЛЪНЧЕВИЯ ТЕРМИНАТОР ПРЕЗ ВИСОКАТА АТМОСФЕРА НА ЗЕМЯТА

Г. Лизунов, А. Федоренко, Л. Банков, А. Василева

Резюме

Чрез използването на данни от непосредствени (in situ) измервания на спътника Atmosphere Explorer - E са изследвани ефектите от движението на слънчевия терминатор във високата атмосфера. Анализирани са данните от приборите RPA (Retarding Potential Analyzer) и NACE (Neutral Atmospheric Composition Experiment) за периода на кръгова екваториална орбита на спътника с инклинация $i = 19.7°$ и

височина 250-300 km. Показано е, че при движението си през неутралната атмосфера, слънчевият терминатор генерира крупномащабни атмосферни гравитационни вълни (АГВ) и движещи се йоносферни смущения (ДИС) със следните параметри: 1) хоризонтална дължина на вълната около 1200-1600 km; 2) период около 50 минути; 3) характерен хоризонтален размер на вълновия пакет АГВ/ДИС от четири до шест вълни; 4) относителната амплитуда на АГВ е от порядъка на няколко проценти от концентрацията; 5) относителната амплитуда на ДИС около изгревния терминатор е от порядъка на няколко процента, докато за вечерния терминатор надминава десет процента; 6) вариациите в концентрацията на $[O^+]$ са в противофаза с вариациите в преобладаващите неутрални компоненти $[N_2]$, [O]; 7) молекулярните йони $[NO^+]$ и $[O_2^+]$ осцилират във фаза с неутралите. Получените експериментални резултати са интерпретирани в светлината на теорията на разпространение на АГВ в мултикомпонентна среда. Показано е, че особеностите в разпределението на амплитудите и фазите за осцилациите на неутралните и заредените компоненти в атмосферата се дължат на разликите във вертикалното им разпределение над турбопаузата.

Bulgarian Academy of Sciences. Space Research Institute.
Aerospace Research in Bulgaria. 23, 2009, Sofia

PHENOMENOLOGICAL QUARK-LEPTON MASS RELATIONS AND NEUTRINO MASS ESTIMATIONS

Dimitar Valev

Stara Zagora Department, Institute of Solar Terrestrial Influences – Bulgarian Academy of Sciences
e-mail: valev@gbg.bg

Abstract

Based on experimental data and estimations of the charged leptons and quark masses, a close power law with exponent ¾ has been found, connecting charged lepton masses and up quark masses. A similar mass relation has been suggested for the masses of neutral leptons and down quarks. The latter mass relation and the results of the solar and atmospheric neutrino experiments have been used for prediction of neutrino masses. The obtained masses of ν_e, ν_μ and ν_τ are 0.0003 eV, 0.003 eV and 0.04 eV, respectively. These values are compatible with the recent experimental data and support the normal hierarchy of neutrino masses.

Key words: *mass relation; quark-lepton symmetry; neutrino mass; normal hierarchy.*

1. Introduction

Decades after the experimental detection of the neutrino [1], it was generally accepted that the neutrino mass $m_{o\nu}$ was rigorously zero. The crucial experiments with the 50 kton neutrino detector Super-Kamiokande found strong evidence for oscillations (and hence - mass) in atmospheric neutrinos [2]. The direct neutrino measurements allowed to find neutrino mass. The upper limit for the mass of the lightest neutrino flavor ν_e was obtained from experiments for measurement of the high-energy part of the tritium β-spectrum and recent experiments yielded ~ 2 eV upper limit [3, 4]. As a result of the recent experiments, the upper mass limits of ν_μ and ν_τ

are 170 *keV* [5] and 18.2 *MeV* [6], respectively. The Solar neutrino experiments (*SNE*) and Atmospheric neutrino experiments (*ANE*) allow to find the square mass difference $\Delta m_{12}^2 = m_2^2 - m_1^2$ and $\Delta m_{23}^2 = m_3^2 - m_2^3$, but not the absolute value of neutrino masses. The astrophysical constraint of the neutrino mass is $\Sigma m_\nu < 2\ eV$ [7]. The recent extensions of the Standard model lead to non-zero neutrino masses, which are within the wide range of $10^{-6}\ eV \div 10\ eV$.

In the classical *SU(5)* model, the mass relations between charged leptons and down quark masses are simple identities: $m_e = m_d$, $m_\mu = m_s$ and $m_\tau = m_b$. The mass relations of Georgi-Jarlskog [8] ensue from the *SO(10)* model and relate charged leptons and down quark masses: $m_e = m_d / 3$, $m_\mu = 3m_s$ and $m_\tau = m_b$. However, these mass relations deviate several times, compared to experimental data. Moreover, similar mass relations are unsuited for neutral leptons (neutrino) masses.

The seesaw mechanism naturally generates small Majorana neutrino mass m_ν from reasonable Dirac mass m_D and very heavy Majorana sterile neutrino mass M_N, namely $m_\nu \sim \frac{m_D^2}{M_N} << m_D$. But there are many seesaw models that differ in the scale M_N and Dirac mass. The Grand unified theories (*GUT*) are the main candidates for seesaw models, with M_N at or a few orders of magnitude below the *GUT* scale. Successful *GUT* models should essentially generate Cabibbo-Kobayashi-Maskawa (*CKM*) quark mixing matrix [9, 10] and Maki-Nakagawa-Sakata (*MNS*) lepton mixing matrix [11] and predict results compatible with the data from *SNE* and *ANE*. Yet, it is admitted that the predictions of the quark-lepton mass spectrum are the least successful aspect of the unified gauge theory [12, 13].

The purpose of this paper is to find simple and reliable quark-lepton mass relations, based on experimental data and estimations for quark and lepton masses. The next step is to estimate neutrino masses by means of these mass relations and data from *SNE* and *ANE*.

2. Power law approximation for the masses of charged leptons and up quarks

According to the Standard model, the fundamental constituents of matter are 6 quarks and 6 leptons. The fundamental fermions group in three generations having similar properties and increasing masses. The three

generations of the fundamental fermions and their masses are presented on Table 1. The estimations of quark masses are taken from [14] and the upper mass limits of neutrino flavors are taken from [3-6].

Table 1. Three generations of fundamental fermions and their masses (MeV)

Fermions	First generation		Second generation		Third generation	
Up quarks	u	3	c	1.25×10^{3}	t	1.74×10^{5}
Down quarks	d	6	s	122	b	4.2×10^{3}
Charged leptons	e	0.511	μ	106	τ	1.78×10^{3}
Neutral leptons	ν_e	$<2\times10^{-6}$	ν_μ	< 0.17	ν_τ	< 18.2

A clear feature of the quark and charged lepton mass spectrum is the hierarchy of masses belonging to different generations:

(1) $$m_u << m_c << m_t\,,\; m_d << m_s << m_b\,,\; m_e << m_\mu << m_\tau$$

Most likely, a similar hierarchy of the masses of neutral leptons (neutrinos) could be anticipated $m_{\nu e} << m_{\nu\mu} << m_{\nu\tau}$. Based on experimental data, we search for a simple relation between the masses of charged leptons (m_{cl}) and the respective up quarks (m_{uq}) by the least squares. Although the linear regression $m_{cl} \approx 0.0102\, m_{uq}$ eV shows close correlation, it yields electron mass many times lower than the experimental value. After examination of other simple approximations (logarithmic, exponential and power law), we found out that the power law fits best experimental data:

(2) $$m_{cl} = k_0 m_{uq}^{\alpha} \;\; eV$$

where $k_0 = 9.33$ and $\alpha = 0.749 \approx ¾$.

Despite the great uncertainty of u-quark mass (from 1.5 *MeV* to 5 *MeV*) and d-quark mass (from 3 *MeV* to 9 *MeV*), the slope remains within the narrow interval from 0.683 to 0.782. Although only three points make the approximation, the correlation coefficient is very high (r = 0.993) and the maximal ratio of the predicted mass in relation to the respective experimental value $\Delta = m_{pr} / m_{ex}$ is 1.74 (for muon). The predicted masses

of the electron and tau lepton differ from the respective experimental values by less than 40%. Therefore, mass relation (2) could be accepted as satisfactory.

3. Mass relation for neutral leptons and down quarks and estimations of neutrino masses

We suggest that a mass relation similar to (2) connects the masses of neutral leptons (m_{nl}) and the respective down quarks (m_{dq}):

(3) $$m_{nl} = k m_{dq}^{\alpha} \ \ eV$$

where $\alpha = 0.749 \approx ¾$ and k is an unknown constant.

For $k = k_0 = 9.33$, formula (3) yields $m_{\nu e} \approx 1.13\ MeV$, $m_{\nu\mu} \approx 10.84$ *MeV* and $m_{\nu\tau} \approx 153.66\ MeV$. These values are several orders of magnitude bigger than the experimental upper limits of neutrino masses (See Table 1), therefore $k << k_0$. Astrophysical constraints allow to limit more closely the value of k, since they give $m_{\nu} < \Sigma m_{\nu} < 2\ eV$. Thus, from equation (3) we obtain:

(4) $$k = \frac{m_{\nu\tau}}{m_b^{3/4}} < \frac{\Sigma m_{\nu}}{m_b^{3/4}} \sim 1.21 \times 10^{-7}$$

ANE [15] determines the squared mass difference:

(5) $$m_{\nu\tau}^2 - m_{\nu\mu}^2 \approx 2.2 \times 10^{-3} eV^2$$

Relation (3) yields:

(6) $$\frac{m_{\nu\mu}}{m_{\nu e}} \sim \left(\frac{m_s}{m_d} \right)^{3/4} \approx 9.60$$

(7) $$\frac{m_{\nu\tau}}{m_{\nu\mu}} \sim \left(\frac{m_b}{m_s} \right)^{3/4} \approx 14.17$$

Solving system (5)–(7), we obtain $m_{\nu e} \approx 3.4 \times 10^{-4}\ eV$, $m_{\nu\mu} \approx 3.3 \times 10^{-3}\ eV$ and $m_{\nu\tau} \approx 4.7 \times 10^{-2}\ eV$. These results support the normal hierarchy of neutrino masses.

On the other hand, the Large mixing angle (*LMA*) of Mikheyev-Smirnov-Wolfenstein (*MSW*) solution for *SNE* yields [16]:

(8) $m_{\nu\mu}^2 - m_{\nu e}^2 \approx 7.9\times10^{-5} eV^2$

This equation, together (6) and (7), yield $m_{\nu e} \approx 9.3\times10^{-4}$ *eV*, $m_{\nu\mu} \approx 8.9\times10^{-3}$ *eV* and $m_{\nu\tau} \approx 0.13$ *eV*. These values are almost three times bigger than the values obtained by Super Kamiokande data, therefore, they do not fit well with the latter. However, the Small mixing angle (*SMA*) *MSW* solution for *SNE* [17] yields:

(9) $m_{\nu\mu}^2 - m_{\nu e}^2 \approx 6\times10^{-6} eV^2$

This equation, together (6) and (7), yield $m_{\nu e} \approx 2.6\times10^{-4}$ *eV*, $m_{\nu\mu} \approx 2.5\times10^{-3}$ *eV* and $m_{\nu\tau} \approx 3.4\times10^{-2}$ *eV*. These values differ by less than 25% from the results obtained by Super Kamiokande data, which show that according to the suggested approach, *SMA MSW* solution fits better with the *ANE* than *LMA MSW*.

Thus, the obtained quark-lepton mass relations and the results of the solar and atmospheric neutrino experiments provide to estimate the masses of ν_e, ν_μ and ν_τ of $(2.6\div3.4)\times10^{-4}$ *eV* $(2.5\div3.3)\times10^{-3}$ *eV* and $(3.4\div4.7)\times10^{-2}$ *eV*, respectively. These values are close to the neutrino masses (2.1×10^{-4} *eV*, 2.5×10^{-3} *eV* and 5.0×10^{-2} *eV*) found in [18] by the mass relation connecting the masses of four stable particles and the coupling constants of the fundamental interactions.

We could calculate constant *k* using the most trustworthy data for neutrinos and down quark masses, namely ν_τ and b-quark masses:

(10) $k = \dfrac{m_{\nu\tau}}{m_b^{3/4}} \sim 2.42\times10^{-9}$

The obtained mass relations (2) and (3) are shown in Fig. 1. It shows that the neutrino masses estimated by *SMA MSW* are close to the neutrino masses estimated by *ANE*, i.e. two sets of estimations are compatible.

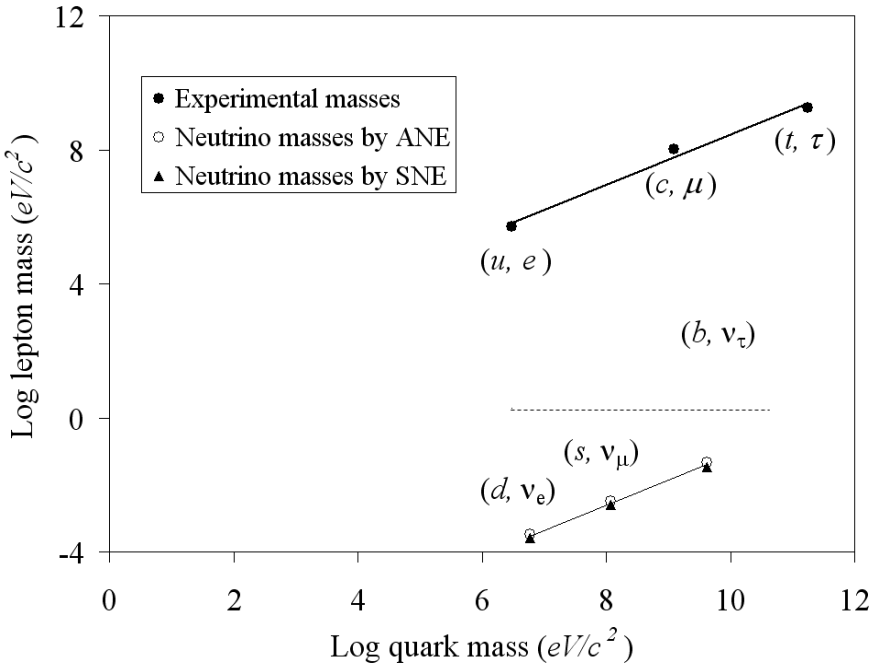

Fig. 1. Mass relations for charged leptons and up quark masses (thick solid line) and for neutral leptons and down quark masses (thin solid line). The dashed line shows the upper limit of the neutrino masses obtained by astrophysical constraints

The attempt to relate the masses of charged leptons with the masses of down quarks and the masses of neutral leptons with the masses of up quarks did not yield satisfactory results, since the data from *SNE* and *ANE* did not fit within the framework of the suggested approach. Besides, the respective mass relations predict a muon mass which is nearly three times less than the experimental value (see Table 2) and an electron neutrino mass which is less than 10^{-7} *eV*.

Table 2 shows the masses of charged leptons calculated by different approaches and experimental values. The last row of the table shows the maximal ratio (deviation) of the masses predicted by the respective approach in relation to the experimental values $\Delta = m_{pr} / m_{ex}$. Clearly, the power law relating to the masses of charged leptons and up quarks fits best experimental data.

Table 2. Masses of charged leptons calculated by various approaches and experimental values (MeV)

Model	*SU(5)*	*SO(10)*	Linear (Down quarks)	Power law (Down quarks)	Linear (Up quarks)	Power law (Up quarks)	Exp. data
Electron	6	2	2.545	0.905	0.031	**0.663**	**0.511**
Muon	122	366	51.8	36.9	12.8	**60.7**	**105.7**
Tau	4200	4200	1782	2877	1775	**2449**	**1777**
Maximal deviation	11.74	3.91	4.98	2.86	16.48	**1.74**	**1**

4. Conclusions

Based on experimental data and estimations of charged leptons and quark masses, a power law with exponent ¾ has been found, connecting charged lepton masses and up quark masses. It has been shown that this approximation is considerably better than any known approach. A similar mass relation has been suggested for neutral leptons and down quarks. The latter mass relation and the results of *ANE* and *SNE* have been used for estimations of neutrino masses. The values of neutrino masses obtained by *ANE* are close to the ones obtained by the *SMA MSW* solution. The masses of ν_e, ν_μ and ν_τ are estimated to $(2.6\div3.4)\times10^{-4}$ *eV*, $(2.5\div3.3)\times10^{-3}$ *eV* and $(3.4\div4.7)\times10^{-2}$ *eV*, respectively, and they support the normal hierarchy of neutrino masses.

References

1. Reines F., C. L. Cowan. Detection of the free neutrino, Phys. Rev., 92, 1953, 830-831.
2. Fukuda Y. et al. Evidence for oscillation of atmospheric neutrinos, Phys. Rev. Lett., 81, 1998, 1562-1567.
3. Weinheimer C. et al. High precision measurement of the tritium beta spectrum near its endpoint and upper limit on the neutrino mass, Phys. Lett. B, 460, 1999, 219-226.
4. Lobashev V. M. et al. Direct search for mass of neutrino and anomaly in the tritium beta-spectrum, Phys. Lett. B, 460, 1999, 227-235.
5. Assamagan K. et al., Upper limit of the muon-neutrino mass and charged-pion mass from momentum analysis of a surface muon beam, Phys. Rev. D, 53, 1996, 6065-6077.
6. Barate R. et al. An upper limit on the tau neutrino mass from three- and five-prong tau decays, Eur. Phys. J. C, 2, 1998, 395-406.

7. B a h c a l l J. N. Solar neutrinos: Where we are, where we are going. Astrophys. J., 467, 1996, 475-484.
8. G e o r g i H., C. J a r l s k o g. A new lepton-quark mass relation in a unified theory, Phys. Lett. B, 86, 1979, 297-300.
9. Cabibbo N., Unitary symmetry and leptonic decays, Phys. Rev. Lett., 10, 1963, 531-533.
10. Kobayashi M., T. Maskawa, CP-violation in the renormalizable theory of weak interaction, Prog. Theor. Phys., 49, 1973, 652-657.
11. M a k i Z., M. N a k a g a w a, S. S a k a t a. Remarks on the unified model of Elementary Particles, Prog. Theor. Phys., 28, 1962, 870-880.
12. F u k u g i t a M., M. T a n i m o t o, T. Y a n a g i d a. Embedding phenomenological quark-lepton mass matrices into SU(5) gauge models, Phys. Rev. D, 59, 1999, 113016-113019.
13. F a l c o n e D. Fermion masses and mixings in gauge theories, Int. J. Mod. Phys. A, 17, 2002, 3981-4006.
14. M a n o h a r A. Quark masses, Eur. Phys. J. C, 15, 2000, 377-385.
15. A s h i e Y. et al. Measurement of atmospheric neutrino oscillation parameters by Super-Kamiokande I, Phys. Rev. D, 71, 2005, 112005-112040.
16. B a n d y o p a d h y a y A. et al. Update of the solar neutrino oscillation analysis with the 766 Ty KamLAND spectrum, Phys. Lett. B, 608, 2005, 115-129.
17. A l b r i g h t C. H. Overview of grand unified models and their predictions for neutrino oscillations, Nucl. Instr. Meth. Phys. Res. A, 472, 2001, 359-363.
18. V a l e v D. Neutrino and graviton mass estimations by a phenomeno-logical approach, Aerospace Res. Bulg., 22, 2008, 68-82 [arxiv:hep-ph/0507255]

ФЕНОМЕНОЛОГИЧНИ КВАРК-ЛЕПТОННИ МАСОВИ ВРЪЗКИ И ОЦЕНКИ НА МАСИТЕ НА НЕУТРИНОТО

Д. Вълев

Резюме

На базата на експерименталните данни и оценки за масите на заредените лептони и кварките бе намерен степенен закон с показател ¾, свързващ масите на заредените лептони и up-кварките. Подобна масова връзка бе предложена за масите на неутралните лептони и down-кварките. Последната масова връзка и резултатите от слънчевите и атмосферните неутринни експерименти бяха използувани за предсказване на масите на неутриното. Получените маси на ν_e, ν_μ и ν_τ са 0.0003 *eV*, 0.003 *eV* и 0.04 *eV*, съответно. Тези стойности са съвместими със съвременните експериментални данни и подкрепят нормалната йерархия на масите на неутриното.

Bulgarian Academy of Sciences. Space Research Institute.
Aerospace Research in Bulgaria. 23, 2009, Sofia

AEROSPACE TEST SITES IN BULGARIA – STATE AND PROSPECTS

Eugenia Roumenina, Vanya Naydenova, Georgi Jelev, Vassil Vassilev, Lubomira Kraleva

Space Research Institute – Bulgarian Academy of Sciences
e-mail: roumenina@space.bas.bg

Abstract

During the last decades, great attention has been paid to integrated use of ground-based (in situ) and remote sensing data. Practice shows that the trustworthiness and accuracy of the information derived from aerial photos and satellite images depend strongly on the available relevant ground-based (in situ) data, which have great practical importance both during the interpretation of remote sensing data, as well as during the modelling and forecasting of natural and technogenic processes. Therefore, the GEOSS and GMES systems that are now under construction pay great attention to this component. The accumulated international experience in the field of remote sensing of the Earth proves that the most rational way to obtain in situ data is the development of a network of aerospace (subsatellite) test sites, representative of the different climatic areas and featuring diverse vegetation cover, thematic and functional purpose depending on the tasks of test site service. Bulgarian Aerospace Test Sites (BASTSs) pertain to the test type by their functional intention. The first Bulgarian test sites were established in the beginning of the 70-ies of the last century and nowadays their number has reached 7. Many satellite images and aerial photos, spectrometric, radiometric, and ground-based data, which have been acquired for these BASTSs, have been uploaded in the thematically distributed satellite and sub-satellite database of the BASTS Scientific-Information Complex (SIC). A web-based BASTS information system, which is planned to be created in the forthcoming years, will provide an effective solution for integration, access, analysis, and publication of obtained information and data on the web-site.

Keywords: *Web-Based Information Systems, Remote Sensing Methods, Aerospace Test Sites, Sub-Satellite Experiments, Geoinformation Technologies*

Introduction

The modern stage of monitoring the development of ecological systems, forecasting natural and anthropogenic disasters and averages, and concrete decision-taking for their prevention are characterized by the global nature of the set tasks and the active use of data from various sources, whereby great attention is paid to satellite images. A number of international programmes are targeted at resolving these international problems, aiming to integrate regional and national monitoring systems. Earth observation is an improved technology which through the use of space and ground-based equipment provides great opportunities for monitoring environment and environmental security threats by obtaining timely, reliable, and objective information. Since 2005, the international scientific community has started implementing the 10-year programme *The Global Earth Observation System of Systems* (GEOSS). It is coordinated by the Group on Earth Observation (GEO). The major goal of this programme is to substantially complete and particularize at quantitative level our knowledge on Earth geosphere status [1, 2]. The major European contribution to the implementation plan of the GEOSS is the Global Monitoring for Environment and Security (GMES) Project which will provide service of public interest. It has three components: Space segment, *in situ* component, and Services. Their complex use will provide to offer new information services in many areas – precise land use mapping, fast mapping under critical circumstances for the purposes of civil protection or monitoring forests, wild fires, geological threat, atmospheric air etc.

The Global Monitoring for Environment and Security System will provide grounds for the establishment of structures collecting measurements and facilitating their use by a great number of users [3]. The timely and economically efficient information provision depends largely on the successful implementation of Directive 2007/2/EC of the European Parliament and of the Council of 14 March 2007 establishing an Infrastructure for Spatial Information in the European Community (INSPIRE), which envisages the establishment and exchange of data regarding the application of EU policies, especially in the field of environment preservation [4].

Remote sensing of the Earth's surface from space-based platforms has passed from the stage of scientific research to the stage of wide practical use and development of remote sensing of the Earth (RSE) technology.

Practice shows that the trustworthiness and accuracy of the information derived from aerial photos and space images depend strongly on the available corresponding ground-based (in situ) data. This data obtained by the use of physical (geochemical, phyto-indicative etc.) and spatial measurements or by the use of immediate object observations and studies help to increase the accuracy and relevance of remote sensing data. Therefore, ground-based data are used for control (calibration) during the formation, processing, and interpretation of aero- and space images. Moreover that, as a result of the still somewhat restricted potentials of modern RSE technologies, not all Earth geosphere and status parameters may be measured or observed by them. Therefore, the GEOSS and GMES systems that are now under construction pay great attention to receiving appropriate amounts of *in situ* data, which have great practical importance both during the interpretation of remote sensing data, as well as during the modelling and forecasting of natural and technogenic processes.

The accumulated international experience in the field of the remote sensing of the Earth proves that the most rational way to obtain *in situ* data is the development of a network of aerospace (subsatellite) test sites, characterizing the conditions of various climatic areas and diverse vegetation cover, and featuring characteristic thematic purpose and functional purpose, corresponding to the tasks of test site service. The network of aerospace test sites is an important segment of space research ground-based infrastructure which is envisaged to provide information for the GMES. Such test sites have been established in the USA, Canada, Russia, France, Germany, Spain and other countries.

Aerospace test sites on the territory of Bulgaria

Depending on their function, aerospace test sites can be divided into control and calibration test sites. The control and calibration test sites are used to solve tasks related with the post-start adjustment of the on-board systems' parameters for the purpose of achieving optimal image acquisition mode during the process of the Earth's surface aerospace monitoring and determining the accurate values of the external orientation elements. By their functional intention, the Bulgarian Aerospace Test Sites (BASTSs) pertain to the second, test type. The major problems resolved by such test sites are related with development and certification of various methods for processing, analysis, and interpretation of data acquired by remote sensing of the Earth, development and completion of objects' spectral signature

databases, and conduct of scientific research. For these purposes, individual test sections are chosen on the test sites' territory, each of them having definite (spectral-brightness, geometric etc.) stable characteristics. These characteristics are used during the images' interpretation as reference indicators for the relevant object class. Furthermore, the quantitative values of these characteristics provide for radiometric (brightness) and geometric corrections to be made.

In the beginning of the 70-ies of the last century, on the territory of the *Intercosmos* Programme member-states, a network of aerospace test sites was established, in which multiple international quasi-synchrounous sub-satellite experiments were carried out (Koursk, Gobi-Hangay, Caribe, Telegeo, Tyan-Shan etc.). In 1973, at a technical meeting of representatives of Russian and Bulgarian geodetic offices held under the *Intercosmos* Programme, 5 test sites were appointed (Fig. 1): Pleven, Shoumen, Rila, Plovdiv, and East Rhodopes, [5,6,7,]. Their organization on the Bulgarian side was assigned to the Central Laboratory for Space Research, currently Space Research Institute (SRI) at the Bulgarian Academy of Sciences (BAS). Later, they were supplemented by 2 more – Pchelina Dam and Novi Iskur. The *Pchelina Dam* test site included in 1987 in relation with the implementation of the *Home Water Catchments* Project under the *Intercosmos* Programme. The *Novi Iskur* test site is a new one, established in 2005 with the financial support of the *Scientific Research* Fund at the Ministry of Education and Science (Contract No.1507).

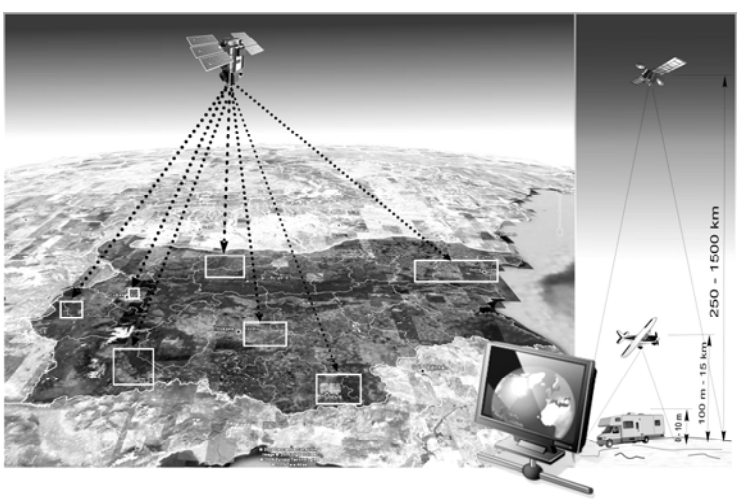

Fig. 1. Aerospace Test Sites in Bulgaria

On its territory, studies aiming to improve the methods of landscape-ecological planning using remote sensing are carried out. During these experiments, many images, spectrometric, radiometric, and ground-based data were accumulated, which were uploaded in the thematically distributed satellite and sub-satellite database of the scientific-information complex (SIC) of the (BASTSs). It was established during the period from 16.10.2007 to 16.04.2009 as a result of the joint efforts of scientists from 2 institutes of the BAS, SRI and National Institute of Meteorology and Hydrology (NIHM) (Contract NIK 003/2007 concluded between the SRI-BAS and the Science Research Fund at the Ministry of Education and Science of the Rep. of Bulgaria, with 25% co-financing by the SRI-BAS) [8,9].

During the last four years, at the Ministry of Emergency Situations of the Rep. of Bulgaria, the establishment of a natural disasters space monitoring system is underway, having satellite data as its main information source. The Aerospace Monitoring Centre was established with the financial support of the EU PHARE Programme. However, the structure of its information system does not envisage receiving any *in situ* data.

The BASTSs' information database maybe composed by integrated use of geoinformation system technologies, data processing systems, remote sensing of the Earth methods, and landscape ecology methods is envisaged.

The test sites in North Bulgaria are intended for remote sensing, mainly in the field of agriculture, prospecting of ores and minerals, such as oil-gas depositions and monitoring the anthropogenic changes of the environment. The polygons in South Bulgaria are oriented to development of ore prospecting methods, study of seismo-tectonic phenomena, exploration of a number of neotectonic morphostructures and faults.

Geodatabases for the *Plovdiv*, *Rila*, *East Rhodopes* and *Novi Iskur* test sites have been composed.

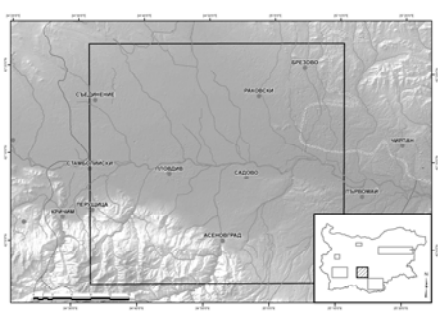

Plovdiv aerospace test site

On the *Plovdiv* test site, a number of methodical issues were clarified, related with recognition and mapping of various soil types and soil salination, mapping of land cover dynamics using aerial photos and satellite images [10]. The *Plovdiv* test

site is located in the Upper Thracean lowlands. For the conductance of sub-satellite experiments on the territory of the test site, two test areas are allocated including the land of Bolyarino and Belozem villages.

They are chosen because they have maximal land cover diversity, typical for the studied region of the Thracian lowland; area, meeting the requirements for spatial resolution of the satellite images. The geodatabase for the *Plovdiv* aerospace test site is composed on the base of topographic maps in scale 1:50,000 and 1:10,000 for the key areas and it consists of 31 layers. Six of them contain information about geology, geologic hazard and soil differences; 5 – about the settlements and road network; 5 – about the hydrographic network; 3 – about the relief; 3 – about the phonological development of 3 of the main crops, cultivated in this area (winter wheat, corn and rice); 5 – about the land use and man-induced transformation state and change; 3 – about the test area Bolyarino, containing spectrometric and radiometric data from the conducted synchronous airplane, ground-based and laboratory measurements, vegetation calendars, and data from the local agronomists and terrain studies. It also contains panchromatic and multispectral images – aerial photos, acquired by the cameras MRB, MKF-6 MC etc., and satellite images from Landsat TM, Landsat ETM^{+} and ASTER.

East Rhodopes aerospace test site

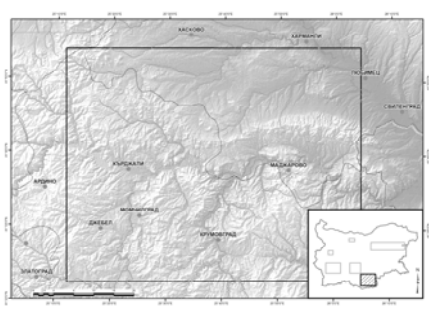

The *East Rhodopes* aerospace test site is located in the east part of the Rhodopes massif. The composing of the geodatabase is focused on geologic, geomorphologic studies and geologic hazard. It includes series of vector and raster layers – relief, river network, water bodies, road network, settlements, geology, deposits of ores and mineral resources, fault structures, geomorphologic structures, lineaments, geologic hazard, land cover, panchromatic and multispectral images [11]. The aerial photos are acquired by the cameras MRB, MKF-6 MC and etc., and the satellite images are from Landsat TM, Landsat ETM+ and ASTER. The composed geodatabase for the East Rhodopes comprises the time period from 1977 till 2008. It is used

for interpretation of the geomorphologic volcanogenic structures in the area and for studying the geologic hazard [12,13,14].

Rila aerospace test site

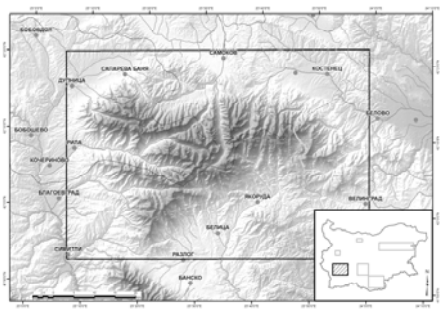

For the territory of the *Rila* aerospace test site and the chosen two test areas spatial data bases in vector format as well as raster ones are developed, containing various aerial photos and satellite images. Aerial photos for 4 years: 1966, 1977, 1988 and 1997, for the test area are processed. The forest vegetation for each period was interpreted and mapped and spatial analysis of the temporal changes was made [15]. An orthophoto mosaic of aerial photos was created for the area of Northern Rila with spatial resolution of 1 m [16, 17].

Novi Iskur aerospace test site

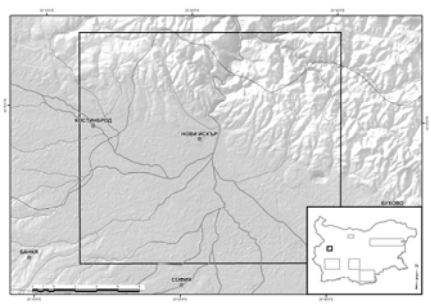

The newest aerospace test site, the *Novi Iskur* one, is located in the northwest part of the Metropolitan Municipality. For the territory of the *Novi Iskur* District, a geodatabase was composed, including satellite images and aerial photos for various temporal stages, digital elevation model and its derivatives, as well as vector information for relief, administrative boundaries, land cover and land use, soils, hydrographic network, transport infrastructure etc. Two test areas for the study area were defined for which more detailed geodatabases were composed – the first is the drainage basin of Kutinska River, where *Kutina Pyramids* natural landmark is located and the second one is the land of the Novi Iskur Town. The composed geodatabase for the Kutina drainage basin covers the period from 1940 till 2008 and its aim is to store, manage, visualize, give an opportunity for analysis, creation of models, and select objects by attributes. The designed geodatabase is of file type and it has

been created using the ESRI software product – ArcGIS 9.2 with license ArcINFO. It consists of 7 feature datasets with 21 feature classes, including information about watersheds, soils, hydrographic network, land cover, forest and soils, geomorphology and geology; 1 raster catalog with 385 images from MODIS; 19 raster datasets (topographic maps, archive aerial photos and satellite images from IKONOS, QuickBird, SPOT, ASTER and LANDSAT for various years), 14 tables with forest and climate data, 3 standalone feature classes with information about the location of Rain-Gauging Stations, boundary of the natural landmark and terrain data; and the corresponding topological and relationship classes [18,19]. The composed geodatabase for the Novi Iskur Town includes topographic maps and satellite images with medium and high resolution - IKONOS, QuickBird, SPOT, ASTER and LANDSAT for various years, DTM, vector information for soil, land cover, land use, buildings and road infrastructure, climate data, etc. [20] The database for the aerospace test site and the two test areas is supplied from time to time with new information.

Perspectives for development of the BASTSs.

One of the tasks scientific community is faced with nowadays is to develop a methodology for the construction of a web-based information system for aerospace test sites, complying with the requirements laid out by the approved documents of the GMES and GEOSS Programmes, the INSPIRE Directive, and the regional environmental characteristics. This unified methodology will be included in the requirements of the *in situ* component of the GMES and GEOSS.

A web-based information system for the BASTSs is planned to be created. It will ensure:

- Collection of experimental (in situ) data as well as results from the thematic processing of airplane and satellite images;
- Exchange of aerospace, geospatial - natural-resource and landscape-ecological information about the BASTSs;
- Provision of remote access to the electronic-information resources of the BASTSs' Scientific-Information Complex at the SRI–BAS for the scientific community;
- Development of geoinformation technologies for processing of remote sensing data and their application in Earth studies.

- Collection of data for the preparation of dissertation theses on design and development of methods, instrumentation, and technologies for remote sensing of the Earth.

An effective solution will be proposed for integration, access, analysis, and publication of the obtained information and data on the web-site, using modern procedures for browsing the available massifs of aerospace and geospatial data, providing the users with the possibility to identify their precise requirements.

Acknowledgements

The study is implemented within the framework of the contracts: Establishment of a Scientific-Information Complex for Aerospace Polygons on the Territory of Republic of Bulgaria. Contract N-НИК-003/07 between the SRI-BAS and the Scientific Research Fund at the Ministry of Education and Science, 2007 – 2008.

Res. Fell. Vanya Naydenova, PhD student, PhD student Vassil Vassilev are beneficiaries of a project of Bulgarian Ministry of Education and Science – the OP "Human Resources Development" funded by ESF, Contract BG051PO001/07/3.3-02/63/170608.

References

1. Global Earth Observation System of Systems (GEOSS). 10 Year Implementation Plan: Reference Document//Published by ESA Publication Division-Noordwijk, The Netherlands. 2005-210 p.
2. The Global Earth Observation System of Systems, http://www.earthobservations.org/geoss.shtml
3. Global Monitoring for Environment and Security (GMES): For Greater Security of the Planet. COMMITTEE OF EUROPEAN COMMUNITIES COM (2008) 748 final. Brussels, 12.11.2008. (in Bulgarian).
4. Directive 2007/2/EU of the European Parliament and the European Council from 14 of March 2007 for establishment of infrastructure of spatial information in the European Community (INSPIRE) – Official Journal of the European Union, 25.04.2007.
5. Mishev D. Remote Sensing of the Earth from Space, Sofia, Publ. House of the BAS, 1981. (in Bulgarian).
6. Spiridonov H. Space and Natural Resources, Sofia, Nauka I Izkoustvo Publ. House, 1986, p. 60. (in Bulgarian).
7. Roumenina E. 2000. Polygon Sub-Satellite Experiments in Bulgaria – State and Prospects. Proceedings of Int. Scientific Session "30 Years of Organized Research in Bulgaria". Published by SR I, BAS, Sofia. pp. 138-145. (in Bulg.).

8. Establishment of a Scientific-Information Complex for Aerospace Polygons on the Territory of Republic of Bulgaria. Contract between the SRI-BAS and the Science Research Fund at the Ministry of Education and Science of the Rep. of Bulgaria, 2007–2008.
9. Roumenina E., A. Gikov, H. Lukarski, V. Naydenova, G. Sotirov, G. Jelev, L. Filchev, L. Kraleva, S Fotev, M. Chervenyashka, P. Dimitrov, V. Kazandzhiev, N. Valkov. 2008. Establishment of a Scientific-Information Complex for Aerospace Test Sites on the Territory of the Republic of Bulgaria. Proc. of the Fourth Scientific Conference with International Participation "Space, Ecology, Nanotechnology, Safety – SENS' 2008", June 2008, Varna, Bulgaria. pp. 106-112.
10. Roumenina E. 2002. PhD Thesis. Land use and Man-Induced Transformation Monitoring of a Part of the Plovdiv Polygon Using Multichannel Images and GIS
11. Jelev G. GIS Project Structure for Geomorphologic Study of Volcanogenic Structures in the East Rhodopes, Book of Abstracts „SENS'2006" with International Participation, 2006, Varna, p.74
12. Georgiev V., R. Marinova, G. Jelev. Morphostructures in Momchilgrad depression (Eastern Rhodopes), Annual *St. Ivan Rilski* UMG, vol. 47, part I, Geology and Geophysics, Sofia, 2004, pp. 69-73.
13. Jelev G.,V. Georgiev. Identification of Ring Structures in the Region of the Strumnirishka Depression – East Rhodopes, Based on Space Images Proceedings from the Balkan Astronomical Meeting, 14-18 June 2004, Rozhen, Bulgaria, (Poster session).
14. Spiridonov H., G. Jelev. Geological-Geomorphological Interpretation of Volcanic Structures Using Space Images, Problems of Geography, vol. 5-6, 2000, 89-95 (in Bulgarian).
15. Gikov, A. Mapping and Analysis of Landscape Vegetation Development Using Various-Time Aerial Photos of the *Bogdaya* Key Area – North-West Rila. Proc. of the Int. Sci. Session *50 Years of GI-BAS*, S., 2000, pp. 190-198.
16. Gikov A., K. Stefanov. Using Aerial Photos to Map the Landscapes in Mountainous Territories. Proc. of the 2nd Sci. Conference with Int. Part. *Space, Ecology, Nanotechnology, Safety*, SRI-BAS, Varna, 2006.
17. Gikov A. Using Land Cover and CORINE Classes to Assess and Map Landscapes Anthropogenization Rate. Proc. of the 4th Sci. Conference with Int. Part. *Space, Ecology, Nanotechnology, Safety*, SRI-BAS, 4-7 June 2008, Varna, 2008. pp. 119-125.
18. Naydenova V., E. Roumenina. 2009. Monitoring the Mining Effect at Drainage Level Using Geoinformation Technologies. Central European Journal of Geosciences. Vol. 1, No 3, Sept. 2009. Publisher Versita, Warsaw, pp 318-339 http://www.versita.com/science/geosciences/cejg/
19. Naydenova V. 2009. PhD Thesis.Geographic Information System for Remote Sensing and Ground-Based Monitoring of Anthropogenic Impact in the Drainage Basin of the Kutinska River

20. R o u m e n i n a E., G. J e l e v, R. N e d k o v, V. N a y d e n o v a, G. K a n e v. A Spatial Model To Evaluate Man-Induced Transformation Using Geoinformation Technologies, Aerospace Research in Bulgaria, Space Research Institute, № 21, 2007 pp 35-47.

АЕРОКОСМИЧЕСКИ ПОЛИГОНИ В БЪЛГАРИЯ – СЪСТОЯНИЕ И ПЕРСПЕКТИВИ

Е. Руменина, В. Найденова, Г. Желев, В. Василев, Л. Кралева

Резюме

През последните десетилетия се обръща голямо внимание на интегрираното използване на наземни (*in situ*) и дистанционни данни. Практиката сочи, че надеждността и точността на информацията, получена от самолетните и сателитните изображения, зависи в голяма степен от наличието на съответни наземни (*in situ*) данни, които имат голямо практическо значение както при интерпретацията на дистанционните данни, така и при моделирането и прогнозирането на природните и техногенните процеси. Затова системите GEOSS и GMES, които се изграждат в момента, обръщат голямо внимание на този компонент. Натрупаният международен опит в областта на дистанционното изследване на Земята показва, че най-рационалният начин за получаване на *in situ* данни е създаването на мрежа от аерокосмически (подспътникови) полигони, представителни за различните климатични области и притежаващи разнообразна растителна покривка, тематично и функционално предназначение, в зависимост от задачите на полигона. По своето функционално предназначение аерокосмическите полигони в България (АКПБ) принадлежат към тестовите полигони. Първите полигони в България са създадени в началото на 70-те години на миналия век, като в момента броят им е седем. В тематично разпределената спътникова и подспътникова база данни на Научно-информационния комплекс (НИК) на АКПБ са качени много сателитни изображения и самолетни снимки, спектрометрични, радиометрични и наземни данни, които са заснети за тях. Предвижда се в близките години да бъде създадена интернет-базирана информационна система на АКПБ, която ще предоставя ефективно решение за интегриране, достъп, анализ и публикуване на получената информация и данни на Интернет-страницата.

Bulgarian Academy of Sciences. Space Research Institute.
Aerospace Research in Bulgaria. 23, 2009, Sofia

ACCURACY ANALYSIS OF MAPPING BASED ON PHOTOS AND GCPs COLLECTED FROM GOOGLE EARTH

Ramzi Ahmed

Space Research Institute – Bulgarian Academy of Sciences
e-mail: ahmedasi@hotmail.com

Abstract

The photoic maps available on Google Earth come primarily from two sources: satellites and aircraft. Google gets this imagery and other digital mapping information from sources such as TeleAtlas and EarthSat, both of which compile photos and maps into digital form for commercial applications. Because the data comes from different sources, it is provided at different resolutions, which is why some areas of the globe appear crisp even at street level while others are blurry from a great distance.

The selected test area is located in Egypt. The test area is covered by photos collected from Google Earth with an overlap and side-lap between them ranging between 15%-25%. All GCPs and CPs are collected from Google Earth, based on Universal Transverse Mercator (UTM). The minimum number of GCPs was 5 well distributed GCPs for each photo. Only two ground control points were measured from maps covering the study area on Egyptian Transverse Mercator (ETM).

After collecting the required data, the methodology procedures included: firstly, geo-referencing of each photo; secondly, generating a mosaic from the geo-referenced photos; and finally, map conversion from UTM to ETM for the produced mosaic followed by linear transformation using only 2 GCPs measured from maps.

In the present research, the accuracy test includes calculations of the discrepancies of (E, N) coordinates for 27 test points (CPs) located on the corrected mosaic. The (E, N) coordinates of check points CPs are compared with the corresponding ones derived from the existing map, which are considered as a reference in this research.

The results of this study concluded that the photos of Google Earth can be used successfully for producing maps with suitable scale in similar study area in case of lacking remotely sensed data and field observations. They also concluded that the worries of numerous countries about the level of detail available in the Google Earth must be taken into consideration.

1. Introduction

There are worries about the Google Earth program focus on national security. Officials in numerous countries have voiced concerns over the level of detail available in the Google Earth application, including Australia, Britain and the United States. The photoic maps available on Google Earth come primarily from two sources: satellites and aircraft. Google gets this imagery and other digital mapping information from sources such as TeleAtlas and EarthSat, both of which compile photos and maps into digital form for commercial applications. But the trick of Google Earth is not in compiling and storing all these images. It is in getting them to your computer quickly and efficiently. With a 56k dial-up modem, it would take 12,400 years to download a one-meter resolution image of the Earth [source: Butler]. But Google Earth makes it seem like a high-resolution picture of the entire world is right in front of you. You are not viewing the imagery in real time: according to Google, the information is no more than three-year-old and is continually updated as new data becomes available. When using Google Earth, you can zoom in, rotate, pan and tilt on an image as specific as your own front yard, view road names and local businesses and get directions from here to there. In this study, the used projection and datum are: (1) Universal Transverse Mercator (UTM); (2) Egyptian Transverse Mercator (ETM). The software package used in this study is ENVI software.

2. Test Site

The test area is Kafr az Zayat region, Egypt. The test area is covered by snapshots (photos) from Google Earth with an overlap and side-lap between them ranging between 15%-25%.

The total area = 1.5 km *1.0 km= 1.5 km^2. Figure (1) shows a snapshot of the test area which was selected for the present research. The UTM coordinates of the boundaries of the selected study area are:

UL corner = 291700, 3411900 m
LL corner = 291700, 3410450 m
UR corner = 293450, 3411900 m
LR corner = 291450, 3410450 m

Fig. 1. A snapshot of the test area which was selected for the present research.

3. Data Acquisition

The test area is covered by photos collected from Google Earth. All GCPs and CPs are collected from Google Earth, based on UTM. The minimum number of GCPs is 5 well distributed GCPs for each photo. Only two ground control points are measured from maps.

3.1. QuickBird images

The test area is Kafr az Zayat region, Egypt. The test area is covered by QuickBird, 0.599m resolution, panchromatic standard ortho-ready Level-2A date 2005-09-06. This image is partially used in this investigation for verification and visual comparison only.

3.2 Photos

In this study, snapshots (photos) from Google Earth at elevation 250m for the selected study area are taken, each of the 9 strips (from 1 to 9) containing 10 images, taking into consideration the side-lap and over-lap between the photos. The photos data are listed below:

- Area covered by one photo = 275x125 m
- Number of strips = 9
- Number of photos per strip = 10
- Total number of photos = 90

Figure (2) shows the layout of the strips and photos. Figure (3) shows photo number 6-6.

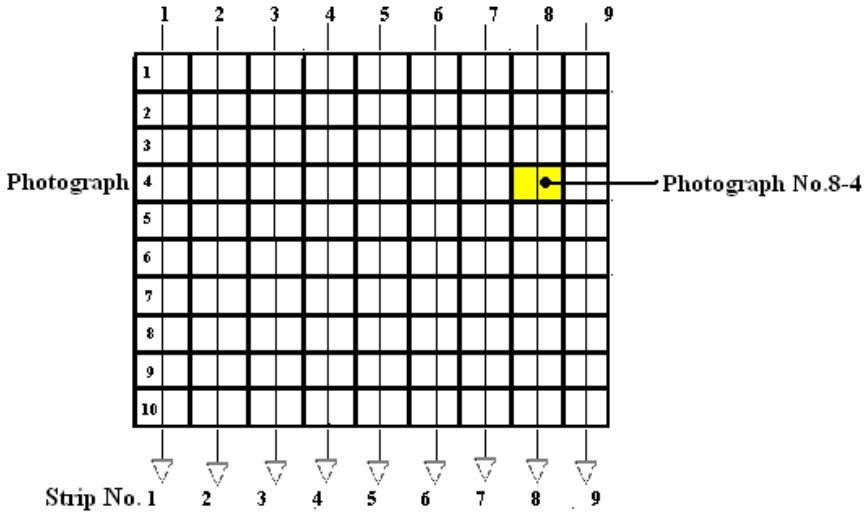

Fig.2. Layout of strips from 1 to 9 with 10 photos in each strip

Fig.3. Photo number 6-6

3.3 Ground Control Points GCPs

There are two types of ground control points used in this study:

a. GCPs collected from Google Earth

All GCPs are also collected from Google Earth, on UTM. The minimum number of ground control points for each photo is 5 points, taking into consideration that the GCPs must be well distributed over the photos and located at the corners and in the overlap area, if possible.

b. GCPs collected from available maps in scale 1/2,500

Only 2 GCPs are measured from maps in scale 1/2,500 which have been used for image transformation.

3.4 Collection of Check Points

27 well distributed sharp features were selected and identified on the geo-referenced mosaic and on the maps in scale 1/2,500. The coordinates (E, N) of these check points are measured from the maps in scale 1/2,500.

3.5 Map in scale 1/2,500

The selected study area covered with map in scale 1/2,500 was produced from aerial photos.

4. Methodology of the Practical Work

After collecting the required data, the methodology involves:

- Geo-reference of each photo based on the collected ground control points on UTM coordinate system taking into consideration the root mean square error (RMS) value for the GCPs. Approximate methods will be used to correct the images (i.e. polynomials). First order polynomial is used in this case.

- Generation of a mosaic from geo-referenced photos based on the geo-reference method in UTM coordinates system.

- Map conversion from UTM to ETM for the produced mosaic based on the transformation parameters between the two systems and using ENVI software package.

- Linear Transformation using only 2 GCPs measured from maps.

5. Results and result assessment:

5.1 Quantitative assessment of GCPs

Quantitative assessment through statistical calculations for the GCPs. Table 1 shows the residuals and the RMS for the GCPs used to correct the photos.

Table 1.Root mean square error (RMS) for the ground control points

No of GCPs	Dx (m)	Dy (m)	RMS (m)
Min 5 for each photo	Max. 0.403 Min. 0.059	Max. 0.525 Min. 0.098	Max. 0.627 Min. 0.108

5.2 UTM and ETM Mosaic

UTM mosaici from the corrected photos were created, based on the geo-reference method. Figure 4 shows the produced mosaic. Using ENVI software, the produced UTM mosaic is converted to ETM mosaic without GCPs. After that, linear transformation using only 2 GCPs measured from maps is performed to regeoreference the mossaic.

Fig.4. The produced mosaic (UTM coordinates)

5.2.1 Quantitative assessment of ETM mosaic direct conversion

Table 2 shows the total RMS of the CPs' direct conversion without GCPs. The discrepancies in the selected check points (E, N), from the geo-referenced mosaic and from the existing map in scale 1/2,500 have been calculated.

Table 2. Total root mean square error (RMS) of the check points' (CPs) direct conversion

No of CPs	Dx (m)	Dy (m)	RMS (m)
27	Max. 7.643 Min. 3.013	Max. 3.926 Min. 0.111	Max. 1.253 Min. 1.214

5.2.2 Quantitative assessment of ETM mosaic using 2 GCPs

Table 3 shows the RMS of the CPs using 2 GCPs. The discrepancies in the selected check points (E, N) from the geo-referenced mosaic and from the existing map in scale 1/2,500 have been calculated**.** Table 3 shows the RMS of the CPs using 2 GCPs.

Table 3. Root mean square error (RMS) of the check points (CPs) using 2 GCPs

No of CPs	Dx (m)	Dy (m)	RMS (m)
27	Max. 2.827 Min. 0.250	Max. 2.656 Min. 0.161	Max. 1.280 Min. 0.960

RMS_t = 1.600 m

5. Conclusions

Regarding the assessment of the obtained results, the following conclusions can be made:

- It can be stated that the accuracy of mapping from photos and GCPs collected from Google Earth and using only two GCPs from the map in scale 1/2,500 for a relatively flat terrain area gives an RMS value of 1.600 m planimetry, which satisfies theoretical large scale mapping in scale 1:3,500 and practical large scale mapping in scale 1:5,000 or less.

- The worries of numerous countries about the level of detail available in the Google Earth which can be used by terrorists must be taken into consideration.

References

1. V o l p e F. Mapping information from space with QuickBird satellite data, Third International Symposium on Digital Earth, Brno, 2003
2. R o s s i L., F. V o l p e. QuickBird high-resolution satellite data for urban applications, II GRSS /ISPRS Joint Workshop on Remote Sensing and Data Fusion over Urban Areas, Berlin, 2003, pp.1-3
3. X u t o n g N i u. Geometric modelling and photogrammetric processing of high resolution satellite imagery, Mapping and GIS Laboratory, CEEGS, The Ohio State University, 2007
4. Th. T o u t i n a, GCP Requirement for High-Resolution Satellite Mapping, Natural Resources Canada, Canada Centre for Remote Sensing, 588 Booth St., Ottawa, Ontario, K1A 0Y7 Canada, 2005
5. G e o r g i e v N. Analysis of the Precision of Georectification of Satellite Imagery Using Distributory Data vs. Ground-Based GPS Measurements, Bulgarian Academy of Sciences, Space Research Institute, Aerospace Research in Bulgaria. 18, 2003, Sofia
6. L. I s c a n a, Accuracy Assesment of High Resolution Satellite Images", General Command of Mapping, Chief of Technical Departments, 06100 Mamak Ankara, Turkey, 2005
7. F r a s e r C l i v e S. Prospects for Mapping from High-Resolution Satellite Imagery, Department of Geomatics. University of Melbourne. Melbourne VIC 3010 Australia, 2005
8. K a r t a l a F., T. E k s i o g l u a, K. E r e n a, A. A a l b. The Assessment of High Resolution Satellite Images and Applications in Regional and Local Planning, Geo Tech Group, Ankara, Turkey, Riyadh, S. Arabia, 2002

АНАЛИЗ НА ТОЧНОСТТА НА КАРТОГРАФИРАНЕ НА БАЗАТА НА СНИМКИ И НАЗЕМНИ КОНТРОЛНИ ТОЧКИ, ВЗЕТИ ОТ GOOGLE EARTH

Рамзи Ахмед

Резюме

Фотографските карти, налични в *Google Earth*, изхождат предимно от два източника – спътници и самолети satellites and aircraft. Google получава тези изображения и друга цифрова картографска информация от източници, като TeleAtlas и EarthSat, които събират снимки и карти в цифров вид с търговска цел. Тъй като данните

произхождат от различни източници, те притежават различна разделителна способност, поради което някои части от земното кълбо се виждат отчетливо дори на ниво улица, докато други са неясни дори от голямо разстояние.

Избраният тестови участък се намира в Египет. Тестовият участък е отразен в снимки, взети от *Google Earth*, чието припокриване и странично застъпване варира в границите 15%-25%. Всички наземни контролни точки и контролни точки са взети от Google Earth в Универсална трансверзална меркаторова система (UTM). Минималният брой на наземните контролни точки беше 5, добре разпределени за всяка снимка. Само две наземни контролни точки бяха измерени от карти, покриващи изследваната област в Египетска трансверзална меркаторова система (ETM).

След събиране на необходимите данни методологичните процедури включваха: първо, геопривързване на всяка снимка; второ, създаване на мозайка от геопривързаните снимки; и накрая, преобразуване на картата от UTM в ETM за създадените мозайки, последвано от линейно преобразуване с помощта на само 2 наземни контролни точки, измерени по карти.

В това проучване, проверката за точност включва изчисляване на несъответствията в координатите (E, N) за 27 контролни точки, разположени върху коригираната мозайка. Координатите (E, N) на контролните точки се сравняват със съответните координати, получени от наличната карта, която е приета за еталон в проучването.

Резултатите от това проучване показват, че снимките от Google Earth могат да се използват успешно за създаването на карти в подходящ мащаб в подобни области на изследване при липса на дистанционни данни и полеви измервания. Те показват още, че тревогата на голям брой страни за нивото на подробности в *Google Earth* са основателни.

Bulgarian Academy of Sciences. Space Research Institute.
Aerospace Research in Bulgaria. 23, 2009, Sofia

SPECTROPHOTOMETER FOR STUDY OF ATMOSPHERIC OZONE

Garo Mardirossian, Stiliyan Stoyanov

Space Research Institute – Bulgarian Academy of Sciences
e-mail: mardirossian@space.bas.bg

Abstract

A paper is presented for the design of a spectrophotometer intended to study the total content of atmospheric ozone based on the absorption principle. The device is designated to operate in the near ultraviolet part of the optic spectrum, where the Hartley–Huggins absorption bands are located and it also provides information from observations in the visible part of the optic spectrum with the Chappuis absorption band. The basic diffracting element of the designed spectrophotometer is the diffraction grating. A photometric channel is provided which reads surface albedo and sun protuberance.

In [1–5], the requirements for rational selection of scanning radiometers and spectrophotometers' parameters are specified and the method developed to calculate the optimal parameters of the optic-electronic tract is presented. This provides to minimize the total error at measuring the brightness of non-homogeneous emission and ensures the specified accuracy for measurement of average brightness during studies of non-homogeneous emissions of arbitrary form, such as the spectral composition of atmosphere.

The contribution aims to develop a method for rational selection and evaluation of the optic-electronic tract's transmission characteristics parameters in a scanning spectrophotometer intended to register dot-source emissions (the Sun, the Moon) which, while passing through the atmosphere, provide to determine the spectral composition of the atmosphere using absorption methods.

The spatial variations of emission brightness are, in their essence, external noise, against the background of which dot-source emissions are registered (atmospheric turbulence, silvery cloudiness etc.).

In practice, usually a spectrophotometer is required to have rectangular view field with uniform sensitivity and to scan along the x line with angular velocity ω_x.

In developing the method, it was assumed that the emission is registered by a receiver with predominant white noise, the optic system is isoplanar, the function has the form of a 2D Gaussoid, the electronic tract describes the product of the transmission characteristics of n pieces of integrating units with one and the same time constant, and external and internal noises at the output of the optic-electronic tract are uncorrelated.

In case of registration of dot-source emissions, it is expedient to determine the parameters of the optic-electronic tract (angular view field along the scanning lines ω_x, accordingly along the y line – ω_y; time constant of the units of the electronic tract τ; angular size of the dissipation spot of the optic system ω_a) based on the total measurement error minimization conditions. In the case of registration of a signal originating from a remote dot emitter, the total least square error ε is equal to:

$$\varepsilon^2 = \varepsilon_a^2 + \varepsilon_\tau^2 + \varepsilon_t^2 + \varepsilon_f^2 \quad (1)$$

and it includes in itself the systematic errors caused by the part of energy lost while the emission passes through the image analyzer – ε_a, the effect of the time constant and the pulse form at the input of the electronic tract – ε_τ, as well as the random errors – ε_τ, related with the noise's dark component and the background brightness' fluctuation – ε_f.

The constituent signal errors caused by the internal noises of the optic-electronic tract are known and may be determined by the formula:

$$\varepsilon_t = \frac{S_v P_t^2 Q T B_f W_a^2 \alpha\beta}{4\tau}, \quad (2)$$

where: S_v – integral sensitivity of the emission receiver;

P_t – threshold sensitivity in dark regime;

Q – useful area of the input slit;

T – transmittance capacity of the optic system;

B_f – average component of background brightness;

$$\alpha = \frac{W_x}{W_a} \ ;$$

$$\beta = \frac{W_y}{W_a} \ .$$

The systematic component of signal errors may be determined using the equation for dot-source signal at the output of an ideal receiver which may be derived using the dissipation function:

(3) $$u(t) = S_v F \frac{\beta}{2} \left(\alpha - \frac{2V_x}{W_a} \right) + \left(\alpha + \frac{2V_x}{W_a} \right) \quad ,$$

where F is the emission flow on the image plane of the dot-source (on the back focal plane of the optic system).

The reduction of the signal amplitude at the output of the optic-electronic tract as a result of the energy lost during the emission's passing through the image analyzer may be determined by the formula:

(4) $$\Delta u_a = S_v F(1 - \alpha\beta) \ .$$

The average square error is equal to:

(5) $$\varepsilon_a^2 = S_v^2 F^2 \left(\frac{1 - e^{-\beta^2}}{\beta\sqrt{\pi}} \right)^2 \frac{e^{-2\alpha^2}}{\pi\alpha^2} \ .$$

In accordance with the performed calculations and with [6], the spectrum of the signal's power G_w at the output of the electronic tract of a scanning spectrophotometer will be:

(6) $$G_w = S_v^2 T^2 Q^2 W_x^2 W_y^2 \frac{G_B}{V_x} \quad ,$$

where the power spectrum of the spatial variations of background brightness $\frac{G_B}{V_x}$, determined by Fourrier transformation is equal to:

$$\frac{G_B}{V_x} = \frac{2\sqrt{2W_f}}{V_x\left(1+2\frac{W_f^2}{V_x^2}\right)}, \tag{7}$$

and the signal dispersion at the output of the optic-electronic tract caused by the spatial variations of background brightness within the bandwidth of the electronic tract is equal to:

$$\varepsilon_f^2 = \frac{1}{\pi}\int_0^{\frac{1}{\tau}} G(w)dw$$

or

$$\varepsilon_f^2 = \frac{2\sqrt{2}}{\pi} S_v^2 T^2 Q^2 W_a^4 \alpha^2 \beta^2 \left[\frac{1}{\sqrt{2}}\operatorname{arctg}\left(\frac{\sqrt{2}\frac{W_f}{V_x}}{\tau}\right)\left(1+\frac{\alpha^2\frac{W_a}{V_x}}{\tau\frac{W_a}{W_x}}\right)\right]. \tag{8}$$

Therefore, if there are no background brightness fluctuations, the measurement errors are reduced by augmenting the view field along the scanning line, while with increasing background dispersion, the function takes the form of a minimum, corresponding to the optimal parameters of the preliminary characteristics of the spectrophotometer's optic-electronic tract.

In Fig. 1, the emission source 1 is shown, providing signal in the ultraviolet, visible and infrared part of the optic spectrum, as well as spectrophotometer 2, intended to study the spectral composition of atmosphere, and the registration module 3 of the equipment complex.

The results obtained from the evaluation analysis of the transmission characteristics of a spectrophotometer intended to study the spectral composition of atmosphere at dot-source emission registration provide to make the following conclusions:

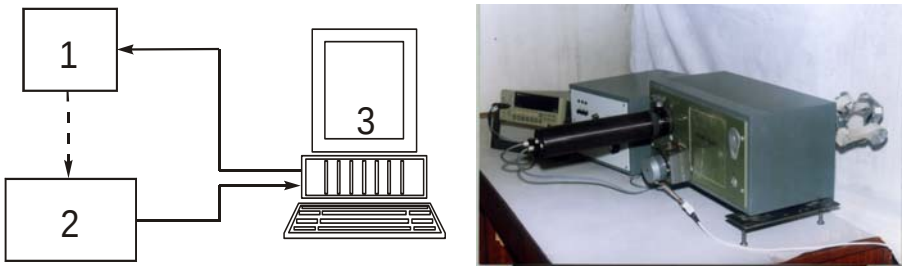

Fig. 1

1. When measuring emission originating from uniform background source, the increase of noise components as a result of the view field's augmentation along the scanning line may be compensated by reduction of the electronic tract's bandwidth at increasing measurement accuracy, whereas the rational selection of the optic-electronic tract's transmission characteristics parameters is substantiated primarily by the device's structural features according to the conditions of the experiment.

2. In the presence of spatial background variations, the developed method allows for a compromise between the influence of the systematic error ε_a at small α and the random error ε_f at increase of α, providing to minimize the total ε for the conducted measurements.

References

1. А р а б о в А., Н. Е л а н с к и й, Ю. Т р у т ц е. Некоторые результаты измерений общего содержания атмосферного озона и двуокиси азота в атмосфере с самолета, Труды совещания по озону, Москва, 2007.
2. Г у щ и н Г. Исследование атмосферного озона, Гидрометеоиздат, 2003.
3. К о з л о в В., Ю. М. Т и м о ф е е в. Об оптимальных условиях измерений уходящого излучения в полюсах поглощения и точности метода термического зондирования атмосферы, Изв. РАН, ФАО,2003, т. 15, № 12.
4. К у з н е ц о в Г. Опыт использования комплекса апаратуры для атмосферно - оптических наблюдений озона и озоноактивных компонент атмосферы, Тр. совещ. по озону, Москва, 2000.
5. Т и м о ф е е в Ю., М. Б и р ю ш и н а, В. К о з л о в. О точности определения содержании озона в атмосфере по данным измерений уходящего излучения, Метеор. Гидрол., 2000, № 3.
6. Х р г и я н А., Г. К у з н е ц о в. Проблемы наблюдений и исследование атмосферного озона, Москва, Изд. МГУ, 2001.
7. Г у щ и н Г. Исследование атмосферного озона, Гидрометеоиздат, 2003.

8. К у з н е ц о в Г. Опыт использования комплекса апаратуры для атмосферно - оптических наблюдений озона и озоноактивных компонент атмасферы, Тр. совещ. по озону, Москва, 2000.
9. Х р г и я н А., Г. К у з н е ц о в. Проблемы наблюдений и исследование атмосферного озона, Москва, Изд. МГУ, 2001.
10. A r u g a T., T. I g a r a s h i. Vertical distribution of ozone: a new method of determination using satelliete measurements., Appl. Optics, 2006, vol.15. No1.
11. C a t e J., S. M a t e e r. A preliminary study on the possibility of total atmospheric ozone from satellite measurements., Appl. J. Atoms. Csi, 2007, vol.15, No3.
12. S t r o n g J. On a new method of measuring the mean height of ozone in the atmosphere, J. Franklin Inst., 2001, vol.231, No2.
13. C a t e J., S. M a t e e r. A preliminary study on the possibility of total atmospheric ozone from satellite measurements., Appl. J. Atoms. Csi, 2007, vol.15, No3.
14. F l e i g A. et. al. User's guide for the solar backscatter ultraviolet (SBUV) instrument first-year ozone-S data set / NASA Ref. Publ. 1095; NASA GSFC; Greenbelt. MD 1982. 72 p.
15. S t r o n g J. On a new method of measuring the mean height of ozone in the atmosphere, J. Franklin Inst., 2001, vol.231, No2.

СПЕКТРОФОТОМЕТЪР ЗА ИЗЛЕДВАНЕ НА АТМОСФЕРНИЯ ОЗОН

Г. Мардиросян, С. Стоянов

Резюме

Представено е изследване за разработване на спектрофотометър, който на базата на абсорбционния принцип да осигурява изследване на общото съдържание на атмосферния озон. Апаратурата е предназначена за работа в близката ултравиолетова част от оптичния спектър, където са разположени ивиците на абсорбция на Хартли – Хюйгенс и предоставя информация и от наблюдения във видимата област с ивица на абсорбция на Шапюи. Като основен дифрагиращ елемент с разработвания спектрофотометър е използвана дифракционна решетка. Предвиден е фотометричен канал, отчитащ влиянието на албедото на подстилащата повърхност и протуберанса на Слънцето.

Bulgarian Academy of Sciences. Space Research Institute.
Aerospace Research in Bulgaria. 23, 2009, Sofia

NEW LEDs LIGHT MODULE DEVELOPED UNDER THE *GREENHOUSE-MARS* PROJECT

Tania Ivanova[1], Ivan Dandolov[1], Iliana Ilieva[1], Yordan Naydenov[1]
Margarita Levinskih[2], Vladimir Sychev[2]

[1]Space Research Institute - Bulgarian Academy of Sciences
e-mail: tivanova@space.bas.bg
[2]State Scientific Center - Institute of Biomedical Problems
76A, Khoroshevskoe shosse, Moscow 123007, Russia

Abstract

According to the Greenhouse-Mars Contract for scientific cooperation between the Space Research Institute, Sofia, and the Institute of Biomedical Problems, Moscow, Bulgarian scientists developed a new Light Module on light-emitting diodes (LM-LED). A new LM-LED was developed with monochromatic LEDs (Cree® XLamp® 7090 XR) emitting in the red, green and blue (RGB) spectral range. DMX control unit was used to set up a predefined Photosynthetic Photon Flux Density (PPFD) within the range of 0-400 µmol.m^{-2}.s^{-1}. Laboratory technical and biological tests of the LM-LED were completed using the equipment of the SVET-2 Space Greenhouse (a prototype of the one flown onboard the MIR Orbital Station). Two one-month experiments with lettuce and radicchio plants were carried out with the new LM-LED (spectral composition - 70% red, 20% green and 10% blue light) and PPFD – 400 µmol.m^{-2}.s^{-1} (high light) and 220 µmol.m^{-2}.s^{-1} (low light). Plant growth and some biochemical parameters were evaluated and compared to the results from similar experiments carried out with SVET-2 SG Light Module on fluorescent lamps (OSRAM DS 11/21). The paper includes a review of our research and development activities under the Greenhouse–Mars Project during the past 3 years (2006-2008).

Background

The *Mars-500* Experiment is under development by the Russian State Scientific Center - Institute of Biomedical Problems (IBMP), Russian Academy of Sciences, Moscow. During the experiment, six volunteers will

be locked for 500 days in a mock-up of the space station modules to Mars in an effort to mimic the stresses and challenges of a long manned mission and how they affect the human crew. The simulation of a manned flight to Mars is planned to start in the late 2009 or early 2010. During the 500-day study, the life of the six men will depend on a preset limit of supplies, including about 5 tons of food and oxygen and 3 tons of water. A doctor will accompany the volunteers inside the module to treat illnesses or injuries. Volunteers will only be allowed to quit the experiment if they develop a severe ailment or psychological stress. A large greenhouse will be installed inside, supporting the life and the health of the "crew", providing them with fresh food and relaxing "green view".

A research team from the Space Research Institute (SRI), Bulgarian Academy of Sciences, Sofia, has been participating in the Russian Program for preparation of a human spaceflight to Mars for 25 years already. The first small-size (0,1 m^2) SVET Space Greenhouse (SG) was created in the 80's under a Joint Scientific Project with the IMBP in the framework of the *Intercosmos* Programme, aiming to study the ways and methods for the use of higher plants in space Biological Life Support Systems (BLSS). The subject of the project was to develop biotechnology for higher plants growing in microgravity with the prospects to use it in the future long-term manned mission to Mars. SVET SG was launched onboard the MIR Orbital Station (OS) in 1990 when the first two-month vegetable plant experiments were carried out to provide vitamin addition to the astronaut food [1]. Artificial lighting was provided by fluorescent lamps mounted in the Light Unit (LU). A new modification, SVET-2 SG, with optimized parameters of all units and systems (including new LU-2) was developed and launched onboard the MIR OS in 1996, which was funded by NASA [2]. A number of successful plant experiments and research were carried out under the fluorescent lamps lighting of the SVET-2 SG equipment in 1996-2000. The unique scientific results obtained in the field of Gravitational Plant Biology proved that there were no "show-stoppers" for plant growth and development in microgravity [3, 4].

Plants need light of definite quantity and quality. They consume light energy mostly in two spectral bands - blue and red (around 450 and 650 nm) to carry out their fundamental biological processes, such as photosynthesis (production of biomass and air cleaning) and phototropism (orientation towards the light in weightlessness). The intensity of these physiological processes with light of various wavelengths is shown in Fig. 1

(curve 1 - phototropism and curve 2 - photosynthesis). To provide experimentally defined light conditions of irradiance, spectral quality, and duration is one of the major engineering requirements of any controlled environment plant chamber [5].

The Bulgarian-made LU with lighting area of 330x330 mm can be moved vertically in the Plant Chamber of SVET SG and adjusted at three different levels: 20, 30 and 40 cm from the plant seedling surface in order to provide best light intensity without overheating, depending on the plant development stage. A fan cooling the lamps and the air in the shoot zone is mounted on the upper bearing plate together with a panel for LU control (manual or automatic).

Russian fluorescent lamps LB 8-6 (12 pieces) developed specifically for the MIR OS board were used in the 1990 experiment. The spectral-response characteristic of LU using this kind of lamps is shown by curve 3. It is seen that almost the whole luminous energy is concentrated in the plants' lower sensibility area. This appreciable discrepancy between the light source and plant needs was due to the lack of special lamps (during the period of development) with appropriate characteristics which necessitated a great enough stock in case of breaking a lamp. The fluorescent lamp DS 11/21 of OSRAM (6 pieces) was chosen as featuring the most appropriate spectrum for LU-2 (curve 4) – intensive photosynthesis and providing phototropism of the plants, which are so important in space flight conditions [6].

Considerably (2.5 times) improved brightness characteristics of LU-2 were obtained at a distance of 15 cm from the illuminants, the intensity being 27,000 lx (under 12,000 lx in SVET SG in 1990). In these circumstances, we could expect considerable increase of plant productivity (biomass quantity) in the future experiments.

The larger warranted duration of work of the lamps DS 11/21 (8,000 hours) results in 5-fold increase of the equipment's reliability. Apart from this, the new LU-2 features appreciably better electrical characteristics, which is of great importance because it used to be the greatest energy consumer within SVET SG. For example, the supply current of the unit (under 27V onboard supply voltage) is 2.5 times lower (3.5A under 9A in SVET SG) and the starting current is almost equal to the normal one [7].

Unfortunately, the lighting systems based on white fluorescent lamps used in plant growing facilities were developed more for human and not for plant lighting purposes, since the well-lit green plants have very positive

psychological effect on the space crew. Nevertheless, such lighting systems have found extensive use in terrestrial facilities with controlled environment.

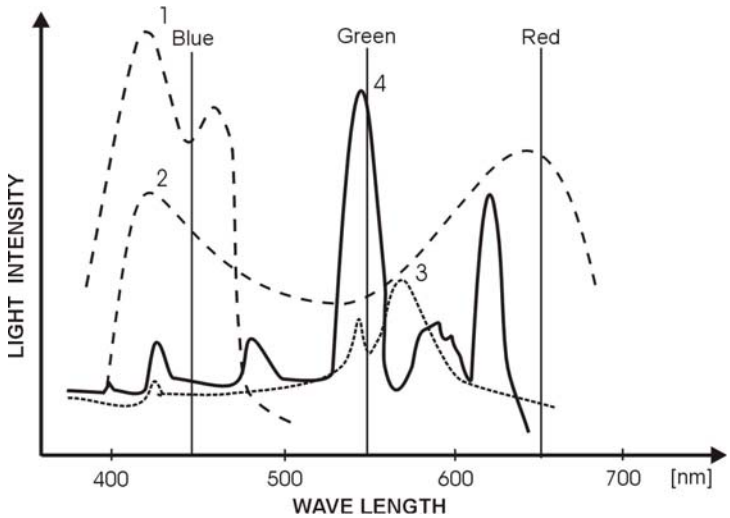

Fig. 1. Light wavelength necessary for plants: 1 - phototropism and 2 – photosynthesis; Spectral characteristics of the fluorescent lamps used in 3 - SVET SG (LB 6-8) and 4 – SVET-2 SG (DS 11/21) and of the new blue, green and red LEDs

Regarding the use of fluorescent lamps in space-based plant chambers there are serious limitations relating to both the power utilization and the safety requirements of the space hardware. The mercury contained in the lamps may be a serious safety hazard, if a lamp is broken. The LU-2 OSRAM lamps were hermetically sealed in specifically developed light bodies that ensure maximum light characteristics. The safety requirements are adequately addressed but the irradiance of these lighting systems is greatly decreased and the volume required by such a system is difficult to accommodate in the very limited LU space.

Lighting system on light-emitting diodes

The plant will be an important component of the future BLSSs for the long-term space mission to Mars as a source of food and air cleaning. The lighting systems intended for long-term plant growing should be light-weight, reliable, and durable, and light-emitting diodes (LEDs) possess all

these characteristics. The development of LED-based LUs for space greenhouse facilities started in USA in the 90's in relation with the Space Shuttle missions [8].

Major advances have been achieved in semiconductor technology and this has led to the availability of LEDs having sufficient photon output and electrical efficiencies making them an excellent light source for plant growing facilities. Mounting the LED chip on a highly thermally conductive ceramic substrate which is bonded to a metal heat sink allows the device to operate at high normal current with high photon output, while maintaining the temperature of the LEDs close to the ambient temperature, resulting in prolonged life and constant photon output.

Since, in contrast to other lamps, LEDs emit photons within a specific spectral range, they should be carefully selected, so that the levels of the provided photosynthetically active, photomorphogenic, and phototropic radiation meet the plant requirements. Photons in the red spectral range are most efficient as a source of photosynthetically active radiation (Fig. 1). Thus, LEDs having a peak emission around 650 nm appear to be the most efficient source providing photons for the photosynthesis, which coincides with the red absorption peak of chlorophyll. Irradiance levels of 0-500 $\mu mol.m^{-2}.s^{-1}$ in the red spectral range can be achieved using an LED plant lighting unit. Light in the blue spectral range (400 to 500 nm) featuring low irradiance levels (0-80 $\mu mol.m^{-2}.s^{-1}$) is generally considered to be involved in the photomorphogenic and phototropic responses. The light requirements involved in the phytochrome responses can be easily met by low light levels with wavelengths of 630 and 680 nm. Supplementing the red photon LEDs with others emitting in the blue (450 nm) and infrared (735 nm) spectral range would meet plants' light requirements in a controlled environment facility [9].

A Light Unit with 90% red and 10% blue LEDs was used in the American ASTROCULTURE^{TM} Greenhouse flight unit during three Space Shuttle missions, STS-57, STS-63, and STS-73, as well as in the commercial ADVASC flight unit on ISS [10]. The video from the board showing the dark-violet coloured plants was terrible, but fortunately, they were not visible for the crew in the closed chamber. In terms of photon output, the performance of the LED unit while in a space environment was the same as the performance while tested on the ground. In addition to being used as a lighting source in plant growth chambers, the LEDs can be a very

effective photon source for photosynthetic research to study electron transport, carbon metabolism and trace gas emission.

A greenhouse with large plant area of 3 m^2 will be mounted "onboard" during the *Mars-500* Experiment (in a module of 250 m^3 volume) together with the required water and food supplies to ensure fresh vitamin addition to the "cosmonaut" food. A Contract for scientific cooperation on the *Greenhouse-Mars* Project between the SRI and the IBMP was signed in the framework of an agreement between the Bulgarian and the Russian Academy of Sciences in the field of Fundamental Space Research for the period 2006-2010 [11]. According to this Contract, part of the Greenhouse equipment, Light Units with different spectra (combinations of LEDs) intended for the scientific plant experiments during the *Mars-500* were developed.

Previous studies demonstrated that the combination of red and blue light was an effective light source for several crops. Yet, the appearance of plants under red and blue lighting is purplish-gray making visual assessment difficult. The addition of green light would make plant leaves appear green and normal, resembling a natural setting under white light, and may also offer a psychological benefit to the crew which is very important for long-term living in a closed system surrounded by technical equipment only [12].

Green supplemental lighting could also offer benefits, since green light can better penetrate plant canopy and potentially increase plant growth by increasing photosynthesis in the lower canopy leaves. The American experimental study proved that plants treated with red and blue LEDs and with additional green fluorescent lamps produced more biomass than the plants grown under white fluorescent lamps [13]. Now, it is not clear enough what the optimal spectra of the future LED LUs should be to achieve maximum plant productivity.

Technical characteristics of the new LM-LED

The Bulgarian team of experienced engineers and young biologists from the SRI developed at the beginning only one small Light Module on LEDs (LM-LED) [14]. The technical specifications for them were set by the Russian experts from the IBMP. The most important requirement was to ensure highly reliable, continuous and flawless operation for at least 18-24 months, so we took special measures to cool the unit, so as to maintain constant electrical and thermal characteristics.

The main technical characteristics of the LM-LED are as follows:

- Lighting area's size - 33x33 cm, same as the size of the LM on fluorescent lamps. The new LM-LED replaced it without any problem in SVET-2 SG, where we conducted the tests. Nine modules with these dimensions will be sufficient to build 1 m^2 of lighting area;
- Distance from the LM-LED to illuminated area – up to 50 cm. The distance could be varied within 20-50 cm, with step of 10 cm, so as to use the full power of the LEDs in the different plant development stages;
- Light intensity required for smooth running of plant processes Photosynthetic Photon Flux Density (PPFD) – 350-400 $\mu mol.m^{-2}.s^{-1}$;
- Spectral characteristics: blue (450 nm), green (550 nm), red (650 nm), ±30 nm (see Fig. 1);
- Simulation of the following spectral ranges, by changing the light intensity or the number of switched on LEDs at any moment:
    1. 50% blue, 20% green, 30% red;
    2. 30% blue, 20% green, 50% red;
    3. 10% blue, 20% green, 70% red;
    4. 10% blue, 90% red.

Since the emission intensity of the LEDs for the different spectral ranges is different, a different number of them are switched on for the different colours.

A special facility was developed for experimental measurements of PPFD. Portable measuring system LI-6400 - LI-COR was used. A series of measurements of the intensity of different commercially available types of LEDs were made.

Based on these measurements, we chose XLamp XR produced by the US company *Cree*, which matched best the technical requirements [15]. This choice reduced significantly the total number of LEDs and simplified the design of the LU. The XLamp XR type of LEDs were among the newest products from this family. They can be operated with currents up to 700 mA (equivalent to the power of 3 W), which allows variation of light intensity within a wide range to achieve the objectives of the planned experiments. Based on long-term reliability testing and standardized forecasting methods, the LEDs of this series will keep up to 70% of their light intensity after

50,000 hours of work, provided that the solder place temperature does not exceed 80°C.

Prismatic optical system developed by *Polymer Optics Ltd.* [16], mounted in front of each LED spot generates homogeneous light beam.

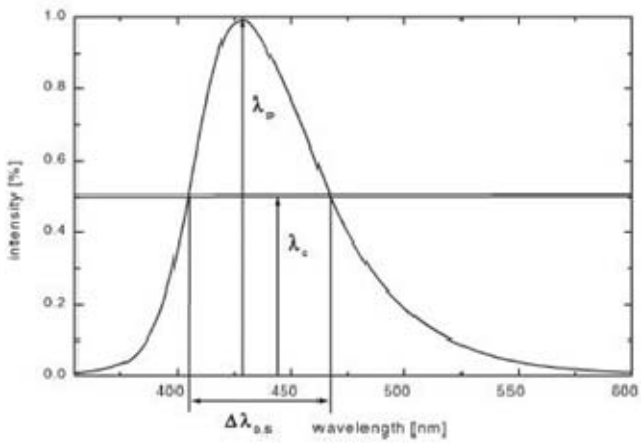

Fig. 2. Calculating FWHM (full width at half maximum)

The spectral distribution of the LEDs differs in many aspects from that of conventional light sources. It is not monochromatic, as laser emission, or with a broad spectrum, as most light sources with incandescent wire. LED has a typical spectral width - FWHM (full width at half maximum) of 15 to 60 nanometres (Fig. 2). In this case, the spectral width of the LED emission for normal distribution ($\Delta\lambda_{0.5}$) is calculated by finding the difference ($\Delta\lambda_{0.5}$) between the wavelengths with ½ of the maximal intensity λ_p, i.e. $\lambda'_{0.5}$ and $\lambda''_{0.5}$:

$$\Delta\lambda_{0.5} = \lambda'_{0.5} - \lambda''_{0.5}$$

For the selected LEDs, we obtain the following:

LED (color)	λ_p	$\lambda'_{0.5}$	$\lambda''_{0.5}$	$\Delta\lambda_{0.5}$
Blue	468	455	480	25
Green	525	505	545	40
Red	632	625	640	15

There is relative overlap between the spectra from the technical requirements and the spectra of the selected LEDs.

Construction and methods of control

In order to describe better the structure and control of LM-LED, we will introduce the following basic concepts:

Fig. 3. Photo of the LM-LED and the DMX Control Unit

- Light source (LS) – a powerful LED with red, green or blue colour;
- Element – a light source with unique identification number (from 1 to 255);
- LED spot – a spot containing three elements;
- Group – a set of elements arranged in one or more spots which are controlled jointly. It is possible to define up to 255 groups. Each element can participate in one or several groups.

The Block Diagram of the LM-LED is shown in Fig. 4. 36 LED spots are installed on a metal plate with heat sinks to maintain optimal temperature during continuous operation. A standard Power Supply of 500W, 24V, 20A is used.

The DMX Control Unit is connected to six DMX LED controllers and six LED spots are coupled to each one. 30 LED spots contain green, red and blue LS, and 6 LED spots - 3 red LSs each. The proposed design allows setting up to 255 different levels of light intensity for each element and provides for easy change of the elements belonging to each group.

This method of work facilitates the variation of spectral characteristics and light intensity within a wide range, which allows to conduct very accurate experiments with different crops to find the optimal regimes for each crop.

Special instructions loaded in the memory of the DMX Control Unit are used to control the spectral characteristics and light intensity of the LM-LED according to a pre-set schedule. Each instruction controls a group of elements, allowing elements from other groups to retain or change its state.

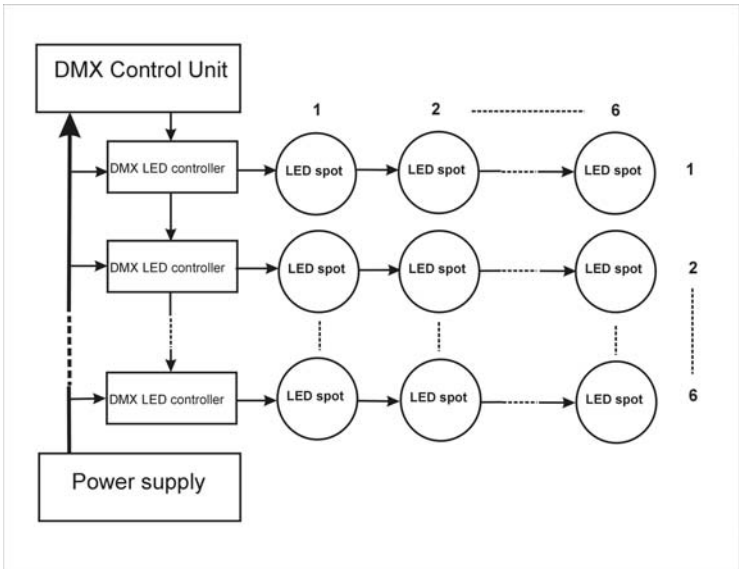

Fig. 4. Block diagram of the LM-LED

The main parameters of the instruction are:

- Instruction number (0-255);
- Group number (0-255);
- Standard program code (0-4);
- Number of cycles (1-255) - indicates how many times to repeat the instruction;
- Initial intensity - red, green, blue (0-255);
- Final intensity - red, green, blue (0-255);
- "Switched on" time (0-25.5 s);
- "Switched off" time (0-25.5 s);

- Start of the allowed astronomical time window (from 00:00 to 23:59) - the instruction is executed only within the allowed astronomical time window;
- End of allowed astronomical time window (from 00:00 to 23:59);
- Active days of the week - the instruction is executed only on the active days of the week.

The available standard programs for the control of LM-LED are:

Program code 0 – Turns all elements of the group into "switched off" state.

Program code 1 – All elements that were switched on by the previous instruction preserve their state. All elements of the group are switched on and shine with constant intensity equal to the value in the field “initial intensity”.

Program code 2 – Switches off all elements that were switched on by the previous instruction. All elements of the group are switched on and shine with constant intensity equal to the value in the field “initial intensity”.

Program code 3 – All elements that were switched on by the previous instruction preserve their state. All elements of the group are switched on and shine with constant intensity equal to the value in the field “initial intensity” for "Switched on" time, and are switched off for "Switched off" time.

Program code 4 – Switches off all elements that were switched on by the previous instruction. All elements of the group are switched on and shine with constant intensity equal to the value in the field “initial intensity” for "Switched on" time, and are switched off for "Switched off" time.

The results of the experiments conducted with the new LM-LEDs will allow us to create a balanced spectral lighting system based on LEDs and to find the optimal ratio between consumed energy and yield.

Experimental Verification Tests of LM-LED

Laboratory technical and biological tests of the LM-LED were conducted using the equipment of SVET-2 SG in the air-conditioned Laboratory of the SRI. The model consists of Control Unit and PGC in which the changeable Root Module and LM are placed. The LM-LED could be used interchangeably with the original LM on fluorescent lamps (LM-FL). The ME-4610 universal data acquisition system *produced by Meilhaus Electronic GmbH* was added to SVET-2 SG to process, store, and visualize

the data acquired from the sensors located in the leaf-zone of PGC. The process of monitoring the shoot zone 5 parameters (air temperature and humidity, light intensity, air flow velocity, and air pressure) and the control of RM substrate moisture is automatic [17]**.**

Two one-month experiments with lettuce (*Lactuca sativa L. var. acephala Dill. cv. Lollo Rossa*) and radicchio (leaf chicory) (*Cichorium intybus L. subsp. intybus (Foliosum Group) cv. Bianca di Milano*) were carried out using the new LM-LED [18]. The LM-LED was positioned at 20 cm in the PGC and ensured 400 $\mu mol.m^{-2}.s^{-1}$ PPFD (high light - HL) for the first experiment and 220 $\mu mol.m^{-2}.s^{-1}$ PPFD (low light - LL) for the second experiment and spectral composition of 70% red, 20% green, and 10 % blue light during both experiments. Another two one-month experiments with the same plants but using LM-FL were carried out. In the first experiment, the LM-FL was positioned 40 cm above the seed sowing surface to ensure 120 $\mu mol.m^{-2}.s^{-1}$ PPFD (low light - LL) and in the second one, 20 cm above the seed sowing surface to ensure 220 $\mu mol.m^{-2}.s^{-1}$ PPFD (high light - HL). Both varieties were cultivated together in each of the experiments. Lettuce and radicchio seed germination, seedling height and dry matter accumulation were measured to assess plant growth. Biochemical parameters were also evaluated – Malonedialdehyde (MDA), H_2O_2 and Peroxidase activity (POX) reflect the extent of photodamage on lettuce and radicchio plants. These morphometric and biochemical data were used to estimate the impact of light intensity and spectral composition on cultivated plants.

Results and Discussion

All analyses were made in the end of the experiments, except for seed germination which was evaluated during the first 10 days of each experiment.

When fluorescent lamps are used as a light source, germination rate of lettuce seeds decreases by 27% as PPFD increases from 120 to 220 $\mu mol.m^{-2}.s^{-1}$. The germination period also decreases twice, from 6 to 3 days. Radicchio germination rate shows different dependences on changes in light intensity – the number of germinated plants increases by 16% while the germination period remains the same, although it is shifted one day left at the higher light intensity (Fig. 5). Germination rate of both lettuce and radicchio seeds cultivated on LEDs decreases as PPFD changes from 220 to 400 $\mu mol.m^{-2}.s^{-1}$ by 5% and 14%, respectively. The beginning of the

germination period remains the same for each of the varieties and the longevity is statistically equal at the two light intensities (Fig. 6).

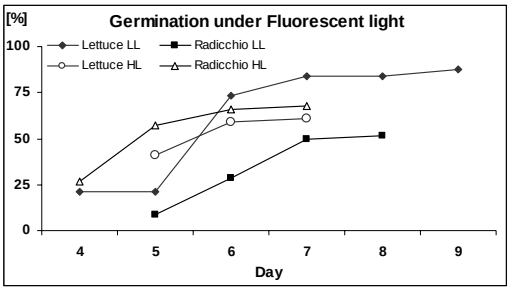

Fig. 5. Lettuce and Radicchio germination rate during experiments using the Light Module on Fluorescent lamps.

Abbreviations:
LL - Low Light Intensity - 120 µmol.m^{-2}.s^{-1}PPFD;
HL -High Light Intensity - 220 µmol.m^{-2}.s^{-1}PPFD.

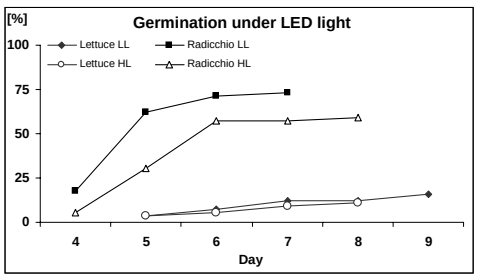

Fig. 6. Lettuce and Radicchio germination rate during experiments using the Light Module on LEDs.

Abbreviations:
LL – Low Light Intensity – 220 µmol.m^{-2}.s^{-1} PPFD;
HL – High Light Intensity – 400 µmol.m^{-2}.s^{-1} PPFD.

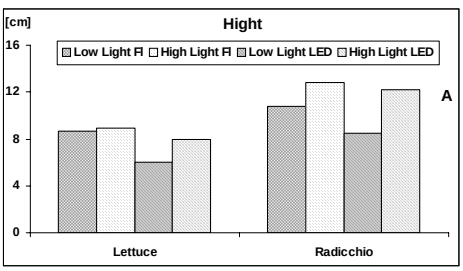

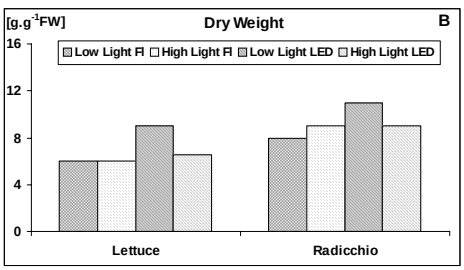

Fig.7. Morphometric characteristics of Lettuce and Radcchio plants during experiments with LM-FL and LM-LED.

7-A: Height and 7-B: Dry Weight.
Used abbreviations are:
Low Light FL (fluorescent) - 120 µmol.m^{-2}.s^{-1} PPFD;
High Light FL (fluorescent) - 220 µmol.m^{-2}.s^{-1} PPFD;
Low Light LED -220 µmol.m^{-2}.s^{-1} PPFD;
High Light LED -400 µmol.m^{-2}.s^{-1} PPFD.

Regardless of the lighting source, plant height within each plant variety is nearly the same in all experiments, except at 220 µmol.m^{-2}.s^{-1} LED light when decrease by almost 30% for both plants was observed (Fig. 7-A). Just the opposite effect – increase of dry weight was observed when low intensity of LED light was used (Fig 7-B).

Accumulation of high levels of MDA (Fig. 8-A) and increased POX activity (Fig. 8-C) correlated with decreased endogenous H_2O_2 content (Fig. 8-B) were observed in HL LED grown plants – both lettuce and radicchio. High light is known to induce photodamage in plants by enhancing photooxidation. This could be assessed by changes in MDA, waste product of lipid peroxidation. As seen from Fig. 8-A, B, C, plants grown under

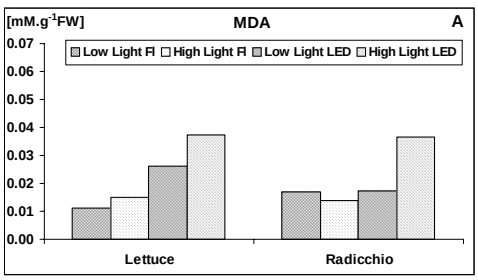

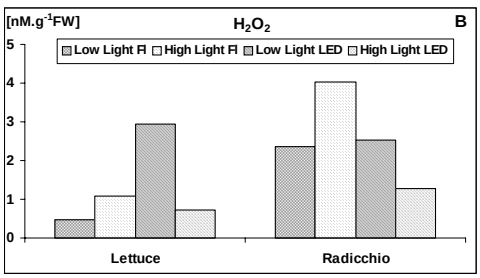

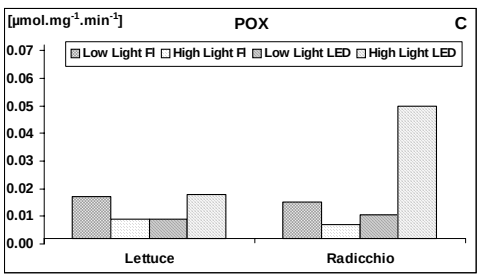

Fig. 8. Biochemical characteristics of Lettuce and Radicchio plants during experiments with LM-FL and LM-LED.

8-A: Malonedialdehyde (MDA), 8-B: Hydrogen peroxide (H_2O_2) and 8-C: Peroxidase activity (POX).

Abbreviations:
Low Light FL (fluorescent) - 120 µmol.m^{-2}.s^{-1} PPFD;
High Light FL (fluorescent) - 220 µmol.m^{-2}.s^{-1} PPFD
Low Light LED - 220 µmol.m^{-2}.s^{-1} PPFD;
High Light LED - 400 µmol.m^{-2}.s^{-1} PPFD.

fluorescent light accumulated small amounts of MDA compared even to LL LED grown plants, both lettuce and radicchio. The biochemical set of parameters revealed that low and high LED light induces photooxidation protection reactions in both plants. HL LED grown plants are more sensible to photooxidation but not to a greater extent than the LL LED grown plants.

Conclusion

Two one-month experiments with the new LM-LED were carried out to study the effect of light intensity and spectral composition on lettuce and radicchio plants. Light intensities were 400 $\mu mol.m^{-2}.s^{-1}$ PPFD (high light - HL) and 220 $\mu mol.m^{-2}.s^{-1}$ PPFD (low light - LL). The spectral composition was 70% red, 20% green, and 10% blue light during both experiments. This spectral composition ensured white light at which plants looked green and pleasant for human eyes. These experiments revealed that LL LED grown plants accumulated the highest dry weight compared to HL LED and cool white fluorescent lamps, both LL (120 $\mu mol.m^{-2}.s^{-1}$ PPFD) and HL (220 $\mu mol.m^{-2}.s^{-1}$ PPFD). The biochemical analyses revealed that light emitted from LEDs unlocks photoprotection reactions in lettuce and radicchio plants cultivated at 70% red, 20% green, and 10% blue light.

Other experiments are carried out to study the different light intensity and spectral composition levels (10% blue, 90% red and 30% blue, 20% green, 50% red) to develop an optimal plant growth technology.

Prospects

Photoprotective plant reactions to high light intensity were observed during the Earth verification tests. Based on these findings a new LM-LED-5, on another type of LEDs (QH513) is under development. The advantages of the new LM are lower price and lower power consumption, light weight and improved effectiveness. The new universal LM, which is sized 40x40 cm and provided with separate pulse power supply of 220V will be tested during the next stage of the *Greenhouse-Mars* Project. Such a module could be easily transported to Moscow by plane to be used in biological and technical tests within the ready-built structure of the experimental model in the IBMP; it is easy to multiply (if funds are available) and to implement it in the two Mars-500 greenhouse facilities with sized 80x160 cm.

The LM-LED-5 composition has been supplemented with white light for psychological effect. Two rows of white LEDs are mounted in the

module, which will be switched on when photos are taken or the "crew" observes the plants. The most important task in both ground-based experiments carried out in the SRI and the IMBP is to find the optimal LED composition, so as to achieve the same plant growth as with fluorescent lamp lighting.

Different plant species, mostly lettuce crops, will be grown under different light spectra provided by LEDs with a small viewing angle and maximum light intensity on the plant surface during the experiment. Samples for analysis will be collected at different plant development stages to investigate the influence of light spectrum on plant physiological parameters. The psychological effect on the crew emotional frame (the "plant-operator" dependence) will also be studied during the long-term *Mars-500* Experiment.

Acknowledgments

The research was supported by grants from the Bulgarian Ministry of Education and Science – the NSF, Contract KI-1-01/03, and the OP "Human Resources Development" funded by ESF, Contract BG051PO001 /07/3.3-02/63/170608.

References

1. I v a n o v a T., Yu. B e r k o v i c h, A. M a s h i n s k i y and G. M e l e s h k o. The First "Space" Vegetables have been Grown in the "SVET" Greenhouse Using Controlled Environment. Conditions. *Acta Astronautica*, 29(8), 1993, 639-644.
2. I v a n o v a T., P. K o s t o v, S. S a p u n o v a, I. D a n d o l o v, F. S a l i s b u r y, G. B i n g h a m, V. S y t c h o v, M. L e v i n s k i k h, I. P o d o l s k i, D. B u b e n h e i m and G. J a h n s. Six-Month Space Greenhouse Experiments - a Step to Creation of Future Biological Life Support Systems. *Acta Astronautica*, Vol. 42, Nos. 1-8, 1998, 11-23.
3. I v a n o v a T., P. K o s t o v and S. S a p u n o v a. Renewing of the Greenhouse Biotechnological Experiments Onboard the MIR Space Complex. *46th International Astronautical Congress*, Oslo, Norway, 2-6 October 1995, Rep. IAF/IAA-95-G.4.01.
4. I v a n o v a T., P. K o s t o v, I. D a n d o l o v, S. S a p u n o v a. Results from Microgravity Experiments in the SVET Space Greenhouse Onboard the MIR Orbital Station, *51st International Astronautical Congress*, Rio de Janeiro, Brazil, 2-6 October 2000, Rep. IAF-00-J.3.10.

5. K o s t o v P., T. I v a n o v a and S. S a p u n o v a. Adequate Substrate Moistening System and Artificial Lighting for the Growth of Higher Plants in the "SVET" Space Greenhouse. *ACTA VET. BRNO*, Vol.65, 1, 1996, 19-25.
6. I v a n o v a T., P. K o s t o v, S. S a p u n o v a, G. B i n g h a m and S. B r o w n. Equipment for the Greenhouse SVET'95 Project and Some Optimizations for Future Experiments on board the MIR Orbital Complex. *Aerospace Research in Bulgaria*, 14, 1998, 71-77.
7. G r a m a t i c o v P. and T. I v a n o v a. SVET-2 Space Greenhouse Light Unit. *Aerospace Research in Bulgaria*, 16, 1999, 24-34.
8. B u l a R., D. T e n n e s s e n, R. M o r r o w and T. T i b b i t s. Light Emitting Diodes as a Plant Lighting Source. *Proceedings of International Lighting in Controlled Environments Workshop*, NASA Conference Publication; Kennedy Space Center, Florida, USA, CP-3309, 1994, 255-268.
9. B u l a R. and R. I g n a t i u s. Providing Controlled Environments for Plant Growth in Space. *International Symposium on Plant Production in Closed Ecosystems*, Narita Japan, August 26-29,1996.
10. Z h o u W., R. B u l a and N. D u f f i e. Performance Evaluation on the Commercial Plant Biotechnology Facility. SAE Technical Paper Series #981666, *28th International Conference on Environmental Systems*, Danvers, Massachusetts, July 13-16, 1998.
11. I v a n o v a T., V. S y c h e v. Project "Greenhouse - Mars" - Plant Growth Study with Different Spectra LEDs Light Units, Proccedings of the Second Scientific Conference with International Participation "Space, Ecology, Nanotechnology, Safety" SENS'2006, 14-16 June, 2006, Varna, Bulgaria.
12. F o l t a K., L. K o s s, R. Mc M o r r o w, H. K i m, D. K e n i t z, R. W h e e l e r and J. S a g e r. Design and Fabrication of Adjustable red-green-blue LED Light Arrays for Plant Research. *BMC Plant Biology* 2005, 5:17.
13. K i m H., G. G o i n s, R. W h e e l e r and J. S a g e r. Green-light Supplementation for Enhanced Lettuce Growth under Red- and Blue-light-emitting Diodes. *HortScience* 39(7):1617-1622, 2004.
14. I v a n o v a T., I. D a n d o l o v, D. D i m i t r o v, B. B o y t c h e v, O. P e t r o v, Y. N a y d e n o v. Light Unit for Space Greenhouse Based on Powerful LEDs, Proceedings of the Third Scientific Conference with International Participation *SENS 2007*, 27-29 June 2007, Varna, Bulgaria, 341-346.
15. D a t a s h e e t f o r C r e e ® X L a m p ® X R L E D, *http://cree.com/products/pdf/XLamp7090XR.pdf*
16. P o l y m e r O p t i c s L i m i t e d, Narrow Angle LED Colour Mixer Assembly, *http://www.polymer-optics.co.uk/Cree%20Colour%20Mixer%20Range.pdf*
17. I v a n o v a T., P. K o s t o v, S. S a p u n o v a, I. I l i e v a, S. N e y c h e v. Plant Cultivation in Space: Next Steps towards the SVET-3 Space Greenhouse Project and Current Advances. Space Technology, Lister Science, Printed in Great Britain (0892-9270/06), Vol. 26, Nos.3-4, 2006, 129-136.

18. I v a n o v a T., I. I l i e v a, Y. N a y d e n o v, V. S y c h e v, M. L e v i n s k i k h. "Greenhouse-Mars" Project: New light-emitting diode module tests. Proceedings of Conference *"Fundamental Space Research"*, 23-28 September 2008, Sunny Beach, Bulgaria, 291-294.

НОВ СВЕТОДИОДЕН МОДУЛ ЗА ОСВЕТЛЕНИЕ РАЗРАБОТЕН ПО ПРОЕКТА "ОРАНЖЕРИЯ-МАРС"

Т. Иванова, И. Дандолов, И. Илиева, Й. Найденов
М. Левинских, В. Сычев

Резюме

Съгласно Договора за научно сътрудничество по Проект „Оранжерия Марс" между Института за космически изследвания, София и Института по медикобиологични проблеми, Москва, български учени разработиха нов осветителен модул на светодиоди (LM-LED). Новият LM-LED е на базата на монохроматични светодиоди (LEDs, тип *Cree® XLamp® 7090 XR*), излъчващи в червената, зелената и синята (RGB) области на спектъра. Блок за управление в DMX стандарт позволява задаване на плътност на фотосинтетичния фотонен поток (PPFD) в границите 0-400 $\mu mol.m^{-2}.s^{-1}$. Бяха проведени лабораторни технически и биологични изпитания на LM-LED с помощта на комплекса апаратура Космическа оранжерия (КО) SVET-2, прототип на летялата на борда на Орбиталната станция МИР. С новия LM-LED бяха проведени два едномесечни експеримента с растенията салата и цикория, със спектрален състав - 70% червена, 20% зелена и 10% синя светлина и PPFD - 400 $\mu mol.m^{-2}.s^{-1}$ (висока осветеност) и 220 $\mu mol.m^{-2}.s^{-1}$ (ниска осветеност). Проследени бяха височините на растенията и анализирани някои биохимични параметри като резултатите бяха сравнени с резултатите от подобни експерименти, извършени със стария Блок за осветление на КО SVET-2 на флуоресцентни лампи (OSRAM DS 11/21). Статията обобщава научно-изследователска работа по проекта "Оранжерия-Марс" за последните 3 години (2006-2008).

Bulgarian Academy of Sciences. Space Research Institute.
Aerospace Research in Bulgaria. 23, 2009, Sofia

ARTIFICIAL SOIL (SUBSTRATE) SELECTION FOR HIGHER PLANT CULTIVATION IN SPACE: GROUND-BASED TESTS FOR ASSESSMENT OF SOME SUBSTRATE PHYSICAL PROPERTIES

Plamen Kostov, Svetlana Sapunova

Space Research Institute - Bulgarian Academy of Sciences
e-mail: plamen_Kostov@space.bas.bg

Abstract

The proposed study presents an approach for early assessment of substrate properties. This includes a course of measurements for preliminary evaluation of part of the substrate's physical and hydro-dynamical characteristics. Two sets of measurements were carried out using standard methods to analyze the substrate's agro-physical properties. In the first set, three different substrate trademarks (Balkanine, Turface and Ekolin) with similar particle sizes (1-2 mm) were tested. The bulk density (BD) of substrate layers of three different thicknesses was measured to study the possibility to achieve repetitive density for the needs of mathematical modelling. In the second set, the physical and hydro-dynamic properties of four particle sizes of Balkanine fractions (PSD) were tested. BD, capillary water capacity, water-holding capacity and saturated water capacity for the four PSDs were determined and discussed. The data show that the 1.5-2 mm fraction is most suitable for earth and space applications because of its low BD (high total porosity) with low StDev values which suggest a repetitive BD when packing the substrate in a real root module and more favourable proportion between air and water content.

Introduction

Continuous improvement of the root-zone media is an important research area motivated by the need to provide suitable root environment for higher plant cultivation in microgravity. Systems for controlling root environment are required to provide steady substrate moistening, non-stop and balanced transfer of nutrients to plant roots and good gas exchange. A

range of conflicting and inadequate requirements has raised problems in the development of root modules for space application. Mass, volume and power constraints have been caused by the requirement to get maximum yield from minimum area (or volume) and power. This imposes hard power and space restrictions on the equipment and reduces the root module volume what leads to higher density of the root area components. The problems of water containment and liquid and gas phase separation in microgravity are of great importance for providing adequate air-water balance in small volume root environment. The separate-phase systems based on porous solids to separate air and water have been adopted for space utilization in most plant growth facilities. Substrates of solid particles are considered to be the most appropriate medium for plant growth in long-term space experiments because of their longevity, repeated use and repeated crops in the same substrate. Particulate substrates that have been used in ground-based and flight tests include peat-vermiculite mixes, arcillite, isolite, Profile and Turface (porous ceramic aggregates with Osmocote pellets used as slow-release fertilizer), Balkanine (natural nutrient saturated zeolite) etc.

Microgravity affects heat transfer, mass exchange processes, fluid behaviour, nutritive concentration gradients in the substrates, and capillary properties of artificial soils. The “free” movement of small substrate particles between the larger ones in the root medium container volume changes the aerating – water-carrying pore ratio and geometry and disturbs the medium homogeneity and density. Furthermore, the substrate particle shrinkage and swelling caused by changes in their water content and the vigorously developing root systems in a small root module volume also leads to variable pore geometry and changes in water retention.

There is still little information available about the nature of problems that might occur in small volumes in microgravity. The current understanding of the nature of water and air transport in porous media in microgravity is not sufficiently well developed to allow clear interpretation of microgravity experimental results. Therefore, upon completing the *Mir* Orbital Station (OS) experiments, scientists from different countries that have experience in various areas of fluid and soil physics, plant physiology, hardware development, and flight experiments met to identify and discuss critical issues of water and air flow through porous media in microgravity [1]. The specific objective of this meeting was to examine the control of air, water, and solutes in a root zone containing solid substrates. Possible mechanisms affecting water and air transport in microgravity that lead to

accentuated hysteresis, reduced hydraulic conductivity, and altered soil-water characteristic curve were discussed. The published studies [2], [3] etc. determine the physical and hydraulic properties of baked ceramic aggregates that have been used as a root medium in ground-based and space experiments. The published information provides to summarize a set of requirements for the substrates – possible candidates for plant growth experiments. The substrate media selected for plant growth research purposes should have definite physical characteristics:

- Substrates for space application should have low specific weight and small packing volume, so as to require minimum launch power.
- Particle size has been a debatable parameter and it should be determined by compromise. The relatively large particle size range (1-5 mm), chosen for aeration reasons for the early *Svet* Space Greenhouse (SG) flight experiment (1990) resulted in water movement problems. On the other hand, the smaller particles (less than 1 mm) impede aeration and such substrate has more pronounced hysteresis of the water retention curve which causes moisture control problems.
- Substrates are required to have uniform particle size distribution, i.e. flatter plateau of the water release curve which means more stringent control of water transport and aeration.
- The parameters mentioned above allow achieving low and repeatable bulk density when filled up in a fixed volume and levelled without compression. The substrate bulk density can be additionally increased using standard compacting methods [2]. Compacting is used to reduce the changes in pore geometry due to overloads during launch, particle rearrangement under microgravity and other factors which lead to changes in substrate–water–air relations.
- Substrates should have long-term spatial and time parameter stability, so as to provide relatively unchangeable particle and pore geometry. This means that no degradation and no swelling of particles in time and space are allowed.

Both particle size and density determine porosity and thus, water retention properties of the material. To achieve high water retention, substrates are required to have good hydraulic characteristics:

- High water holding capacity of the substrate material is needed to achieve high volumetric water content (wettable porosity) for the matric potential control range. For the purpose, the substrate material should have low bulk density and high porosity.

- Substrate material with low hysteresis is preferable for use [1]. Hysteresis occurs in the range of water potential control where small changes in water content produce significant matric potential changes. This range depends strongly on particle size. Dani Or [1] notes that Turface has turned to be harder to control compared to isolite and zeolite because of its high hysteresis.
- Substrate material is required to have high hydraulic conductivity which depends on the pore size. Saturated hydraulic conductivity is greater for the larger particle size fractions. Unsaturated hydraulic conductivity also depends strongly on volumetric water content.

A possible way to overcome the complexity and uncertainty of using particulate media would be to engineer a material specifically designed for space application. Such a material would have fixed pore geometry and optimized pore shape and size in order to achieve better control of the water and air flow through the root medium.

The process of selection of substrate capable to support suitable root environment in small volume containers on earth and in space involves a lot of long, hard and expensive analysis in specialized laboratories. The purpose of this investigation is to suggest a way for preliminary selection of substrates – candidates for space utilization. This includes a course of measurements for early evaluation of part of the substrate's physical and hydro-dynamical characteristics. In case some parameter goes beyond the specified limits, the substrate is not subject to further accurate study in specialized laboratories.

The study proposed is part of a research of the *Svet-3* SG project targeted at development of algorithm for automatic control of plant growth environment to maintain optimal conditions in the chosen substrate during different plant development stages.

Materials and Methods

Substrate materials of three trademarks with the same particle size distribution (1-2 mm) were tested:

1. Balkanine™ (Stoilov, G., I. Petkov, D. Dimitrov, (1979, Bulgarian Patent No 40343), Bulgaria;
2. Turface® (Profile Products LLC, Buffalo Grove, IL, USA);
3. Ekolin® (NIPRORUDA JSCo, Bulgaria).

The first two substrates were used in all space experiments carried out onboard the *Mir* OS in the *Svet* SG in 1990-2000. The third substrate

was proposed by specialists from NIPRORUDA to be subject to test. Below is described the test program used for our research. It could be applied to test all sorts of substrates for evaluation of their physical properties.

A. *Assessment of bulk density (BD) for the three trademark substrates*

Air-dry substrates stored under definite environmental conditions have been commonly used for laboratory plant experiments. The object of the proposed set of measurements is to test the possibilities for early evaluation of the physical properties of air-dry substrates without using compaction techniques. These measurements aim to check if the height and the area of the root modules used for plant experiments influence bulk density when filled up and without additional compacting.

Three vessels of different heights (5.5, 11 and 40 cm) and volumes (1009.5, 1045.6 and 675.1 cm^3, respectively) were filled up with each kind of substrate and levelled using a laboratory spatula. Sample mass (air-dry basis) was measured to calculate bulk density as $BD_{ad} = m_{ad}/V_b$ where BD_{ad} and m_{ad} are the bulk density and mass of air-dry substrate and V_b is the bulk volume. Each test was replicated 50 times. Hygroscopic moistures (θ_h) of 100 g substrate samples after drying for 48 hours at 105ºC were calculated: $\theta_h = m_h/m_s$, where m_h is the mass of the hygroscopic substrate and m_s is the mass of absolutely dry substrate. The bulk densities thus determined (air-dry basis) were re-calculated on oven dried basis using $BD = BD_{ad}/(1+\theta_h)$. The results, processed statistically, provide an idea of the lowest bulk density value for each substrate which is possible to achieve before compacting in the experimental root module volume.

B. *Assessment of bulk density for four particle size distributions of Balkanine*

Balkanine was successfully used in the space plant experiments carried out in the *Svet* SG onboard the *Mir* OS in 1990, 1995 and 1996. For the 1997-2000 *Svet-2* SG experiments, this substrate was substituted by Turface which is wide-used and well studied by our American colleagues.

Analyses of the porous substrate water relations [5] observed in the space experiments show that an optimal wettable – air-filled porosity relation in microgravity can not be achieved by using a wide PSD range (for example 1-3 mm). Small particles fallen into the large particle pore space

could not be tightly compacted irrespective of the compaction techniques used when preparing the root module on Earth. In microgravity, this causes dynamic changes in the contact pressure and contact surface between particles which influences drastically the unsaturated hydraulic conductivity of the substrate. This calls for study of the physical and hydro-dynamic properties of narrower PSDs for experimental substrates.

Balkanine was sieved to retain four particle size fractions – (0.05-0.9); (1.0-1.5); (1.5-2.0); (2.0-3.0) mm using standard sieves. Bulk density of the four PSDs was determined. For the purpose, the following procedure comprising two sets of measurements was used: (a) an aluminum cylinder 6 cm high and 6.5 cm in diameter (volume 200 cm^3) was filled up with air-dry substrate of each fraction without compacting. Substrate material was levelled, sample mass was measured and BD was calculated, and (b) the cylinder was filled in 2-cm layers and each layer was tamped manually using a cylindrical tool with a tabular front surface of about 5 cm^2. After compaction sample mass (m_c) was measured and bulk density (BD_c) was calculated. Each measurement was replicated 10 times. During the measurements the hygroscopic moisture of the tested PSDs was determined by oven drying at 105°C for 48 hours. The absolutely-dry sample masses were determined and the BDs were calculated as described above. The results were statistically processed and the compaction coefficient (K_c) was calculated as: $K_c = BD_c/BD$.

C. *Assessment of capillary water capacity, water holding capacity and saturated water capacity for the four Balkanine PSDs*

Capillary water capacity, water holding capacity and saturated water capacity for PSDs – (0.05-0.9); (1.0-1.5); (1.5-2.0); (2.0-3.0) mm were determined. Cylindrical plastic vessels 6 cm high, 6.5 cm in diameter (volume 200 cm^3) and with an about 90º contact angle of wetting were used for these measurements.

The vessels used to measure saturated water capacity had a valve inlet in the bottom end allowing saturation from below – water table rising to or above the surface. The saturation process took about 3 hours. Air bubbles captured in the substrate volume were not been removed. The saturated sample weight was measured. The absolutely-dry substrate weight and the net water weight were calculated using coefficient (K_w) for re-calculation of the hygroscopic moisture (θ_h) of air-dry substrate: $K_w = 1+\theta_h$.

Saturated water content was calculated as θ_{sat} (m) = m_w/m_s (weight basis) or θ_{sat} (v) = V_w/V_b (volume basis).

The vessels used to measure capillary water capacity and water holding capacity had a number of holes on the bottom allowing free water movement inwards and outwards when capillary suction and water draining after saturation respectively occurs. Capillary water capacity was determined after the sample's weight had reached a constant value (the process lasted several days). After measuring the weight of the sample with capillary retained water the vessel was dipped slowly into another vessel with water and stayed there to full saturation. About two hours later the vessel with the sample was pulled out, it was covered with a plastic lid preventing from evaporation and water was allowed to drain freely. After completing the drainage process the sample weight was measured and the retained water content was calculated.

Capillary water capacity (θ_{CWC}) was calculated as θ_{CWC} (m) = m_{CW}/m_s (weight basis) or θ_{CWC} (v) = V_{CW}/V_b (volume basis) and water holding capacity (θ_{WHC}) as θ_{WHC} (m) = m_{WH}/m_s (weight basis) or θ_{WHC} (v) = V_{WH}/V_b (volume basis) where m_s was the sample mass for oven dry substrate. The measurements were replicated three times.

Results

The results from measurements of sample mass and volume used to calculate BDs for the three tested kinds of substrate were statistically processed and presented in Tables 1, 2 and 3.

Table 1. Mean bulk density (BD), standard deviation (StDev), and coefficient of deviation (CD) for 50 samples of uncompacted 1-2 mm Balkanine and 3 pot heights

Bulk density for uncompacted Balkanine 1-2 mm			
Pot height	h = 5.5 cm	h = 11 cm	h = 40 cm
Number of samples	50	50	50
Mean BD [g/cm^3]	0.7867	0.7767	0.7586
StDev [g/cm^3]	0.0024	0.0025	0.0028
CD [%]	0.30	0.33	0.37

Table 2. Mean bulk density (BD), standard deviation (StDev), and coefficient of deviation (CD) for 50 samples of uncompacted 1-2 mm Turface and 3 pot heights

Bulk density for uncompacted Turface 1-2 mm			
Pot height	h = 5.5 cm	h = 11 cm	h = 40 cm
Number of samples	50	50	50
Mean [g/cm^3]	0.5571	0.5461	0.5433
StDev [g/cm^3]	0.0030	0.0019	0.0029
CD [%]	0.54	0.35	0.54

Table 3. Mean bulk density (BD), standard deviation (StDev), and coefficient of deviation (CD) for 50 samples of uncompacted 1-2 mm Ekolin and 3 pot heights

Bulk density for uncompacted Ekolin 1-2 mm			
Pot height	h = 5.5 cm	h = 11 cm	h = 40 cm
Number of samples	50	50	50
Mean [g/cm^3]	0.4460	0.3858	0.4566
StDev [g/cm^3]	0.0273	0.0244	0.0334
CD [%]	6.11	6.32	7.31

After oven-drying of about 100 g substrate samples the hygroscopic substrate moisture at 40% relative air humidity was fixed at: 2.35% for Turface, 5.60% for Balkanine and 5.37% for Ekolin. BD of the three kinds of substrate was calculated using a coefficient of re-calculation of the air-dry mass into absolutely dry mass which was 1.0235 for Turface, 1.0560 for Balkanine and 1.0537 for Ekolin.

The results show considerable differences in BDs for the three kinds of substrate. Great deviation coefficient is observed for Ekolin. Fig. 1 shows the frequency polygons for the three kinds of substrate and provides to evaluate visually the measurement data's statistical distribution.

Measurement data for Ekolin do not show normal distribution. An additional study discussed below provided to find the reason for this result.

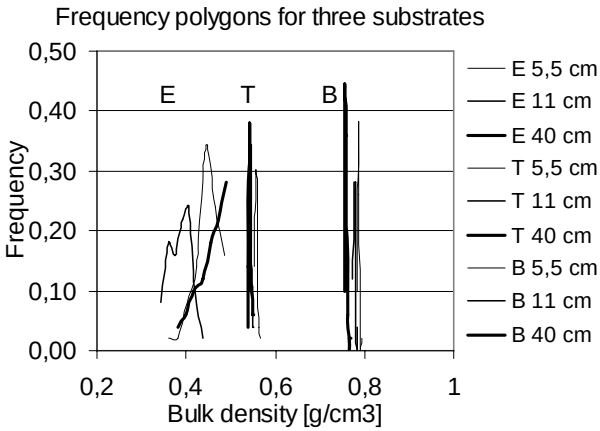

Fig. 1. Comparative illustration of 7-interval frequency polygons for the three tested kinds of substrate – E – Ekolin, T – Turface, and B – Balkanine

Figure 2 allows visual observation of the substrate surface for the three tested kinds of substrate after applying a compaction procedure. A study of BD and hydro-dynamic changes in the substrates after treatment show additionally the processes of particle composition demix for Ekolin (the right pot on the picture).

Fig. 2. A view of Turface, Balkanine, and Ekolin substrate surfaces after compaction procedures – water saturation and 50 Hz vibrations (10 min)

The results from some physical measurements of Ekolin properties show high heterogeneity, quite differing particles and low mixing capability. Such properties do not match the requirements for the substrates used in microgravity experiments. Turface has been well studied and characterized in details by American scientists. For this reason, we chose Balkanine as an experimental substrate and subjected it to our proposed test procedure to evaluate the substrate's physical properties.

As mentioned above, characteristics of narrower PSD should be used for microgravity experiments. For this reason, four PSD fractions for Balkanine were sieved and tested.

After oven-drying of about 100 g substrate samples the hygroscopic substrate moisture at 60% relative air humidity was fixed at 7.1%. A coefficient of re-calculation of the air-dry mass into absolutely dry mass of 1.071 was used.

Bulk density data for compacted and uncompacted substrate samples of each PSD were determined and presented on Table 4.

Table 4. Bulk densities and standard deviations for four tested PSD of uncompacted (BD) and compacted (BD_c) Balkanine

Bulk density data for four Balkanine PSD				
PSD	BD [g/cm^3]	±StDev	BD_c [g/cm^3]	±$StDev_c$
0.05-1.0 mm	0.8517	0.009	0.9791	0.009
1.0-1.5 mm	0.7365	0.005	0.8422	0.005
1.5-2.0 mm	0.7268	0.001	0.8325	0.003
2.0-3.0 mm	0.7374	0.001	0.8576	0.003

Data shows that the compaction coefficients are 1.150, 1.143, 1.145 and 1.163. As may be seen from the comparative chart in Fig. 3, the 1-2 mm fractions have lowest BD and highest total porosity, respectively. The low StDev values for the two cases suggest a repetitive BD when packing the substrate in a real root module.

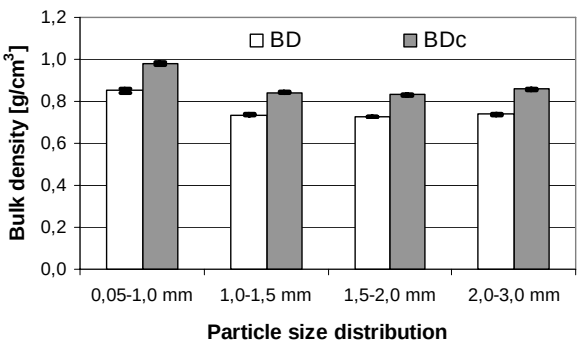

Fig. 3. A comparative chart of the bulk densities and standard deviations for the four tested PSDs of uncompacted (BD) and compacted (BD_c) Balkanine samples

The most important parameters reflecting the relations air-water-substrate are shown on Table 5.

Table 5. Total porosity (calculated) (TP), saturated water content (SWC), water holding capacity (WHC), capillary water capacity (CWC) and maximum hygroscopicity (MH) for the four tested Balkanine PSDs

	Substrate water relations, (volume basis)			
PSD	0.05-1.0 mm	1.0-1.5 mm	1.5-2.0 mm	2.0-3.0 mm
TP	0.59	0.64	0.65	0.64
SWC	0.54	0.57	0.55	0.55
WHC	0.52	0.49	0.40	0.37
CWC	0.49	0.38	0.36	0.34
MH	0.17	0.14	0.14	0.15

Total porosity (TP) was calculated as TP = (1-BD/PD), where PD = 2.37 g/cm^3 is the particle density for Balkanine measured by Zakharov [5]. The maximum hygroscopicity MH = 17% (weight basis) has been measured by Zakharov, too. This parameter is the maximum quantity of water molecules adhered to the particle surface at 99% relative air humidity. This water quantity is not available for plant use.

The chart in Fig. 4 presenting tabled data shows that in normal laboratory experimental conditions, when no measures are taken to expel the air bubbles captured in the substrate volume, the saturated water content is a bit lower than the total porosity for all PSDs.

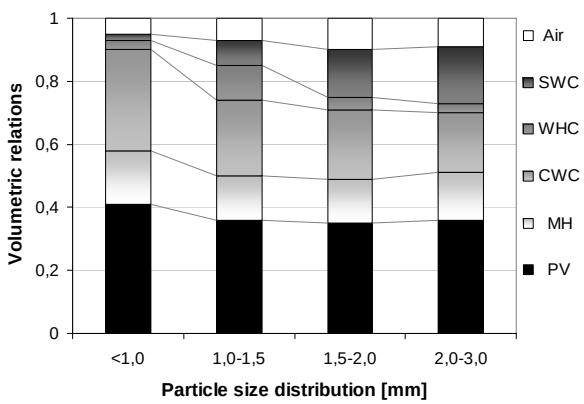

Fig. 4. Volumetric relations of the total porosity (TP), saturated water capacity (SWC), water holding capacity (WHC), capillary water capacity (CWC) and maximum hygroscopicity (MH) for the four Balkanine PSDs

It can be seen that the three water capacity parameters for the smallest substrate fractions are too close which results in small air filled porosity for aeration. For the 1.0-1.5 mm PSD the water holding capacity is close to the saturated water content which leads to higher hysteresis.

Discussions

The greatest part of the time and funds spent to prepare a space plant experiment is allocated to ground-based task development. The choice of suitable substrate, particle size distributions and mixes, aerating and watering regimes and technologies, techniques for repeated seed sowing and plant growth in a root module, development of algorithms to control the actuating mechanisms as well as the accurate assessment of the phenomena observed in the root media during experiments are continuously developed and improved.

The first set of measurements of Balkanine, Turface and Ekolin had as its objective to assess the ability of these loose materials for keeping their minimal BD while filling up the volume of dishes of various shapes. The effect of the measuring dish height, dish sectional area related to the substrate particle diameter and material compaction while levelling on BD was determined. As may be seen from Tables 1-3 and Fig. 1, BD increases in the sequence Ekolin, Turface, Balkanine and Ekolin shows a minimal BD of about 0.4 g/cm^3. The tendency for substrate compacting when filling up a dish 5.5 cm in height and levelling is pronounced for Balkanine and Turface. The substrate column with height of 40 cm and 4.6 cm in diameter involves self-compacting but the relatively small dish diameter limits the particle number in one layer and reduces the levelling effect on BD. So, the difference between BDs in the dishes of 5.5 cm and 40 cm in height for Balkanine is 0.0281 g/см^3, which exceeds StDev 10 times. These results show that it is also necessary to assess the actual BD of substrates when filling up small-dimension dishes (few dm^3) with complicated interior (water and aeration pipes, wick and compaction fabrics and others).

Statistical distribution for Ecolin's BD requires to determine the substrate structure. The manufacturer provides information about the use of "natural clinoptilolite, expanded perlite, vermiculite, water-soluble polymers, saturated with biogenic elements" in the substrate mixture production. The Stoke's law was applied in an experiment to separate the substrate component particles (Fig. 5).

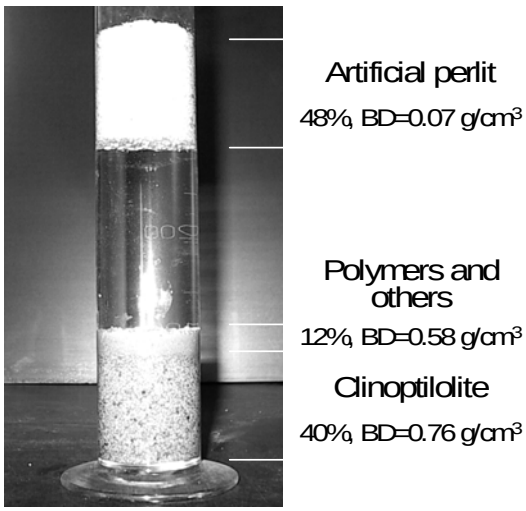

Fig. 5. Ekolin after particle separation

Down below 40% of the volume was occupied by particles with BD = 0.76 g/cm^3 (clinoptilolite), following by 12% particles with BD = 0.58 g/cm^3 above, and 48% was the artificial perlite with BD = 0.07 g/cm^3 keeping afloat. The great disparity between the particle BDs and dimensions allows easier demix when filling up the dish. It was found that the artificial perlite granules did not have the desired hardness and stability (they swell). The results from measurements showed that the requirements for the physical properties of substrates for space application are considerably higher and the further study of Ekolin was abandoned.

Turface has a low BD value (about 0.55 g/cm^3), the total porosity reaches 78% at 2.5 g/cm^3 particle density. The slightly higher CD (0.35-0.54%) compared to Balkanine's CD (0.30-0.37%) can be accounted for the particle shape of both materials. Turface has a slaty particle shape which provides to achieve close contact between particles, respectively greater unsaturated water flow. Fig. 6 shows the three substrates after they have been compacted under saturation with water and 50 Hz vibrations for 10 minutes. After water draining Turface surface becomes smooth, the Balkanine particles keep their outlines and the Ekolin particles demix and a part of them swell.

As mentioned above, Turface has been studied in details by American scientists and used in space plant growing. This is one of the

reasons to continue studying Balkanine which is currently used in our work. Balkanine's accessibility, the available data from ground-based and space experiments, the data about its properties obtained in Russia, USA and Bulgaria, the mathematical modelling and the accumulated experience are additional reasons for testing this material with different laboratory practices and equipment.

Balkanine is natural zeolite charged with chemical elements which provide nutrients for plant growth during several vegetation cycles (over 5). Ivanova [6], [7] provides detailed information about the agrochemical characteristics and use of Balkanine in space experiments. Petrov [7] provides the results from phase analysis performed on a DRON 3M powder X-ray diffraction apparatus using a CoKα radiation source.

The zeolite used for Balkanine production has double porosity - inner-particle and inter-particle. Zakharov [5] and Jones [4, 8] measure the basic hydro-physical characteristics and report that the sharp drop in the matric potential at 22% water content due to full macro-pore water draining leads to drastic decrease of water conductivity (Fig 6).

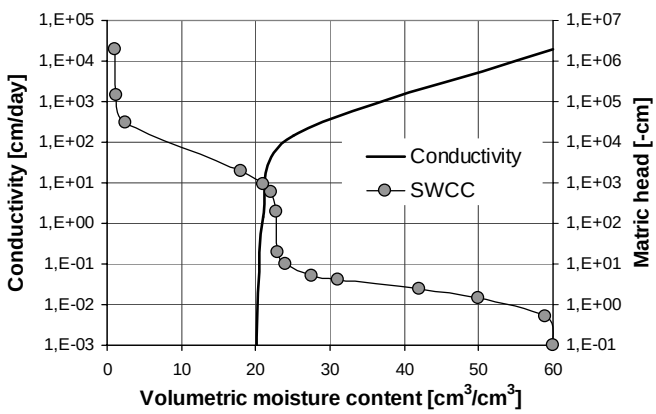

Fig. 6. Matric head and water conductivity of 1-2 mm Balkanine versus volumetric moisture content. (Jones and Or, [13])

Some disadvantages of Balkanine are: (a) appearance of a small fraction (below 0.2 mm) after shocks and vibrations imitating the mechanical effects during equipment launch; (b) comparatively large BD (about 0.84 g/см^3); and (c) inner-aggregate porosity concentrated in the range below 10 μm which reduces unsaturated water conductivity and limits water flow at substrate water content below 0.22 cm^3/cm^3.

The results from BD calculation for the four PSDs (Table 4) show that BD and compaction coefficient (about 14.4%) are lowest for the 1.0-1.5 and 1.5-2.0 mm fractions. Standard deviations for the compacted 1.5-2.0 and 2.0-3.0 mm fractions are higher than the ones for uncompacted fractions, a fact which reflects the substrate material's sensitivity to the compaction procedure method and duration. This is especially important in the cases when substrate is packed in a root module together with additional accessories and soft materials.

The air-water-substrate volumetric relations (Table 5 and Fig. 4) provide information about the total water capacity of the four PSDs, the plant available water part and aeration porosity. Fonteno [9] notes that for soilless substrates that do not contain fine particles, the root module height has a significant effect on the air-water proportions. Our data show that for sample vessel height of 6 cm the water holding capacity is too close to saturation for fractions smaller than 1.0 mm and 1.0-1.5 mm and the capillary water capacity is about 1.5 times higher than the gravitational water for 1.0-1.5 mm fractions and draw level with it for 2.0-3.0 mm fractions. The water contained in the substrate at maximum hygroscopicity (MH, about 14-17% volumetric) is absolutely unavailable for the plant's roots. This conclusion is corroborated by Shaydorov [10] who has determined volumetric water content of 15% at wilting point for salad crops grown in 1-3 mm Balkanine.

The following conclusions could be drawn based on the measurements conducted and discussed above:

- 0.05-0.9 mm PSD has highest BD (about 1 g/cm^3); 7% aeration porosity; 35% Plant Available Water (PAW), 2% difference between saturation and water holding capacity; operation mode close to saturation and blocking of about 5% air bubbles.
- 1.0-1.5 mm PSD has BD = 0.84 g/cm^3; 15% aeration porosity; 35% PAW; 8% difference between saturation and water holding capacity; operation mode with blocking of about 7% air bubbles.
- 1.5-2.0 mm PSD has BD = 0.83 g/cm^3; 25% aeration porosity; 26% PAW; 15% difference between saturation and water holding capacity; operation mode with balance between air and water content; blocking of about 10% air bubbles.
- 2.0-3.0 mm PSD has BD = 0.86 g/cm^3; 27% aeration porosity; 22% PAW; 18% difference between saturation and water holding capacity;

operation mode with predominant aeration volume; blocking of about 9% air bubbles.

Water distribution in substrate pores can be determined using the pore size distribution curve. Drzal [11] presents an analysis of pore size distribution ranges for container substrates. The effective diameter of the biggest water filled pore for every characteristic value of the water head can be calculated using the *Jurin* equation:

(1) $d_p = 4.\sigma/\rho_w.g.h$

where d_p is pore diameter, σ is water surface tension (72.75 J/m^2), ρ_w is water density (1 Mg/m^3), g is gravitational acceleration (9.81 m/s^2), and h is matric head (m).

On the other hand, matric head (h) and volumetric water content (θ) are related by the substrate-water characteristic curve (SWCC). The fitted SWCC of Balkanine (1-2 mm PSD) shown in Fig. 6 is determined by Jones and Or [12] using the van Genuchten [13] nonlinear model, defined as:

(2) $\theta = \theta_s + (\theta_s - \theta_r)/[1 + (\alpha.|h|)^n]^m$

where θ is the current volumetric water content, θ_s is the saturated volumetric water content, θ_r is the residual volumetric water content at 30 kPa (300 cm), α, n, m are fitting parameters, and h is matric head (cm).

Using the determined water capacities (Table 5) and the corresponding matric heads, as well as eqs. (1) and (2), the pore size distribution ranges were determined (Fig. 7). Easily available water for plant roots in 6 cm high dish filled with Balkanine is kept in about 12-15% of the pores and is concentrated in the range of 5-300 cm matric head.

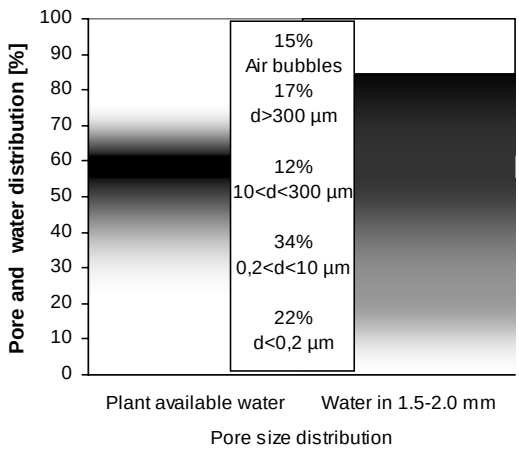

Fig. 7. Plant available water range, pore size distribution, and water distribution in 1.5-2.0 mm fraction

Conclusions

The proposed study presents an approach for preliminary selection of substrates applicable to plant cultivation in microgravity. This includes a course of measurements for early evaluation of part of the substrate's physical and hydro-dynamical characteristics.

Three different trademark substrates (Balkanine, Turface and Ekolin) with similar particle sizes (1-2 mm) were tested. The results of the Ekolin study show high heterogeneity, quite differing particles and low mixing capability. Such properties do not match the requirements for the substrates used in microgravity experiments.

The physical and hydro-dynamic properties of four particle size Balkanine fractions (PSD) were estimated. The data show that the 1.5-2 mm fraction is most suitable for ground-based and space applications because of its lower BD (high total porosity) with low StDev values which suggest repetitive BD when packing the substrate in a real root module and more favourable proportion between air and water content.

Acknowledgements

This research was supported in part by the Bulgarian Ministry of Education and Science under Contract Number KI-1-01/03.

The authors would like to thank technician Diana Antonova for her help and professional work in conducting the laboratory tests.

References

1. Steinberg S. L., D. W. Ming, D. Henninger. Plant Production Systems for Microgravity: Critical Issues in Water, Air, and Solute Transport through Unsaturated Porous Media, 2002, NASA/TM-2002-210774.
2. Steinberg S. L., G. J. Kluitenberg, S. B. Jones, N. E. Daidzic, L. N. Reddi, M. Xiao, M. Tuller, R. M. Newman, D. Or, J. I. D. Alexander. Physical and Hydraulic Properties of Baked Ceramic Aggregates Used for Plant Growth Medium, J. Amer. Soc. Hort. Sci. 130(5), 2005, pp. 767-774.
3. Steinberg S. L. and Darwin Poritz. Measurement of Hydraulic Characteristics of Porous Media Used to Grow Plants in Microgravity, Soil Sci. Soc. Am. J. 69, 2005, pp. 301-310.
4. Bingham G., S. Jones, I. Podolsky, B. Yendler. Porous Substrate Water Relations Observed During the Greenhouse-2 Flight Experiment, SAE Technical Paper Series 961547, 26th International Conference on Environmental Systems, Monterey, CA, July 8-11, 1996.

5. Z a k h a r o v S. B. Some Agro-physical Properties of the Balkanine Substrate for the Svet Greenhouse Regarding the Ground Stage of the Studies, Proc. Second Micro-Symposium “Svet-90”, Varna, Bulgaria, October 5-11, 1990, pp. 56-66.
6. Ivanova, T., I. Stoyanov, G. Stoilov, P. Kostov, S. Sapunova, Zeolite Gardens in Space, Proceedings of the Zeolite Meeting '95, NATURAL ZEOLITES Sofia’95, 18-25 June 1995, (ISBN 954-642-015-8), G. Kirov, L. Filizova & O. Petrov (eds.), PENSOFT, 1997, pp. 3-10.
7. I v a n o v a T. N., P. T. K o s t o v, O. E. P e t r o v, I. I. I l i e v a. Zeolite for Space Greenhouse Experiments on "MIR" Orbital Station, Microporous and Mesoporous Materials, Special issue "ZEOLITE'02", manuscript No. #MMM/MST/02/100TH, 2002.
8. B i n g h a m G., S. J o n e s, D. O r, I. P o d o l s k i, M. L e v i n s k i k h, V. S y t c h o v, T. I v a n o v a, P. K o s t o v, S. S a p u n o v a, D. B u b e n h e i m, G. J a h n s. Microgravity effects on water supply and substrate properties in porous matrix support systems, Acta Astronautica, Vol. 47, No. 11, 2000, pp. 839-848.
9. F o n t e n o W. C. An Approach to Modeling Air and Water Status of Horticultural Substrates, Acta Hort. 238, 1989, pp. 67-74.
10. S h a y d o r o v Yu. I., I. S t o y a n o v, R. O. G e o d a k i a n, V. M. S i m o n o v. “Balkanine” substrate moisture influence on lettuce plants growth, Proc. XVII meeting of Soc. countries on Space Medicine and Biology, Gagra, USSR, May 27 – June 1, 1985, pp. 192-193, (in Russian).
11. D r z a l M., W. F o n t e n o, D. C a s s e l. Pore Fraction Analysis: a New Tool for Substrate Testing, Proc. Int. Sym. Growing Media and Hydroponics, Ed. A. P. Papadopoulos, Acta Hort. 481, ISHS, 1999, pp. 43-54.
12. J o n e s S., D. O r. Microgravity effects on water flow and distribution in unsaturated porous media: Analyses of flight experiments, WATER RESOURCES RESEARCH, Vol. 35, No. 4, 1999, pp. 929–942.
13. V a n G e n u c h t e n M. Th. A closed-form equation for predicting the hydraulic conductivity of unsaturated soils, Soil Sci. Soc. Am. J. 44, 1980, pp. 892-898.

ПОДБОР НА ИЗКУСТВЕНИ ПОЧВИ (СУБСТРАТИ) ЗА ОТГЛЕЖДАНЕ НА РАСТЕНИЯ В КОСМИЧЕСКИ УСЛОВИЯ: НАЗЕМНИ ТЕСТОВЕ ЗА ОПРЕДЕЛЯНЕ НА НЯКОИ ФИЗИЧЕСКИ ХАРАКТЕРИСТИКИ НА СУБСТРАТИТЕ

П. Костов, С. Сапунова

Резюме

Предложеното изследване дава един подход за ранна оценка на качествата на субстрата. Той включва серия измервания за предварително определяне на част от физическите и хидродинамичните

характеристики на субстрата. Бяха направени две серии измервания по стандартни методи за анализиране на агрофизическите качества на субстрата. При първата серия измервания бяха подложени на тест три различни търговски марки субстрати (Балканин, Турфейс и Еколин) със сходен размер на частиците (1-2 mm). Беше измерена обемната плътност на три субстратни слоя с различни височини с цел да се изследва възможността за постигане на повторяема плътност за целите на математическото моделиране. При втората серия измервания бяха тествани физическите и хидродинамичните качества на четири фракции субстрат Балканин. Бяха определени и дискутирани обемната плътност, капилярната влагоемност, пълната полева влагоемност и влагоемността при насищане. Данните показват, че фракцията 1.5-2 mm е най-подходяща за наземни и космически експерименти поради по-малката си обемна плътност (по-голяма порестост) и по-малко стандартно отклонение, което говори за повторяема обемна плътност при насипване на субстрата в реален коренов модул, както и поради по-благоприятно съотношение между съдържанието на вода и въздух в обема на субстрата.

Bulgarian Academy of Sciences. Space Research Institute.
Aerospace Research in Bulgaria. 23, 2009, Sofia

AUTOMATED CONTROL SYSTEM FOR UNMANNED COMBAT AIR VEHICLE

Valentina Tsekova

Rakovski Defence and Staff College, Defence Advanced Research Institute
e-mail: valsof20@hotmail.com

Abstract

A type of automated control system (ACS) for unmanned combat air vehicle (UCAV) is suggested. ACS framework is synthesized out of its block diagram. The diagram and the equations enclosed to them could be used for basic calculations and researches of ACS for unmanned air vehicle.

Introduction

One of the earliest created UCAV is the unmanned plane, controlled by operators. In this case, the operator follows the target and the unmanned air vehicle (UAV) evaluates the deviation between the plane and the target. If there is any diversion, the operator gives command to the plane to eliminate it. In this type of control, the operator takes a very big psychophysical load on himself [1,3,4,5], commensurable with the load of pilots, because of the very limited time and the need to evaluate quickly and precisely the changing situation, when controlling an air vehicle with pronounced inertia. This is why UAV operator selection was similar to pilot selection and their education was long and expensive. The possibility of a hit in the target for this UAV was very low and usually less that 0.5.

Notwithstanding the above-mentioned difficulties in operator-controlled UAVs, they have been used widely, mostly for striking small and mobile targets and objects as tanks, command posts, ground radars, etc., which have less dynamics than UAV.

The abundant available literature on control systems provides no thorough research of the ACS for air vehicles nor states any issues for their synthesis. ACS high noise stability, the possibility to reach high probability for hitting, especially for low contrasted targets, and the comparatively low price for single used board equipment substantiate their wide use, especially in light UAV. That is why their research is interesting not only in the theoretical aspect, but is also of practical value, which is underlined by the possibility for streamlining the control system for reconnaissance UAV, developed and produced in Bulgaria.

Block-Diagram of ACS for UAV

As mentioned above, UCAV operators take a very big psychophysical load upon themselves during the flight to the target. ACS has been developed in order to reduce that load. After the operator identifies the target and turns the UAV in its direction, he just keeps a marker (label, color point, etc.) on it on his monitor screen till the strike. During that time the microprocessor systems are calculating the deviation of the UAV from the target and turn it in such way that its longitudinal axis sticks always through it.

The diagram of ACS for UCAV is shown in Fig. 1.

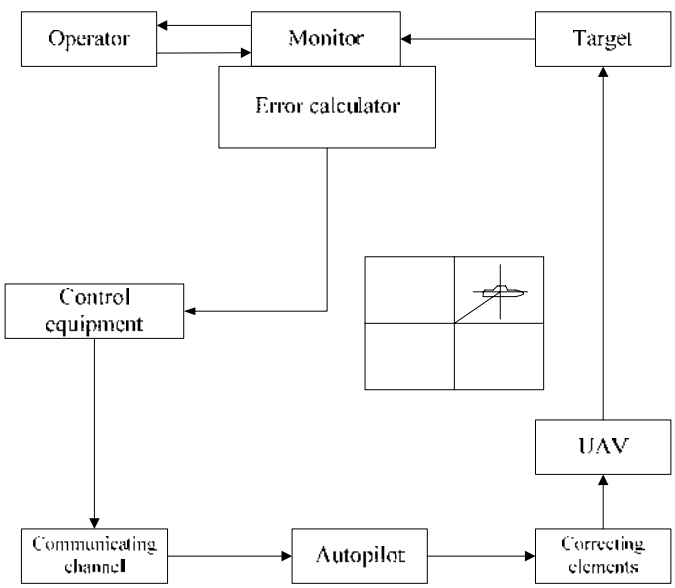

Fig. 1. Block Diagram of ACS for UCAV

It is synthesized on the base of the following control algorithm. After the choice and identification of the target, the operator integrates the longitudinal axis of the board system for air observation (usually television camera or infrared one) with the UAV longitudinal axis. Thus, the target view is centralized on the screen of the monitor and at that very moment the operator marks this position by a marker. When the UAV's longitudinal axis deviates from the target, its view moves out of the centre of the monitor screen. Then the operator indicates again the target by the marker and thus he shows the deviation of the center, i.e. indentifies the deviation of the desired value. Based on this error the error calculator determines the UAV's deviation from the kinematics path and issues the respective signal to the control equipment. It produces correcting signals which reach the UAV auto pilot via the communicating channel. The latter sends the correcting signals which divert the air vehicle correcting elements (the steering wheel) in the direction of the issued command. As a result of the wheel's deviation, the UAV starts to change its flight path until the commands stop, i.e. until the target view is back in the center of the monitor.

The essential difference between the ACS whose operation algorithm was explained above, and the systems controlled manually by operators, from automation point of view, lies in the operator's elimination from the control cycle. Regarding ACS - he has to cover only the target view on the monitor screen and all the decisions are taken by the dedicated and universal computers. This elimination of the operator from the control cycle increases abruptly control quality and the system's efficiency as the psychophysical load on him decreases significantly.

Structural Diagram of ACS for UCAV

The ACV for UAV is a device complex. Together with the operator, these devices measure the target and UAV coordinates and, depending on the adopted law on targeting, the produces commands, which keep the flight to the kinematic pathway. In this process, the plane could be considered as an element of the control system – a generalized correcting element which eliminates the measured error.

The description of the UAV (the airplane) as an element of the automation is presented in the available abundant literature on plane control, e.g. [2], where their longitudinal and cross motion is presented in details. The integration of the function of the UAV on the angle of arrival θ with the angle of alternation of the horizontal wheel δ_x could be expressed by:

(1) $$W_{\theta}^{\delta_x}(p) = \frac{k_{\theta}^{\delta_x}}{T_{\theta} p (T_{\alpha}^2 p^2 + 2\xi_{\alpha} p + 1)},$$

Where

(2) $$k_{\theta}^{\delta_x} = \frac{a_{\omega z1}^{\delta_x}}{a_{\theta}^{\theta} a_{\omega z1}^{\omega z1} - a_{\omega z1}^{\vartheta}}$$

is factor of the angle of arrival to the angle of alternation of the horizontal steering wheel;

(3) $$a_{\omega z1}^{\delta_x} = \frac{1}{J_{z1}} M_{z1}^{\delta_x}$$

where J_{z1} is the plane moment of inertia in relation to the axis O_{z1};

(4) $$M_{z1}^{\delta_x} = m_{z1}^{\delta_x} \frac{\rho V^2}{2} S_k b_a$$

is the plane moment of pitch;

(5) $$m_{z1}^{\delta_x} = f(\alpha, \beta, M, \delta_x)$$

is dimensionless factor; β – angle of resistance; $M = V_в/a$ – Mah's figure; a – local sonic velocity;

(6) $$\overline{\omega_{z1}} = \frac{\omega_{z1} l_k}{2V_в}$$

is dimensionless angular velocity of the UAV around the axis O_{z1}; $\omega_{z1}=d\alpha/dt$ – angular velocity of the plane around the axis O_{z1}; $l_к$ – UAV wing-span; $V_в$ – UAV air velocity; ρ – air density; $S_к$ – wing area; b_a – middle aerodynamic chord;

(7) $$a_{\omega z1}^{\vartheta} = \frac{1}{J_{z1}} M_{z1}^{\alpha}$$

ϑ – angle of pitch; $\alpha = \vartheta + \theta$ – angle of attack;

(8) $$M_{z1}^{\alpha} = m_{z1}^{\alpha} \frac{\rho V_{в}^{2}}{2} S_k b_a;$$

(9) $$a_{\theta}^{\theta} = \frac{1}{m(t) V_{в}} (-P - Y^{\alpha} + G \sin\theta);$$

m(t) – variable airplane mass; P – traction of engine;

(10) $$Y^{\alpha} = C_{y}^{\alpha} \frac{\rho V_{в}^{2}}{2} S_k \alpha$$

is lifting force; G = m(t)g – UAV gravity force;

(11) $$a_{\omega z1}^{\omega z1} = \frac{1}{J_{z1}} M_{z1}^{\omega z1}$$

is UAV angular velocity around the axis O_{z1};

(12) $$M_{z1}^{\omega z1} = m_{z1}^{\omega z1} \frac{\rho V_{в}^{2}}{2} S_k b_a$$

is UAV moment of rotation around the axis O_{z1};
$T_{\theta} = 1/a_{\theta}^{\vartheta}$ – time constant of the plane to the alteration of its path;

(13) $$a_{\theta}^{\vartheta} = \frac{1}{m(t) V_{в}} (P + Y^{\alpha});$$

(14) $$T_{\alpha} = \frac{1}{\sqrt{a_{\theta}^{\theta} a_{\omega z1}^{\omega z1} - a_{\omega z1}^{\vartheta}}}$$

is time constant of the plane to the angle of attack;

(15) $$\xi_{\alpha} = \frac{-a_{\theta}^{\theta} - a_{\omega z1}^{\omega z1}}{2\sqrt{a_{\theta}^{\theta} a_{\omega z1}^{\omega z1} - a_{\omega z1}^{\vartheta}}}$$

is damping ratio of the UAV variation to the angle of attack.

The linear deviation of the plane trajectory strike from the target is as follows:

$$x = V_ц \tau(\lambda_ц + \varepsilon_ц) + r(\varepsilon_ц + \varepsilon_c), \quad (16)$$

where: $V_ц$ – the target velocity; $\lambda_ц$ – the angle between the target velocity vector and the visual axis of TV system; r – radius vector; $\varepsilon_ц$ – the diversion of the target screen image from the monitor center, converted into angle measure; ε_c – the angle between the longitudinal plane axis and the line which connects the UAV with the target; $\tau = \tau_c + \tau_{опер}$, where τ_c is time constant of UAV and $\tau_{опер}$ – time constant of the operator.

Equation (16) shows that the linear deviation of the plane trajectory strike from the target is a sum of two parts, whereas in real tactic conditions the first part is smaller than the second one. Therefore, the ACS functional diagram will be synthesized only by the second part. It is shown in Fig. 2.

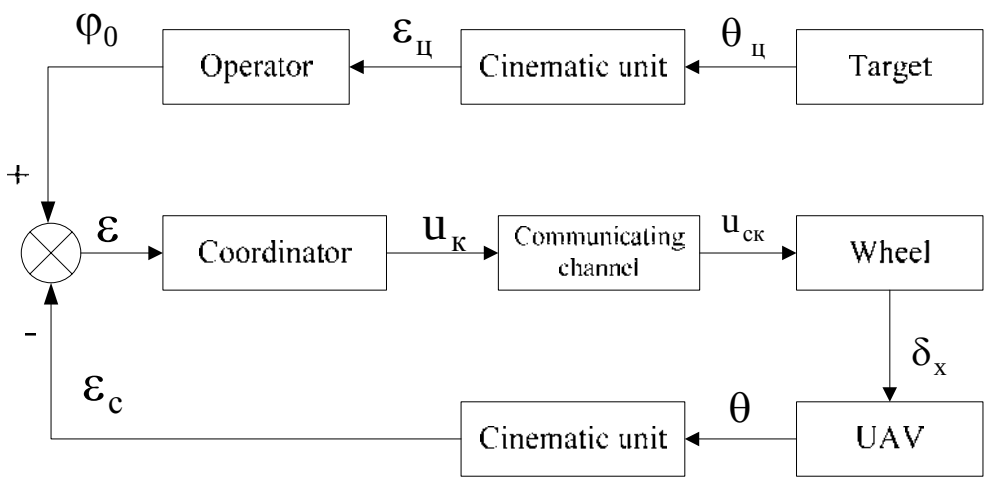

Fig. 2. Functional Diagram of ACS for UCAV

The functional diagram above shows that, as a result of the target trajectory deviation (the angle $\theta_ц$), the operator observes the deviation of the angle of error $\varepsilon_ц$ on the monitor and moves the marker to the converted angle φ_0, so as to cover the target's visualization. The angle φ_0 is incoming (coordinating) signal for the coordinator. The coordinator is formed by the error calculator and the control system shown in Fig. 1. It creates the load

$u_к$, which comes to the steering wheels of the plane (correcting elements) via the communicating channel. They divert into angle δ_x, according to which UAV switches over to a new trajectory, whose angle of arrival is θ. This angle is transformed into angle ε_c by the kinematic unit. The deviation of the angle θ will continue until the equality $\varepsilon = \varphi_0 - \varepsilon_c = 0$ is reached. This equality is an idealization and usually in the stated regime $\varepsilon \to 0$.

The angle ε_c will change, if any deviation of the plane from its kinematic trajectory occurs. After that, the equality $\varepsilon = 0$ will be broken and the coordinator will send a command to the UAV, so that it is restored to the initial trajectory.

The structural diagram of ACS for UCAV could be designed using the functional diagram (Fig. 2), as shown in Fig. 3.

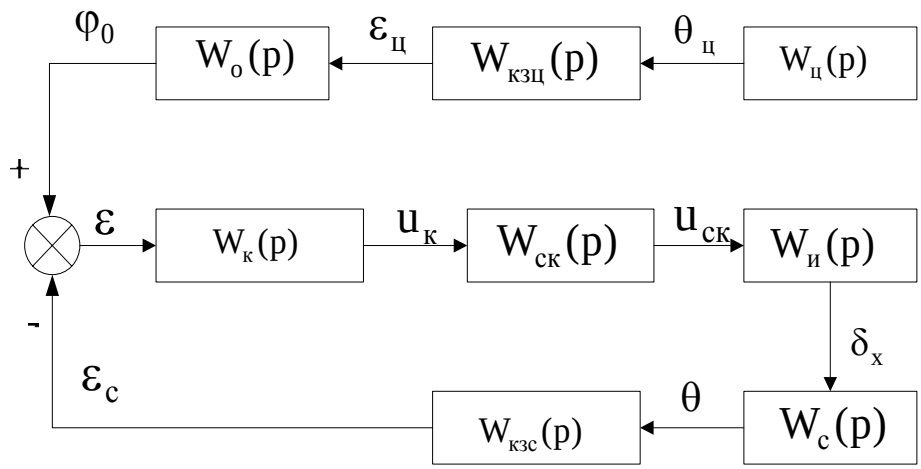

Fig. 3. Structural Diagram of ACS for UCAV

The closed loop control system (without the operator) is of some interest from theoretical point of view. Using the known characteristics of the units, which are part of it, it could be shown in Fig. 4. The following symbols are used: $W_к(p)$ – indefinite transmission function of the coordinator; $K_{ск}$ – factor of the communicating channel; $K_и/p$ – transmission function of the correcting elements (the wheels); $K_\theta^{\delta x}/T_\theta p$ – transmission function of the UAV and $K_{кзс}/p$ – transmission function of the kinematic unit of the unmanned plane.

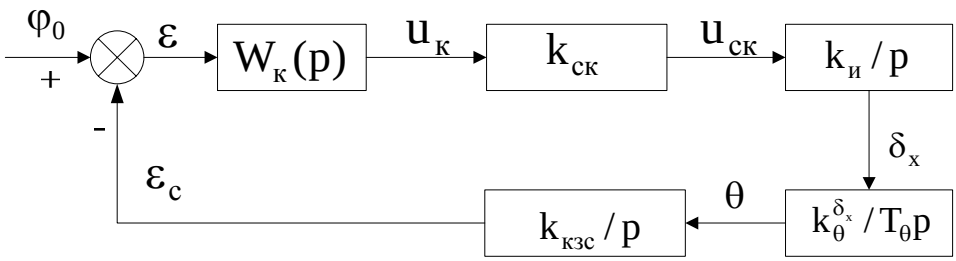

Fig. 4. Structural Diagram of Closed Loop ACS for UCAV

Only the main parameters of the single units of the control system are taken into consideration in the description, as the influence of the small-valued second-order parameters has been ignored. Actually, the influence of the pure delay has been ignored, which could be recognized for the time constants, whose values are 5–10 times smaller than $1/\omega_c$.

Conclusions

The structural diagram, shown in Fig. 4 shows that the closed part of the ACS for UCAV is structurally unstable – there are three integrated units. Therefore, some special measures for its correction have to be taken. The easiest way to make this correction is by using classical automation methods. The transmission function of the coordinator should be considered as transmission function of consecutive correcting elements and should have such parameters and structure, so that the closed system has some previously defined characteristics as:

$$(17) \qquad W_k(p) = \frac{W_ж(p)}{W(p)},$$

where $W_ж(p)$ is the previously desired function of the open loop control system and

$$(18) \qquad W(p) = W_{СК}(p)W_И(p)W_С(p)W_{КЗС}(p).$$

When the automation set is used, for example the method of logarithmic characteristic, the preliminary function of the coordinator $W_к(p)$ could be determined and some requirements could be applied to it – for example to optimize the control system in general.

References

1. Б о д н е р В. А. Оператор и летательный аппарат, М.: Машиностроение, 1976.
2. Г л а г о л е в А. Н., М. Я. Г о л ь д и н о в, С. М. Г р и г о р е н к о. Конструкция самолетов, М.: Машиностроение, 1975.
3. Е л и с е е в А. А., А. А. О в о д е н к о, Управление движущимися объектами, М.: Мир книги, 1994.
4. Инженерная психология в применении к проектированию оборудования, разработано и составлено Обединеным координационным комитетом сухопутных, военно-морских и военно-воздушных сил США, М.: Машиностроение, 1971.
5. Н а з а р о в А. И. Изучение сенсомоторных реакции и двигательных навиков, кн. Инженерная психология М.: МГУ, 1964.

АВТОМАТИЗИРАНА СИСТЕМА ЗА УПРАВЛЕНИЕ НА БОЕН БЕЗПИЛОТЕН ЛЕТАТЕЛЕН АПАРАТ

В. Цекова

Резюме

Предложен е един тип автоматизирана система за управление (АСУ) на боен безпилотен летателен апарат (БЛА). Като е използвана блоковата схема на АСУ е синтезирана структурната й схема. Схемите и уравненията към тях могат да се използват за първоначални разчети и изследвания на АСУ на БЛА.

Bulgarian Academy of Sciences. Space Research Institute.
Aerospace Research in Bulgaria. 23, 2009, Sofia

FAST ALGORITHM FOR DETECTION OF NORMAL AND PATHOLOGICAL EVENTS IN LONG-PERIOD ELECTROCARDIOGRAM RECORDINGS

Stoyan Tanev[1], Plamen Trendafilov[1], Petar Genov[1], Lyudmila Taneva[2]

[1] Space Research Institute – Bulgarian Academy of Sciences
[2] Technical University – Sofia
e-mail: spsbyte@space.bas.bg

Abstract

Fast algorithm based on digital filters is considered. It is intended to detect normal and pathologic events in real ECG recordings. The methods for recognition of normal QRS complexes, pacemakers stimuli and supraventricular extrasystoles are described. The results of the data processing performed by a program based on the described algorithm are shown.

The processing of long-period ECG recordings requires relatively long time periods and depends on the used algorithms. On the other hand, it also depends on the microcontroller or PC computing power. The dedicated program products feature average processing time between 5 and 10 minutes after which, in many cases, manual data processing has to be done. As a result, the overall processing time grows up to one hour.

The aim of this work is to propose and describe a fast algorithm for detection of normal and pathologic events in a real 24-hour ECG recording where the average main processing time of the signal is reduced to 30 seconds. The great number of variations for the patterns of normal and pathological events makes the recognition process very difficult.

To solve the problem and satisfy the requirements arising from the nature of the ECG signal and processing time, digital filtration is chosen. The method of digital filtration is used as a base of the algorithm, where the output signal is given by equation (1):

(1) $$Y[k] = \frac{1}{a_0}\left(\sum_{i=0}^{m} b_i x[k-i] - \sum_{j=1}^{n} a_j [k-j]\right)$$

Where: *x[k]* - input data and a_j, b_i - constant coefficients.

To reveal the specific parts in the ECG recording, it is expedient to use a digital filter with second order Butterworth type infinite pulse characteristic, whose structure is shown in Fig.1.

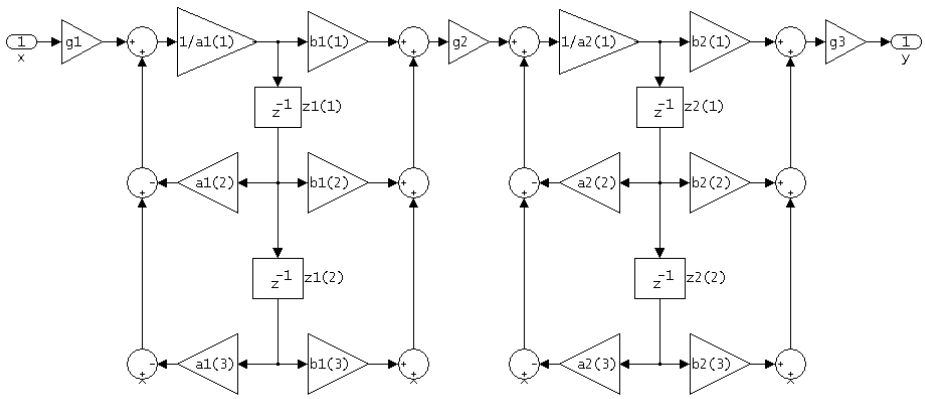

Fig. 1. Structure of the used Butterworth type digital filter

Where: *X* – filter input;
Y – filter output;
g1, g2, g3 – gain coefficients;
a(1,2,3) b(1,2,3) – filter coefficients;
$z^{-1}(1,2,3)$ – the last value of Z;

The signal processed with this filter provides to obtain the required filter slope and high event-detection speed typical for the ECG signal. The algorithm of the signal processing is shown in Fig. 2.

The algorithm works with two data arrays, Buff1[n] and Buff2[n], registered by the first and second channel of the ECG holter. The length of the record is 24 hours. The Event[n] array is intended to save the type and place of the discovered event. *Nk* is a constant representing the number of discrete determined by formula (2).

(2) $$N_k = \frac{120 * F_d}{1000}$$

Where: *Nk* discrete number, 120 constant (set equal to 120 ms and used as time threshold in detecting ventricular extrasystoles)

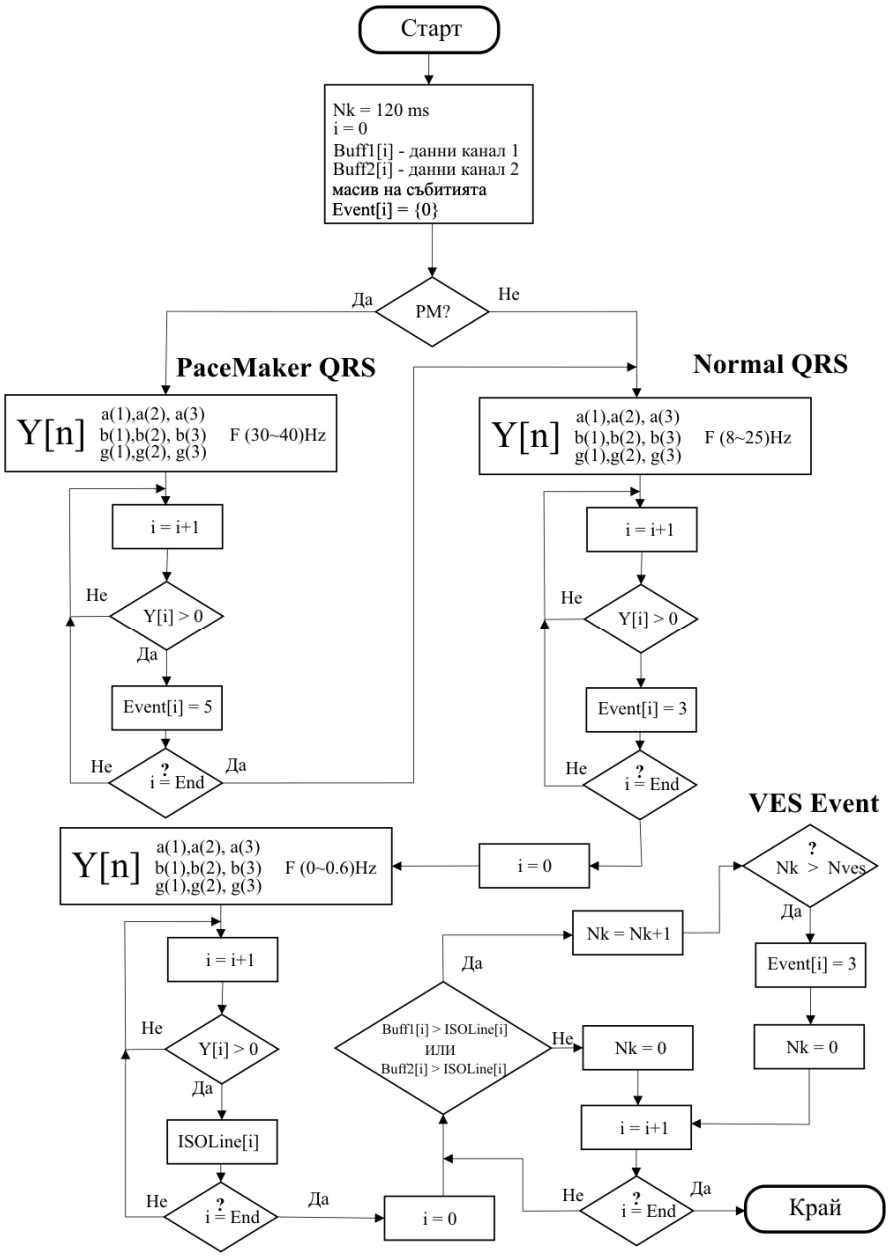

Fig. 2. Signal processing algorithm

In practice, quite often, ECG data recorded by different types of pacemakers, such as unipolar, bipolar, “on demand” and more has to be processed. This makes data processing more difficult. A common feature of all these devices is the generation of a short pulse (width of 1-7 ms) with each heart contraction.

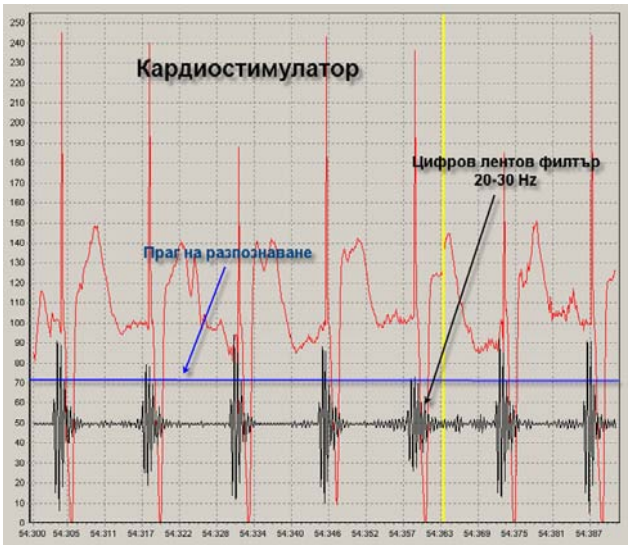

Fig. 3. Determination of the stimulating pulse place in the RR interval

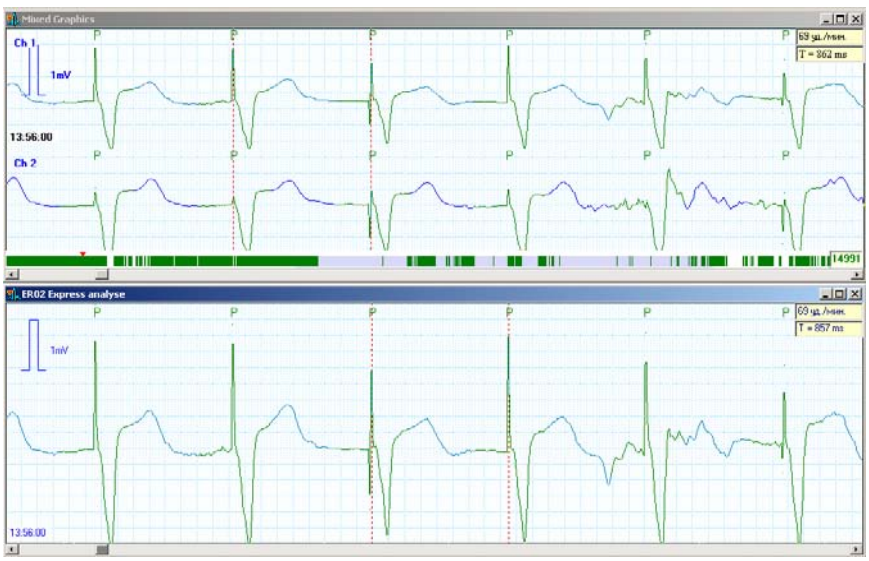

Fig. 4. Results after the signal processing

To find the place of the stimulation pulse in the RR interval, the signal has to be passed through a band digital filter with band frequencies of 20-30 Hz. If the signal is greater than the preliminary set threshold (not shown in Fig. 2 to simplify the algorithm's diagram), we consider that a stimulation pulse is generated at this place. Then, all signals greater than the threshold are ignored for a time period equal to 200 ms corresponding to heart rate of 300 beats per minute, upon detecting the event (Fig. 3). The results of the signal processing are shown in Fig. 4.

If there is no indication of the presence of cardiostimulator, the algorithm starts processing the signal using the band pass filter within the range of 12-20 Hz. The difference between the levels in the same part of the recording, processed by a detecting filter for stimulator generated pulses and the normal QRS complex is shown in Fig. 5 (20-30 Hz) and Fig. 6 (12-20 Hz).

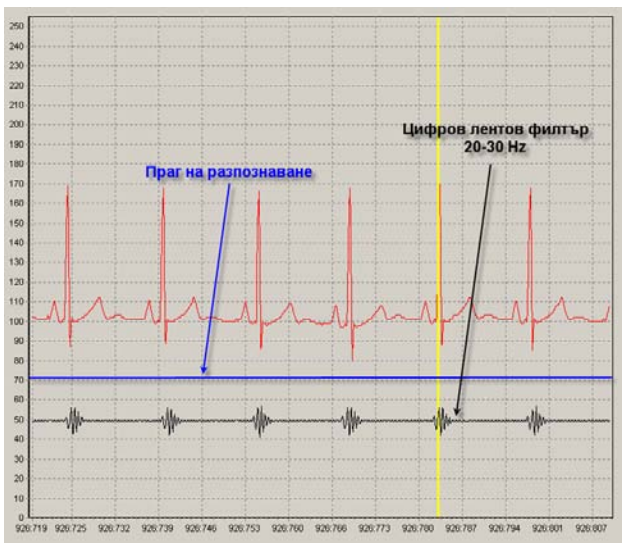

Fig. 5. Detecting pulses generated by a cardiostimulator

During the analysis and detection of the normal QRS complexes, time-frequency valuation could be applied, using the proposed algorithm for VES detection. Ventricular extrasystoles (VES) are wider than normal QRS complexes. Normal QRS complexes change within the range of 50–110 ms for healthy people and depend on sex and age. For VES detection, the signal must be processed using a low pass digital filter with frequency of 0–0.7 Hz.

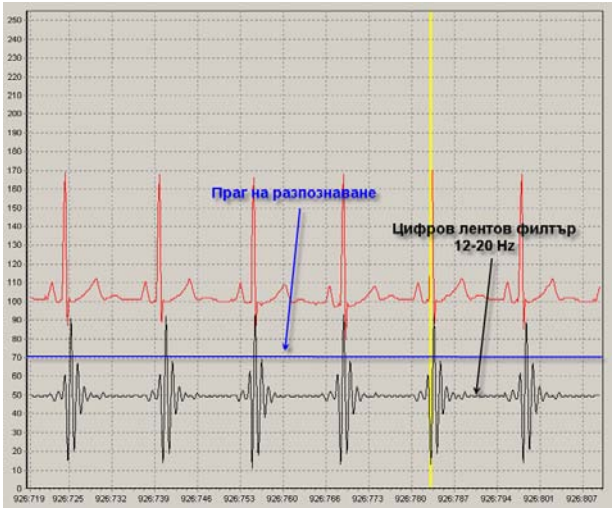

Fig. 6. Detecting pulses from normal QRS complex

The output of the filter follows the isoline of the signal recorded by the registration device and is used as start voltage threshold – first crossing point of the event on the graphic and the filter output signal, or end voltage threshold – second crossing point of the event on the graphic and the filter output signal. If the measured time is greater than 120 ms, the algorithm determines that a VES event is discovered. The measurement is presented in Fig. 7.

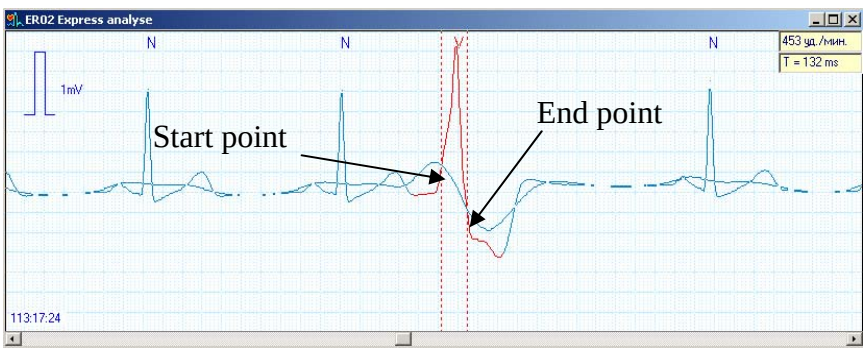

Fig. 7. VES detection algorithm

The signal processing is carried out simultaneously on both channels. It is enough to satisfy the requirement for the time threshold in one of the two channels to determine that the event is VES. The presence of

artifacts with width close to VES's width will be recognized as a VES. The correction can be made by secondary data analysis and the application of various correlation analyses.

Conclusion

The method described above reduces greatly the time period of long time period ECG recordings. The method increases the reliability of the data processing results. The fast algorithm provides to make one or more processing passes of the signal for secondary analysis. Analyses for different recording lengths are possible. The method is useful in cases where human status needs to be determined quickly under extreme conditions, such as during space missions.

References

1. P a n J. and T o m p k i n s W. J. (1985): 'A real-time QRS detection algorithm', *Eng.*, 33, pp. 1157–1165.
2. M e r v i n J. G. and G o l d s c h a l a g e r N. (1989): 'Principles of clinical Electrocardiography', *Appleton Lange*.
3. F r i e s e n G. M., C. J. T h o m a s, M. A. J a d a l l a h, S. L. Y a t e s, S. R. Q u i n t, and H. T. N a g l e (1990): 'A comparison of noise sensitivity of 9 QRS detection algorithms', *IEEE Trans. Biomed. Eng.*, 37(1), pp. 85–98.
4. L i n P. K. and C h a n g W. H. (1997): 'A technique for automated arrhythmia detection of holter ECG', *In Proceedings of Engineering in Medicine and Biology*, 35, pp. 626–631.

БЪРЗ АЛГОРИТЪМ ЗА ОТКРИВАНЕ НА НОРМАЛНИ И ПАТОЛОГИЧНИ СЪБИТИЯ В ЕЛЕКТРОКАРДИОГРАФСКИ ЗАПИСИ С ГОЛЯМА ПРОДЪЛЖИТЕЛНОСТ

Ст. Танев, Пл. Трендафилов, П. Генов, Л. Танева

Резюме

Разгледан е бърз алгоритъм за откриване на нормални и патологични събития в реален ЕКГ запис. Алгоритъмът е базиран на обработка на сигнала с цифров филтър от втори ред тип Butterworth.

Описани са етапите при обработката на сигнала за разпознаване на нормални QRS комплекси, стимулиращи импулси от кардиостимулатор и камерни екстрасистоли. Постигната е висока скорост на бързодействие и висока степен на достоверност на резултатите при използване на минимални изчислителни ресурси. Показани са резултатите от анализа на сигнала с програма, работеща по описания алгоритъм.

A NEW BOOK DEDICATED TO NATURAL DISASTERS AND SPACE METHODS AS A POWERFUL TOOL TO COMBAT THEM*

Millions of victims, much more left injured and homeless, great material losses and heavy destructions – these are just some of the negative effects of the various natural disasters worldwide. Even today, in the beginning of the 21st century, they are taking their heavy toll of human lives and material damages. It is agreed unanimously that such toll and damages strongly depend on the quality of the buildings' construction and the population's preparedness. The effectiveness of emergency planning measures and their enforcement, the quick and well organized response to natural disasters are among the most important factors for successful mitigation of the various natural hazards. This has always been a crucial topic and now, shortly after the end of the UN's Triennium of the Earth, 2007-2009, the entire world is allocating a lot of resources, developing educational programs and taking active measures to mitigate the calamitous effects of earthquakes, tsunamis, global climate change and all other catastrophic events occurring on the Earth's surface. Five years after the devastating tsunami in the Indian Ocean (The Boxing day event, which took more than 300,000 victims and left more than 1,000,000 people homeless), and while still shocked by the recent calamitous earthquake in Haiti (with estimated human toll of over 70,000 people, not to mention material damages) people are still unable to put up with such big tragedies. Why the scientific community has been silent about these event, which hit so unexpectedly. And when will thy strike again?...

It has become clearer than ever now that humanity is going to experience an increasing number of disasters in the future due to the dynamic Earth. Global climate change, the development of the ozone hole, the El Nino phenomenon and the fast geodynamic events registered by the GPS in the solid earth, as well as the increased urbanization are the main factors which will augment Nature's negative effects on people's everyday life.

Therefore, the newly published book "Natural Hazards and Ecological Catastrophes – Study, Prevention, Protection" is very useful and actual. The author, Prof. Garo Mardirossian from the Space Research Institute of the Bulgarian Academy of Sciences, does not need some special presentation. Well known for his popular scientific books, he is working hard on the problems of natural hazards and their study by aerospace methods and techniques. This is his 5th book on the topic, all of them accepted gratefully by the audience.

In the beginning of his last book the author provides some general data about natural hazards, their generation and development and the many physical properties underlying their potential to cause negative effects. Many terms like risk, vulnerability, multi risk and preliminary assessment of consequences are highlighted. Significant attention is paid to ecological catastrophes, war consequences and geophysical weapons. Step by step, the study goes deeper to unveil the nature and effects of such calamitous events as earthquakes, landslides, cyclones, volcanic eruptions, tsunamis, avalanches, floods, wild fires, thunderstorms, tornadoes, etc. Each disaster type is dedicated a separate chapter. The author provides a lot of data for their occurrence, statistics of the victims and the damages, and describes the most extreme cases. Special attention is paid to natural hazards on Bulgarian territory. The main parameters generating the negative effects for the population and the infrastructure are discussed. Special attention is paid to the prevention and protection of the individuals and society. The presentation of the potentials of aerospace technologies for such studies and observations and their high effectiveness is very useful. While supporting the idea that these methodologies could be a very effective tool to combat natural disasters, the book provides a lot of improvements that have been made during the new millennium.

The text is well narrated and illustrated with many schemes, figures and photos. It could be useful to many different specialists – scientists and researchers in the field of geophysics and ecology, geography and meteorology, decision-makers and civil defence servants, engineers and land planners, as well as students from schools and universities. The book contains 372 pages, 56 figures, and 20 tables. It is supplied with annexes containing the measurement scales for the various natural hazards.

The actual content and usefulness of the book alongside with the fact that books on this topic are rarely published both in Bulgaria and abroad make the book of Prof. Mardirossian a major event in our scientific community.

Assoc. Prof. Dr. Boyko Ranguelov

**Мардиросян, Г. „Природни бедствия и екокатастрофи – изучаване, превенция, защита". Академично издателство „Проф. Марин Дринов", София, 2009, 372 стр.*

In memoriam

Prof. DSc Dipl. Eng. Nikola Georgiev

On 10.08.2009 the outstanding Bulgarian scientist Prof. Nikola Georgiev, DSc, passed away at the age of 75.

Prof. Georgiev was a widely recognized geodesy expert. He graduated from the Higher Institute of Architecture and Construction. He started his scientific and pedagogical career at the Higher People's Military Artillery School, Town of Shoumen, where he lectured in Mathematical Geodesy and Cartography, Geodetic Astronomy, and Physical Geodesy. During this period he became post-graduate student of the prominent Bulgarian scientist-geodesist, Acad. Vl. Hristov, and in 1967 presented successfully his PhD Thesis on the topic *The Direct and Reverse Geodetic Problem for Great Distances* which was published as a monograph in 1967.

In 1965, Prof. N. Georgiev joined the Central Laboratory for Higher Geodesy (CLHG) at the Bulgarian Academy of Sciences (BAS) as a Research Fellow. Here, he focused his scientific activity and interests in the field of Space Geodesy, a new and prospective scientific field at that time. In recognition for his successful results, during 1975-1977, he was invited to work for the Council of Astronomy of the Russian Academy of Sciences, where he developed analytical theory for high-precision determination of Earth satellite orbits and their use for the purposes of space geodesy. In 1978, he presented his Doctorial Thesis at the *A. Sterberg* State Institute of Astronomy of the M. *Lomonossov* State University of Moscow on the topic *A Satellite Geodesy Orbital Method for Short Time Intervals* to acquire the title Doctor of Physico-Mathematical Sciences. The major results of this thesis were published in the joint Bulgarian-Russian monograph *Using Earth Satellite Optic Observations for Geodetic Purposes* which was published in 1979 and later on gained great popularity.

Upon his return to Bulgaria in 1977, N. Georgiev was appointed Director of the CLHG–BAS. Here, he organized a large team of researchers and professionals, which developed successfully various aspects of the analytical theory for determination of satellite orbits, with particular emphasis on its application for the purposes of global geodynamics. Under his supervision, the CLHG continued its

scientific research work in both the traditional fields of higher geodesy, as well as in some new areas. In his capacity of Director of the CLHG, Prof. N. Georgiev paid particular attention to the young researchers assisting their scientific and creative development.

From 1990 to 2007, Prof. Georgiev worked for the SRI–BAS where he focused his efforts on the methods for georeference, rectification, and interpretation of high-resolution space images; space methods for study of regional and global geodynamics; analysis of remote-sensing and ground-based studies of the neotectonics and geodynamics of the Moesian platform. During this period, he was also Chairman of the General Assembly of Scientists.

The career of Prof. N.Georgiev was marked not only by his prolific scientific activity, but also by his pedagogical practice. He lectured at the Higher Institute of Architecture and Construction, the *Gen. Blagoy Ivanov* Higher People's Military Construction School, the Higher People's Military Artillery School, the University of Shoumen and more.

The results of the long-lasting and scientific and organizational activity of Prof. N. Georgiev resulted in his wide international recognition. He was member of international and overseas organizations, his name is inscribed on a number of home and foreign encyclopedias, he was elected member of a number of foreign Academies of Science on account of his academic achievements, he was also leader of international projects and programs. Some of the prestigious positions held by Prof. Georfgiev are: National Coordinator and active participant in influential overseas organizations, such as: INTERCOSMOS, KAPG, COSPAR, MAG, МСГГ; Scientific Secretary of the Dedicated Scientific Council in Geodesy and Geophysics; member of the Scientific Council in Geophysics at the Higher Attesting Committee; Vice-Chairman of the Dedicated Scientific Council in Geodesy at the Higher Attesting Committee. His versatile and rewarding activity was honoured by the awarded Order of Cyril and Methodius, I class, Golden Order of Labour, Badge of Excellent Worker of the BAS etc.